



저작자표시-비영리-변경금지 2.0 대한민국

이용자는 아래의 조건을 따르는 경우에 한하여 자유롭게

- 이 저작물을 복제, 배포, 전송, 전시, 공연 및 방송할 수 있습니다.

다음과 같은 조건을 따라야 합니다:



저작자표시. 귀하는 원저작자를 표시하여야 합니다.



비영리. 귀하는 이 저작물을 영리 목적으로 이용할 수 없습니다.



변경금지. 귀하는 이 저작물을 개작, 변형 또는 가공할 수 없습니다.

- 귀하는, 이 저작물의 재이용이나 배포의 경우, 이 저작물에 적용된 이용허락조건을 명확하게 나타내어야 합니다.
- 저작권자로부터 별도의 허가를 받으면 이러한 조건들은 적용되지 않습니다.

저작권법에 따른 이용자의 권리는 위의 내용에 의하여 영향을 받지 않습니다.

이것은 [이용허락규약\(Legal Code\)](#)을 이해하기 쉽게 요약한 것입니다.

[Disclaimer](#)

공학박사 학위논문

**Low-temperature methane combustion
over Co and Pd-based catalysts**

코발트와 팔라듐 기반 촉매 상에서의
저온 메탄 연소 반응

2023년 2월

서울대학교 대학원

화학생물공학부

유 상 범

Low-temperature methane combustion over Co and Pd-based catalysts

지도 교수 김 도 희

이 논문을 공학박사 학위논문으로 제출함
2023년 1월

서울대학교 대학원
화학생명공학부
유 상 범

유상범의 공학박사 학위논문을 인준함
2023년 1월

위 원 장 _____ 이 원 보 _____ (인)

부위원장 _____ 김 도 희 _____ (인)

위 원 _____ 강 중 현 _____ (인)

위 원 _____ 김 지 만 _____ (인)

위 원 _____ 박 영 권 _____ (인)

Abstract

Low-temperature methane combustion over Co and Pd-based catalysts

Sangbeom Yoo

School of Chemical and Biological Engineering

The Graduate School

Seoul National University

Natural gas is one of the most abundant energy sources on earth and can be used for electric power generation, heating, and transportation. Methane, a major component of natural gas, produces less pollution during combustion than conventional petroleum-based fuels. Thus, a large number of gasoline and diesel engines are being replaced by natural gas engines to reduce the emission of nitrogen oxides, sulfur oxides, and hydrocarbons. However, unburned methane is emitted from natural gas vehicles. Because the global warming potential of methane is 25 times greater than that of CO₂, methane emission regulation is being implemented for environmental protection. The catalytic combustion of methane ($\text{CH}_4 + 2\text{O}_2 \rightarrow \text{CO}_2 + 2\text{H}_2\text{O}$) is one of the most effective methods for reducing methane emissions from natural gas engines. However, methane is very stable because of its strong C–H bonds; methane oxidation requires high temperatures and consumes a large amount of energy. Therefore, catalysts for low-temperature

methane oxidation are urgently required to reduce the energy consumption of this process.

Currently, Pd-based noble metal catalysts are the most widely used and most active catalysts for the methane combustion reaction. However, the volatile price of noble metals limits their industrial applications. Fortunately, transition metal oxide catalysts, such as perovskite oxides or spinel oxides, are attractive alternatives. Among these transition metal oxides, spinel-type cobalt oxide is widely used as an active catalyst for methane combustion reactions. However, the poor intrinsic activity of metal oxides relative to Pd catalysts limits their application in low-temperature methane oxidation reactions.

In chapter 2, the poor activity of bulk cobalt oxide catalyst was enhanced by two different methods. First, the textural property of the bulk catalyst was enhanced by the introduction of mesoporosity. Second, the synthesized mesoporous cobalt oxide catalysts were treated with nitric acid to further modify the surface structure and chemistry. The prepared catalysts were applied to the methane combustion reaction and a significant enhancement in catalytic activity was observed for the acid-treated catalysts compared to the pristine catalyst. The properties of the acid-treated catalyst were investigated in detail using various characterization techniques. In particular, transmission and scanning electron microscopy images revealed a roughening in the surface morphology of the acid-treated catalysts. Meanwhile, the H₂ temperature-programmed reduction results showed that the reducibility of the cobalt oxides was enhanced by the acid treatment. In addition, O₂ temperature-programmed desorption and X-ray photoelectron spectroscopy analyses revealed that the acid-treated catalysts contained larger amounts of surface chemisorbed oxygen than the pristine catalyst, which may explain the enhanced reducibility and oxidation activity of the acid-treated catalysts. In conclusion, simple acid treatment is a useful post-treatment method for the synthesis of highly active bulk oxide catalysts for the methane

combustion reaction.

Although it was possible to significantly increase the methane oxidation activity of the cobalt oxide catalyst by the acid treatment, the catalytic activity was still inferior than the noble metal catalysts. Noble metal catalysts, especially those containing Pd, have attracted significant attention due to the excellent catalytic activities for various oxidation reactions. Because of their high cost, noble metal catalysts are generally prepared by dispersing a small amount of the precious metal on a support material, such as alumina, ceria, or zeolite. However, Pd catalysts are vulnerable to H₂O in the exhaust gas, which is known to severely inhibit the initial activity and cause deactivation during the long-term operation. One of the possible solutions for synthesizing the catalyst that is resistant to H₂O is using hydrophobic support. Among the various support materials, zeolite can be effective support for the methane oxidation catalyst because the hydrophobicity can be enhanced by increasing Si/Al₂ ratio. Zeolite can be easily dealuminated by steam treatment at high temperature, which is often called as hydrothermal treatment.

In chapter 3, the effects of dealumination on Pd/SSZ-13 catalysts for methane combustion were investigated. Pd(1)/SSZ-13 (HTA), which was prepared by treating the catalyst hydrothermally at 750 °C, displayed extremely low catalytic activity. On the contrary, Pd(1)/SSZ-13 (DeAl) catalyst, which was prepared by treating the SSZ-13 support hydrothermally and subsequent Pd impregnation, exhibited superior catalytic activity for methane oxidation. Catalytic properties, including zeolite hydrophobicity, Pd location and states were investigated by using various characterization techniques to clarify the differences between the catalysts. Most Pd species in the Pd/SSZ-13 (HTA) catalyst existed as Pd ions, which were not very active for the reaction. On the contrary, most Pd species in the Pd(1)/SSZ-13 (DeAl) catalyst existed as PdO nanoparticles at the external surface, which were highly active for the methane oxidation. In summary, the amount of external PdO nanoparticles should be maximized in order to synthesize highly active Pd/SSZ-13

catalyst for the methane combustion, which was achieved by dealuminating the SSZ-13 support before the Pd impregnation.

Because it was revealed that the hydrophobicity of the zeolite support was not critical factor for the catalytic activity, we decided to use other support material. Ceria is generally utilized for oxidation reactions owing to the redox properties arising from the $\text{Ce}^{4+}/\text{Ce}^{3+}$ cycle, strong interaction with supported metals and large oxygen storage capacity. Because of the limited availability of noble metals, the synthesis of highly active catalysts with low metal loadings is essential for industrial applications. Pd species in Pd/CeO₂ catalysts can exist in various states, most commonly as metallic Pd, PdO nanoparticles, and highly dispersed Pd ions stabilized in ceria defect sites by forming a Pd_xCe_{1-x}O_{2-δ} solid solution. Each Pd phases exhibits different catalytic activities for different reactions. Therefore, understanding the active phase of Pd for a specific reaction is important to synthesize a highly active catalyst with an appropriate Pd state.

In chapter 4, the effects of Pd precursor on the state of Pd species in the Pd/CeO₂ catalysts were investigated. The Pd/CeO₂ catalysts were prepared using different Pd precursors and applied to CH₄ and CO oxidation. Significantly, the Pd/CeO₂ catalyst prepared using palladium nitrate (Pd(2)/CeO₂ (N)) was highly active toward CH₄ oxidation, whereas the catalyst prepared using palladium acetate (Pd(2)/CeO₂ (A)) exhibited high CO oxidation activity. The effects of the precursor on the catalytic activity and other properties were studied using various characterization techniques. The Pd(2)/CeO₂ (N) catalyst contained surface PdO nanoparticles, which were active sites for CH₄ oxidation. On the contrary, the Pd(2)/CeO₂ (A) catalyst possessed Pd ions stabilized at CeO₂ defect sites, which were not very reactive. However, the high Pd dispersion was beneficial for the CO oxidation reaction. Therefore, the Pd precursor clearly altered the Pd dispersion and state in the Pd/CeO₂, which are critical for catalytic activity.

Keywords: Low-temperature methane combustion, Co_3O_4 catalyst, acid treatment, supported Pd catalyst, dealumination, Pd precursor

Student Number: 2017-26064

Contents

Chapter 1. Introduction	1
1.1. Catalysts for low-temperature methane combustion	1
1.2. Objectives	2
 Chapter 2. Methane combustion over mesoporous cobalt oxide catalysts: Effects of acid treatment	 5
2.1. Introduction.....	5
2.2. Experimental	7
2.3. Results	10
2.4. Discussion.....	39
 Chapter 3. Effects of dealumination on the methane combustion activity of Pd/SSZ-13 catalysts	 42
3.1. Introduction.....	42
3.2. Experimental	43
3.3. Results	46
3.4. Discussion.....	71
 Chapter 4. Effects of Pd precursors on the catalytic properties of Pd/CeO₂ catalysts for CH₄ and CO oxidation.....	 80
4.1. Introduction.....	80
4.2. Experimental	82
4.3. Results	84
4.4. Discussion.....	105
 Chapter 5. Conclusions	114

Bibliography	117
초 례	134

List of Tables

Table 2-1. Catalytic activities (T_{50}) of the Co_3O_4 catalysts	13
Table 2-2. Catalytic activities of the cobalt based catalysts reported in the literatures.....	17
Table 2-3. Textural properties of the m- Co_3O_4 catalysts.....	23
Table 2-4. Textural property of the b- Co_3O_4 catalyst.....	25
Table 2-5. Hydrogen consumption during the H_2 -TPR experiments.....	31
Table 2-6. Oxygen desorption during the O_2 -TPD experiments	34
Table 2-7. Cobalt and oxygen species on the surface of the m- Co_3O_4 catalysts obtained from XPS analysis.....	38
Table 3-1. T_{50} values of the Pd/SSZ-13 catalysts	49
Table 3-2. Textural properties of the Pd/SSZ-13 catalysts.....	54
Table 3-3. PdO/Pd _{total} ratio of the Pd/SSZ-13 catalysts	65
Table 3-4. Surface and bulk Pd concentration of the Pd/SSZ-13 catalysts.....	70
Table 3-5. T_{50} values of the Pd/SSZ-13 catalysts; dry and wet condition	73
Table 4-1. T_{50} values of the Pd(2)/ CeO_2 catalysts for oxidation reactions.	88
Table 4-2. Dispersion and average size of Pd in the Pd(2)/ CeO_2 . catalysts	92
Table 4-3. Pd species on the surface of the Pd(2)/ CeO_2 catalysts	101
Table 4-4. Surface and bulk Pd concentration of the Pd(2)/ CeO_2 catalysts.....	102
Table 4-5. CO oxidation activities of the Pd/ CeO_2 catalysts reported in the literatures.....	109

List of Figures

Fig. 2-1.	Light-off curves of methane combustion over the (a) bulk cobalt oxide catalysts, (b) mesoporous cobalt oxide catalysts and (c) methane conversion with time-on-stream in the methane combustion reaction over the m-Co ₃ O ₄ -0.01M catalyst at 450 °C.....	12
Fig. 2-2.	Light-off curves of methane combustion over the Pd(2)/Al ₂ O ₃ catalyst.....	14
Fig. 2-3.	Arrhenius plots for methane combustion over the m-Co ₃ O ₄ catalysts.....	16
Fig. 2-4.	TEM images of the (a) m-Co ₃ O ₄ , (b) m-Co ₃ O ₄ -0.01M and (c) m-Co ₃ O ₄ -1M catalysts.....	19
Fig. 2-5.	SEM images of the (a) m-Co ₃ O ₄ , (b) m-Co ₃ O ₄ -0.01M and (c) m-Co ₃ O ₄ -1M catalysts.....	20
Fig. 2-6.	(a) N ₂ adsorption-desorption isotherms and (b) pore size distribution of the m-Co ₃ O ₄ catalysts.....	22
Fig. 2-7.	N ₂ adsorption-desorption isotherms of the b-Co ₃ O ₄ catalyst	24
Fig. 2-8.	(a) XRD patterns of the m-Co ₃ O ₄ catalysts and (b) (311) peak of the m-Co ₃ O ₄ catalysts.....	27
Fig. 2-9.	Raman spectra of the m-Co ₃ O ₄ catalysts.....	28
Fig. 2-10.	H ₂ -TPR profiles of the m-Co ₃ O ₄ catalysts	30
Fig. 2-11.	O ₂ -TPD profiles of the m-Co ₃ O ₄ catalysts	33
Fig. 2-12.	XPS spectra of the m-Co ₃ O ₄ catalysts; (a) Full spectrum, (b) Co 2p and (c) O 1s.....	37
Fig. 3-1.	Light-off curves of methane oxidation over the Pd/SSZ-13 catalysts	48
Fig. 3-2.	(a) ²⁷ Al NMR and (b) ²⁹ Si NMR spectra of the Pd/SSZ-13 catalysts.....	51
Fig. 3-3.	N ₂ adsorption-desorption isotherms of the Pd/SSZ-13 catalysts.....	53
Fig. 3-4.	XRD patterns of the Pd/SSZ-13 catalysts	55
Fig. 3-5.	TGA profiles of the Pd/SSZ-13 catalysts	57

Fig. 3-6.	H ₂ O adsorption isotherms of the Pd/SSZ-13 catalysts.....	58
Fig. 3-7.	DRIFT spectra of the Pd/SSZ-13 catalysts obtained after H ₂ O adsorption	59
Fig. 3-8.	Raman spectra of the Pd/SSZ-13 catalysts.....	62
Fig. 3-9.	DRIFT spectra of the Pd/SSZ-13 catalysts obtained after CO adsorption.....	63
Fig. 3-10.	H ₂ -TPR profiles of the Pd/SSZ-13 catalysts	64
Fig. 3-11.	NH ₃ -TPD profiles of the SSZ-13 supports.....	66
Fig. 3-12.	HAADF-STEM and EDX mapping images of the Pd/SSZ-13 catalysts.....	68
Fig. 3-13.	Pd 3d XPS spectra of the Pd/SSZ-13 catalysts.....	69
Fig. 3-14.	Light-off curves of methane combustion over the Pd/SSZ-13 catalysts; dry and wet condition	72
Fig. 3-15.	Arrhenius plots for methane combustion over the Pd/SSZ-13 catalysts	74
Fig. 3-16.	Light-off curves of methane combustion over the Pd/SSZ-13 catalysts including Pd(1)/SSZ-13 (HTA-400R500C) catalyst.....	77
Fig. 3-17.	Methane conversion with time-on-stream in the methane combustion reaction over the Pd/SSZ-13 catalysts at 400 °C	79
Fig. 4-1.	Light-off curves of CH ₄ oxidation over the Pd(2)/CeO ₂ catalysts; (a) dry condition and (b) wet condition (5% H ₂ O)	86
Fig. 4-2.	Light-off curves of CO oxidation over the Pd(2)/CeO ₂ catalysts; (a) dry condition and (b) wet condition (5% H ₂ O)	87
Fig. 4-3.	HAADF-STEM images and EDX mapping of the (a) Pd(2)/CeO ₂ (N) and (b) Pd(2)/CeO ₂ (A) catalysts.....	90
Fig. 4-4.	XRD patterns of the Pd(2)/CeO ₂ catalysts	94
Fig. 4-5.	Raman spectra of the Pd(2)/CeO ₂ catalysts.....	96
Fig. 4-6.	H ₂ -TPR profiles of the Pd(2)/CeO ₂ catalysts	98
Fig. 4-7.	Pd 3d XPS spectra of the Pd(2)/CeO ₂ catalysts.....	100
Fig. 4-8.	(a) Normalized XANES and	

	(b) EXAFS spectra of the Pd(2)/CeO ₂ catalysts with PdO foil.....	104
Fig. 4-9.	The color of the Pd/CeO ₂ catalysts	106
Fig. 4-10.	(a) CO oxidation activities of the Pd(2)/CeO ₂ catalysts in terms of TOF, Arrhenius plots (b) for CO and (c) CH ₄ oxidation.....	111
Fig. 4-11.	(a) H ₂ -TPR profiles and (b) TGA profiles of the Pd(2)/CeO ₂ (A) catalysts calcined in air or N ₂ condition	113

Chapter 1. Introduction

1.1. Catalysts for low-temperature methane combustion

One of the most important issues over the global economic growth is the solution for the increasing energy demand. Although there is ongoing researches on the development of clean and renewable energies, the use of fossil fuel is still dominant. Among the available fossil fuel resources, natural gas has received much attention because of the pronounced increase in the shale gas production past few decades. In addition, it is accepted as clean energy source compared to the other fossil fuels because it emits less pollution, such as nitrogen oxides, sulfur oxides and hydrocarbons during combustion. As a result, the consumption of natural gas has been increasing rapidly in the past decades, which is used in various sectors, such as industrial, power, transport and others.

Therefore, due to the advantages of utilizing natural gas as energy source, large number of gasoline and diesel engines are being replaced by natural gas engines to meet the stringent environmental regulations. However, the presence of unburned methane in the exhaust gas of natural gas vehicles has become a serious problem for the clean environment because the global warming potential of methane is 25 times greater than that of CO_2 . One of the most effective methods for reducing methane emission is complete CH_4 oxidation to CO_2 and H_2O . However, complete methane oxidation at low temperature is still challenging because of the highly stable C-H bond in the non-polar CH_4 molecule. Therefore, developing highly active catalysts for the low temperature methane oxidation has gained much attention over the past decades.

Platinum-group metals have been widely used as active catalysts for the oxidation of CO and hydrocarbons. Among them, Pd-based catalysts are accepted

as the most active catalysts for the low temperature methane combustion . Because of their high cost, noble metal catalysts are generally prepared by dispersing a small amount of the precious metal on a support material, such as alumina, ceria, or zeolite . However, the Pd catalysts are vulnerable to the poisoning effects of H_2O and SO_2 , which are usually present in the exhaust gas of natural gas engines. Water can react with PdO particles to form inactive $\text{Pd}(\text{OH})_2$ and inhibit oxygen exchange between Pd and support . In the case of SO_2 -poisoning, the deactivation is explained by the formation of sulfates on Pd, which blocks active sites for the reaction . Therefore, developing highly active catalysts at low temperature that are resistant to the poisoning effects of H_2O and SO_2 is required for the industrial application. Mixed oxide catalysts, such as perovskite and spinel oxide catalysts are attractive alternatives because of their low price and high thermal stability . However, their catalytic activities are much lower than that of the Pd catalysts especially at the low temperature region, which need to be improved significantly for the industrial application.

1.2. Objectives

As mentioned earlier, the Pd-based noble metal catalysts are the most active catalysts for the methane combustion reaction. However, the volatile price of noble metals limits their industrial applications. Fortunately, transition metal oxide catalysts, such as spinel-type cobalt oxide catalysts, are attractive alternatives, although their catalytic activity must be improved for industrial applications. In chapter 2, the poor activity of bulk cobalt oxide catalyst was enhanced by two different methods. First, the textural property of the bulk catalyst was enhanced by the introduction of mesoporosity. Second, the synthesized mesoporous cobalt oxide catalysts were treated with nitric acid to further modify the surface structure and chemistry. The prepared catalysts were applied to the methane combustion reaction

and a significant enhancement in catalytic activity was observed for the acid-treated catalysts compared to the pristine catalyst. The properties of the acid-treated catalyst were investigated in detail using various characterization techniques.

Although it was possible to significantly increase the methane oxidation activity of the cobalt oxide catalyst by the acid treatment, the catalytic activity was still inferior than the noble metal catalysts. Because of the high cost, noble metal catalysts are generally prepared by dispersing a small amount of the precious metal on a support material. However, Pd catalysts are vulnerable to H₂O in the exhaust gas, which is known to severely inhibit the initial activity and cause deactivation during the long-term operation. One of the possible solutions for synthesizing the catalyst that is resistant to H₂O is using hydrophobic support. Among the various support materials, zeolite can be effective support for the methane oxidation catalyst because the hydrophobicity can be enhanced by increasing Si/Al₂ ratio . Zeolite can be easily dealuminated by steam treatment at high temperature, which is often called as hydrothermal treatment . In chapter 3, the effects of dealumination on Pd/SSZ-13 catalysts for methane combustion were investigated. Pd(1)/SSZ-13 (HTA), which was prepared by treating the catalyst hydrothermally at 750 °C, displayed extremely low catalytic activity. On the contrary, Pd(1)/SSZ-13 (DeAl) catalyst, which was prepared by treating the SSZ-13 support hydrothermally and subsequent Pd impregnation, exhibited superior catalytic activity for methane oxidation. Catalytic properties, including zeolite hydrophobicity, Pd location and states were investigated by using various characterization techniques to clarify the differences between the catalysts.

Because it was revealed that the hydrophobicity of the zeolite support was not critical factor for the catalytic activity, we decided to use other support material. Ceria is generally utilized for oxidation reactions owing to the redox properties arising from the Ce⁴⁺/Ce³⁺ cycle, strong interaction with supported metals and large oxygen storage capacity . Pd species in Pd/CeO₂ catalysts can exist in various

states and understanding the active phase of Pd for a specific reaction is important to synthesize a highly active catalyst with an appropriate Pd state . In chapter 4, the effects of Pd precursor on the state of Pd species in the Pd/CeO₂ catalysts were investigated. The Pd/CeO₂ catalysts were prepared using different Pd precursors and applied to CH₄ and CO oxidation. Significantly, the Pd/CeO₂ catalyst prepared using palladium nitrate (Pd(2)/CeO₂ (N)) was highly active toward CH₄ oxidation, whereas the catalyst prepared using palladium acetate (Pd(2)/CeO₂ (A)) exhibited high CO oxidation activity. The effects of the precursor on the catalytic activity and other properties were studied using various characterization techniques.

Chapter 2. Methane combustion over

mesoporous cobalt oxide catalysts:

Effects of acid treatment

2.1. Introduction

Natural gas is one of the most abundant energy sources on earth and can be used for electric power generation, heating, and transportation . Methane, a major component of natural gas, produces less pollution during combustion than conventional petroleum-based fuels . Thus, a large number of gasoline and diesel engines are being replaced by natural gas engines to reduce the emission of nitrogen oxides, sulfur oxides, and hydrocarbons. However, unburned methane is emitted from natural gas vehicles. Because the global warming potential of methane is 25 times greater than that of CO₂, methane emission regulation is being implemented for environmental protection . The catalytic combustion of methane ($\text{CH}_4 + 2\text{O}_2 \rightarrow \text{CO}_2 + 2\text{H}_2\text{O}$) is one of the most effective methods for reducing methane emissions from natural gas engines . However, methane is very stable because of its strong C–H bonds; methane oxidation requires high temperatures and consumes a large amount of energy. Therefore, catalysts for low-temperature methane oxidation are urgently required to reduce the energy consumption of this process .

Currently, Pd-based noble metal catalysts are the most widely used and most active catalysts for the methane combustion reaction . However, the volatile price of noble metals limits their industrial applications . Fortunately, transition metal oxide catalysts, such as perovskite oxides or spinel oxides, are attractive alternatives, although their catalytic activity must be improved for industrial

applications . Among these transition metal oxides, spinel-type cobalt oxide is widely used as an active catalyst for methane combustion reactions . However, the poor intrinsic activity of metal oxides relative to Pd catalysts limits their application in low-temperature methane oxidation reactions. To date, there have been many studies into methods to improve the catalytic activity of cobalt oxide catalysts, and one method for enhancing the catalytic activity of bulk cobalt oxide is to modify the structure of the catalyst by introducing mesoporosity . For example, using a mesoporous silica template, metal oxides with well-defined mesopores and high surface areas can be synthesized. These catalysts generally exhibit higher catalytic performance than conventional bulk catalysts because the mass transfer efficiency is enhanced in the ordered porous structures .

Recently, several researchers have reported that acid treatment is an effective method for enhancing the catalytic activity of bulk oxide materials, especially for oxidation reactions. For example, several researchers have studied the effects of acid treatment on perovskite catalysts . Perovskites are mixed metal oxides having the general formula ABO_3 , where the A-site ion is usually a lanthanide and the B-site ion is a transition metal . The acid treatment process results in the selective removal of the A-site cations, thus exposing the catalytically active B-site cations at the surface. Tang et al. reported a similar treatment for other metal oxides, such as spinel-type Co_3O_4 , which resulted in better catalytic activity than the fresh catalysts for the propane combustion reaction .

Previously, our group have successfully synthesized mesoporous spinel oxide catalysts via a nano-replication method and discovered that the mesoporous catalysts exhibit better catalytic activity for methane combustion than the bulk counterparts . Therefore, in this study, a mesoporous cobalt oxide catalyst was treated with various concentrations of nitric acid, and the prepared catalysts were applied to the methane combustion reaction. In addition, the effects of the acid treatment on the properties of the catalysts were investigated extensively using

various characterization methods.

2.2. Experimental

2.2.1. Catalyst preparation

The bulk cobalt oxide catalyst was prepared using the oxalate precipitation method. Specifically, $\text{Co}(\text{NO}_3)_2 \cdot 6\text{H}_2\text{O}$ (98%, Junsei) and $\text{Na}_2\text{C}_2\text{O}_4$ (99%, Junsei) were dissolved in distilled water. Both aqueous solutions were heated at 80 °C for 15 min and mixed under vigorous stirring. Then, the mixture was stirred at 80 °C for a further 30 min, and the precipitate was filtered. The powder was dried at 80 °C for 12 h and calcined at 550 °C for 3 h. The prepared catalyst was named as b- Co_3O_4 .

SBA-15, a mesoporous silica template, was synthesized using a well-established method. Briefly, Pluronic P123 triblock copolymer (Average Mn 5,800, Sigma-Aldrich) was dissolved in a solution of concentrated HCl (35% ~ 37%, Samchun) and distilled water. After the complete dissolution of P123, tetraethyl orthosilicate (98%, Sigma-Aldrich) was dropped into the solution, and the temperature of the solution was adjusted to 40 °C. The mixture was stirred at 40 °C for 24 h, followed by aging at 100 °C in an oven for 24 h. The resulting solid product was filtered with ethanol to remove any residual surfactant. Finally, the powder was dried at 80 °C for 12 h and calcined at 550 °C for 3 h.

The mesoporous cobalt oxide was synthesized via the nano-replication method using SBA-15 as a mesoporous template. $\text{Co}(\text{NO}_3)_2 \cdot 6\text{H}_2\text{O}$ (98%, Junsei) was dissolved in ethanol, and the solution was impregnated into the pores of SBA-15. After the impregnation process, the powder was dried at 80 °C for 12 h and calcined at 550 °C for 3 h. The silica template was removed by treating the catalyst

with a 2 M NaOH (98%, pellets, Sigma-Aldrich) solution. After filtration, the sample was dried at 80 °C for 12 h, and the template-free mesoporous cobalt oxide was obtained.

Mesoporous cobalt oxide powder (500 mg) was added to 50 mL of nitric acid (60%, Samchun) solution (either 1 or 0.01 M), and the suspension was stirred at 60 °C for 1 h. The samples were filtered and washed with deionized water. After drying at 80 °C for 12 h, the powder was calcined at 550 °C for 3 h. The acid-treated samples were denoted as m-Co₃O₄-1M or m-Co₃O₄-0.01M, depending on the concentration of nitric acid used.

2.2.2. Catalyst characterization

Nitrogen adsorption–desorption isotherms were obtained using a BELSORP-mini II (BEL Japan) apparatus, and the surface areas of the catalysts were calculated using the Brunauer–Emmett–Teller (BET) equation. The morphologies of the catalysts were observed by transmission electron microscopy (TEM) and scanning electron microscopy (SEM). TEM images of the catalysts were obtained using a JEM-3010 (Jeol) operated at 200 kV, and SEM images of the catalysts were obtained using a JSM-7800F Prime (Jeol). X-ray diffraction (XRD) measurements were conducted using a Rigaku SmartLab instrument with Cu-K α radiation ($\lambda = 1.541 \text{ \AA}$, 30 kV, 40 mA). Raman spectra were acquired using a LabRAM HR Evolution (HORIBA) with an Ar⁺ (532 nm) laser as the excitation source. Hydrogen temperature-programmed reduction (H₂-TPR) profiles were obtained using a BELCAT-B (BEL Japan) instrument. The catalyst (50 mg) was pretreated under a flow of He (50 mL/min) at 400 °C for 1 h. After cooling to 50 °C, the furnace temperature was increased to 700 °C at a ramping rate of 10 °C/min under a mixed flow of H₂ (2.5 mL/min) and Ar (47.5 mL/min). Hydrogen consumption was assessed using a thermal conductivity detector (TCD).

Oxygen temperature-programmed desorption (O₂-TPD) profiles were acquired using a gas chromatography–single quadrupole mass spectrometer (GC-MSD, 6890N GC-5975MSD, Agilent). The catalysts (50 mg) were pretreated under a flow of He (20 mL/min) at 400 °C for 1 h. After cooling to 50 °C, a mixed flow of O₂ (2 mL/min) and He (20 mL/min) was introduced into the reactor for 1 h. The physisorbed O₂ was removed at 100 °C for 30 min using a flow of He (20 mL/min). Finally, the furnace temperature was increased to 800 °C at a ramping rate of 10 °C/min under a flow of He (20 mL/min), and the desorbed O₂ was analyzed by GC-MSD. X-ray photoelectron spectroscopy (XPS) analysis was conducted using a VG Multilab 2000 spectrometer (Thermo Electron Corporation) with an Al K_α X-ray source (1486.6 eV).

2.2.3. Catalytic reaction system

The methane combustion reaction was carried out in a fixed-bed quartz reactor. The catalyst (200 mg) was mixed with 400 mg of α -Al₂O₃ beads to dissipate the heat generated by the reaction. The mixed gas was composed of 1000 ppm CH₄, 200 ppm NO, 3% CO₂, 5% H₂O, 20% O₂, and N₂ balance with a total flow rate of 200 mL/min was supplied to the catalyst bed by using a mass flow controller and syringe pump. The mass hourly space velocity was maintained at 60,000 mL g⁻¹ h⁻¹, and the outlet gas composition was analyzed using an on-line gas chromatograph (ACME 6500, Younglin) equipped with a TCD. The reaction temperature was increased from 350 to 500 °C in 25 °C intervals, and the methane conversion at each point was obtained after stabilization for 30 min.

The apparent activation energy for the methane combustion reaction was obtained when the methane conversion was less than 20% . We confirmed that there was no mass transfer limitation in this kinetic region based on the Weisz–Prater criterion . The reaction rate was calculated using equation (1) .

$$r = \frac{N \cdot X}{W} \quad (1)$$

Here, N represents the total flow rate of methane (mol s^{-1}), X denotes the methane conversion, and W is the catalyst weight (g). The activation energy (E_a) was calculated from an Arrhenius plot using equation (2).

$$\ln r = \frac{E_a}{RT} + c \quad (2)$$

2.3. Results

2.3.1. Catalytic performance

The methane combustion reaction was performed in a fixed-bed quartz reactor. The inlet gas composition was designed to mimic the exhaust gas composition of vehicles having a natural-gas-powered engine. A mixed gas containing N_2 , O_2 , CH_4 , CO_2 , NO , and H_2O was introduced into the reactor, and the reaction was carried out under lean-burn conditions, under which the O_2 concentration was 200-times higher than the CH_4 concentration. A bulk cobalt oxide catalyst was prepared using the conventional precipitation method, and the prepared bulk catalyst was treated with nitric acid to modify its surface structure and chemistry. The light-off curves are presented in Fig. 2-1(a), and the temperatures at which the methane conversion reached 50% (T_{50}) are summarized in Table 2-1. The methane conversion increased with increase in temperature, and T_{50} was used as a criterion for comparing the methane combustion activities of the catalysts. As shown in Fig. 2-1(a), the methane combustion activity increased

significantly after the acid treatment. Specifically, T_{50} decreased from 473 to 447 °C after acid treatment. However, the activity of the bulk catalyst was still inferior to that of the conventional Pd(2)/Al₂O₃ catalyst. As shown in Fig. 2-2, the T_{50} of the Pd(2)/Al₂O₃ catalyst prepared using the incipient impregnation method was 371 °C. Many researchers have reported that the poor intrinsic activity of the bulk oxides may hinder their potential catalytic activity. To overcome this problem, mesoporous cobalt oxide catalysts were synthesized using the nano-replication method with an SBA-15 silica template. The catalyst was treated with different concentrations of nitric acid and applied for catalytic methane combustion. Fig. 2-1(b) and Table 2-1 show that the catalytic activity of the mesoporous cobalt catalyst was superior to that of its bulk counterpart. In addition, the methane combustion activity increased after the acid treatment, although the catalytic activities of the m-Co₃O₄-1M and m-Co₃O₄-0.01M catalysts were almost identical. Table 2-1 shows that the T_{50} values of the acid-treated catalysts were 409 °C and 411 °C, both of which were lower than that of the fresh catalyst by 42 °C and 40 °C. Therefore, it can be concluded that the catalytic activity was enhanced significantly after acid treatment, although the concentration of acid was not a critical factor.

To investigate the long-term activity of the acid-treated catalyst, the activity of the m-Co₃O₄-0.01M catalyst was evaluated at 450 °C for 15 h. Fig. 2-1(c) shows the methane conversion with increasing time-on-stream. The methane conversion slightly decreased from 74% to 70% after 15-h reaction. Crucially, the reduction in methane conversion after 15 h was only 4%, suggesting that the acid-treated catalyst is stable under these reaction conditions.

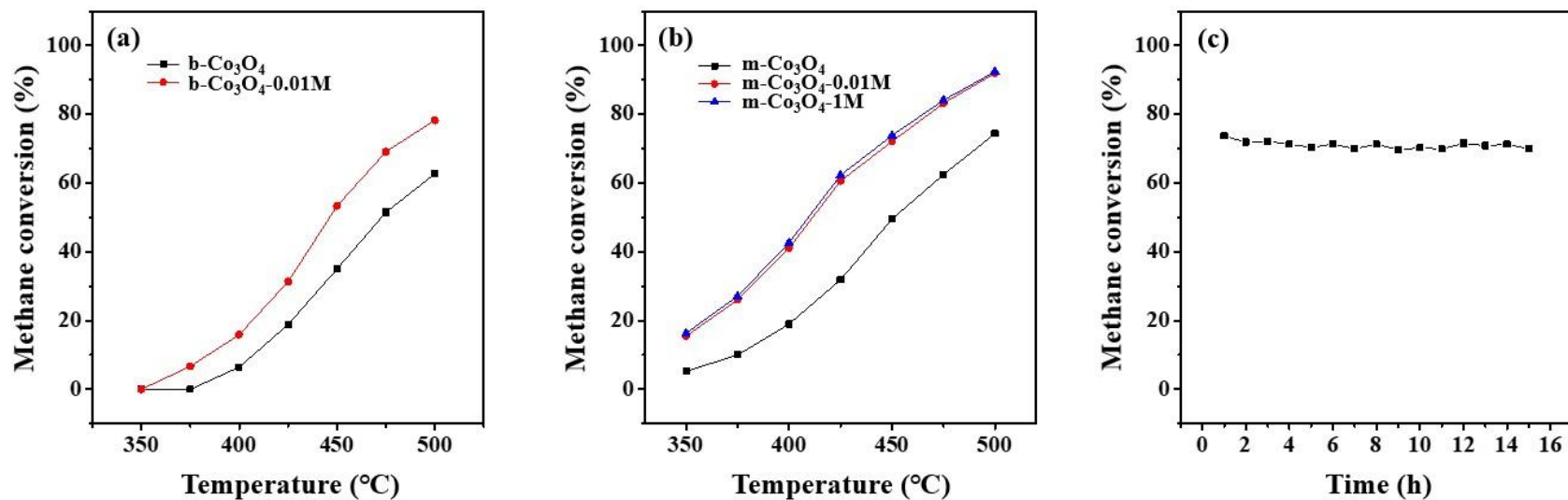


Fig. 2-1. Light-off curves of methane combustion over the (a) bulk cobalt oxide catalysts, (b) mesoporous cobalt oxide catalysts and (c) methane conversion with time-on-stream in the methane combustion reaction over the $m\text{-Co}_3\text{O}_4\text{-0.01M}$ catalyst at 450 °C.

Table 2-1. Catalytic activities (T_{50}) of the Co_3O_4 catalysts.

Catalyst	T_{50} (°C)
b-Co_3O_4	473
b-Co_3O_4-0.01M	447
.....	
m-Co_3O_4	451
m-Co_3O_4-0.01M	411
m-Co_3O_4-1M	409

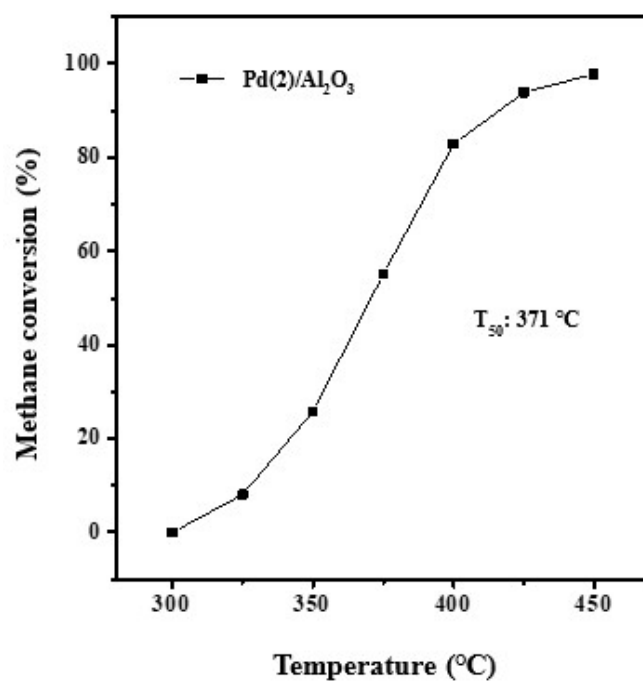


Fig. 2-2. Light-off curves of methane combustion over the Pd(2)/Al₂O₃ catalyst.

Kinetic studies of the methane combustion reaction over the cobalt oxide catalysts were carried out at methane conversions lower than 20%, and the activation energy of each catalyst was calculated from the slope of the Arrhenius plot, as shown in Fig. 2-3. Interestingly, the activation energy of the m-Co₃O₄-0.01M catalyst was 102 kJ/mol, which was much lower than that of the m-Co₃O₄ catalyst (130 kJ/mol). Considering that the lower activation energy is typically advantageous for catalytic reaction, the results were well in line with the superior catalytic activities of the acid-treated cobalt oxide catalysts. Thus, it can be concluded that the acid treatment reduced the reaction activation barrier, which allowed the acid-treated catalyst to oxidize methane at lower temperatures.

In order to compare the catalytic activities of the acid-treated catalysts with other transition metal oxide catalysts, T₅₀ values of the cobalt based catalysts reported in the literatures were summarized in Table 2-2. Although the acid-treated catalysts showed lower activity than the noble metal catalyst (Fig. 2-2), Table 2-2 clearly displays that the catalytic activities of the acid-treated catalysts were higher than other transition metal oxide catalysts reported in the literatures. To explain the enhanced catalytic activity of the acid-treated catalyst, the effects of acid treatment on the mesoporous cobalt oxide catalysts were investigated using various characterization techniques.

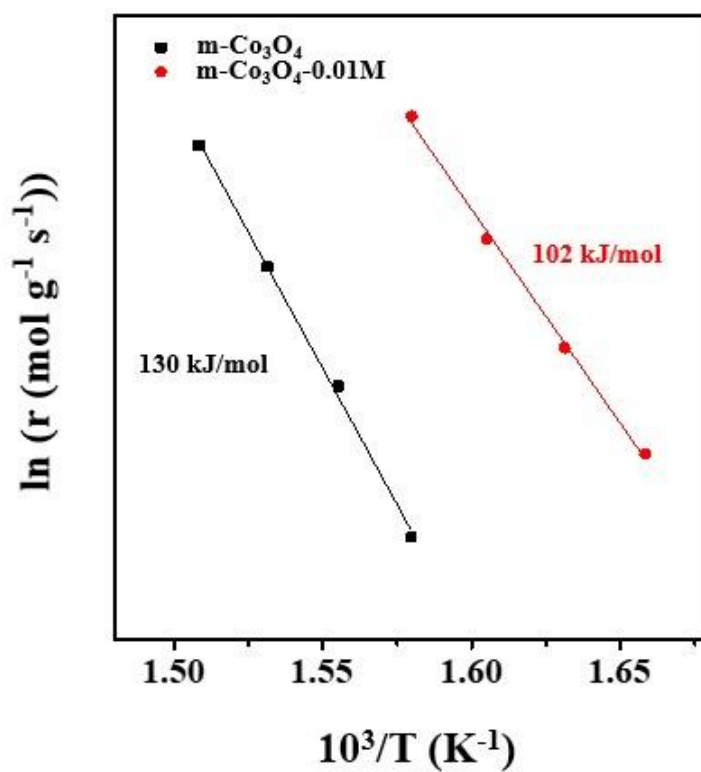


Fig. 2-3. Arrhenius plots for methane combustion over the $m\text{-Co}_3\text{O}_4$ catalysts.

Table 2-2. Catalytic activities of the cobalt based catalysts reported in the literatures.

Catalyst	T ₅₀ (°C)	Space velocity	Reactant	Ref.
LaCoO ₃	470	60,000 h ⁻¹	0.8% CH ₄ , 5% O ₂ , N ₂ balance	
Co _{3-x} Fe _x O ₄	520	60,000 mL g ⁻¹ h ⁻¹	0.5% CH ₄ , 4% O ₂ , N ₂ balance	
Co-Mg/Al mixed oxide	530	50,000 h ⁻¹	1% CH ₄ , air balance	

2.3.2. Catalyst characterization

TEM analysis was performed to confirm the mesoporous structure of the $m\text{-Co}_3\text{O}_4$ catalysts. As described in the experimental section, the catalysts were prepared using a nano-replication method. Specifically, the cobalt precursor was impregnated into the channels of the SBA-15 template, and a template removal process was carried out to yield the mesoporous cobalt oxide catalysts. As shown in Fig. 2-4, a longitudinal arrangement of mesopores can be observed for the fresh catalyst, which is a characteristic of the SBA-15 template. Therefore, we concluded that the $m\text{-Co}_3\text{O}_4$ sample well-replicated the SBA-15 template, indicating the formation of an ordered mesoporous structure. Further, the longitudinal arrangement of mesopores was still detected in the acid-treated catalyst. Hence, the TEM images confirmed that the acid treated catalysts still retained the original mesoporous structure.

Further morphological studies were carried out using SEM analysis, as shown in Fig. 2-5. Agglomerates of nanorods can be observed in the SEM images, which result from the pore structure of the SBA-15 template. In addition, the images show that the morphology of the catalyst was clearly affected by the acid treatment. For instance, the surface of the catalyst became rougher and the original nanorod structure was divided into thinner wires after acid treatment. Based on the TEM and SEM images, we concluded that the main mesoporous structure was maintained after the acid treatment, although the morphology of the catalyst surface was altered. On the basis of this result, we hypothesize that abundant defect sites, such as steps or kinks, could have been generated during the acid treatment.

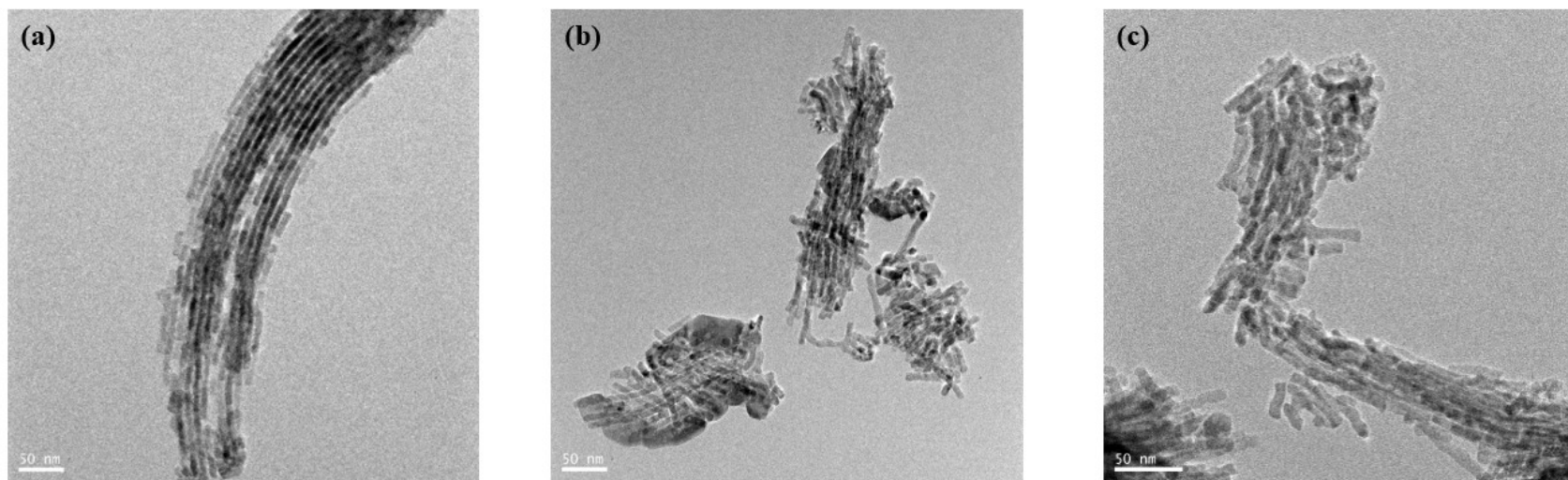


Fig. 2-4. TEM images of the (a) $\text{m-Co}_3\text{O}_4$, (b) $\text{m-Co}_3\text{O}_4\text{-0.01M}$ and (c) $\text{m-Co}_3\text{O}_4\text{-1M}$ catalysts.

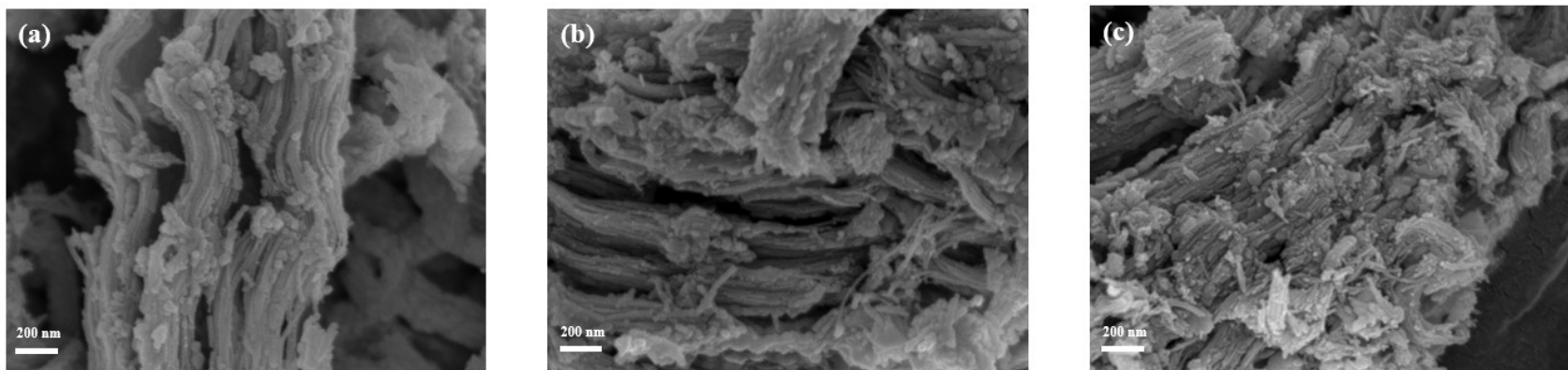


Fig. 2-5. SEM images of the (a) m-Co₃O₄, (b) m-Co₃O₄-0.01M and (c) m-Co₃O₄-1M catalysts.

The textural properties of the cobalt oxide catalysts were investigated using N₂ adsorption–desorption measurements. As shown in Fig. 2-6(a), the isotherms of the mesoporous cobalt oxide catalysts can be classified as type-IV with an H1 hysteresis loop, which indicates the presence of a mesostructure with cylindrical channels . The pore size distribution was obtained using the Barrett–Joyner–Halenda (BJH) method, and the results are shown in Fig. 2-6(b). All the mesoporous cobalt oxide catalysts exhibited a narrow pore size distribution centered at 3.8 nm, indicating that the ordered mesoporous structure was maintained even after the acid treatment. The BET surface areas and pore volumes of the mesoporous catalysts are listed in Table 2-3. For comparison, the textural properties of the bulk catalyst are shown in Fig. 2-7 and listed in Table 2-4. As expected, the introduction of mesopores significantly improved the textural properties of the bulk catalyst. For instance, the surface areas of the mesoporous cobalt oxide catalysts (100–107 m²/g) were much larger than those of the bulk cobalt oxide catalyst (14 m²/g), and this can be ascribed to the ordered mesoporous structure . Interestingly, the pore volume of the mesoporous catalyst slightly increased after acid treatment, which indicates that pore enlargement occurred. Nonetheless, the differences in the textural properties of the fresh and acid-treated catalysts did not significantly affect the catalytic activity for the methane oxidation reaction.

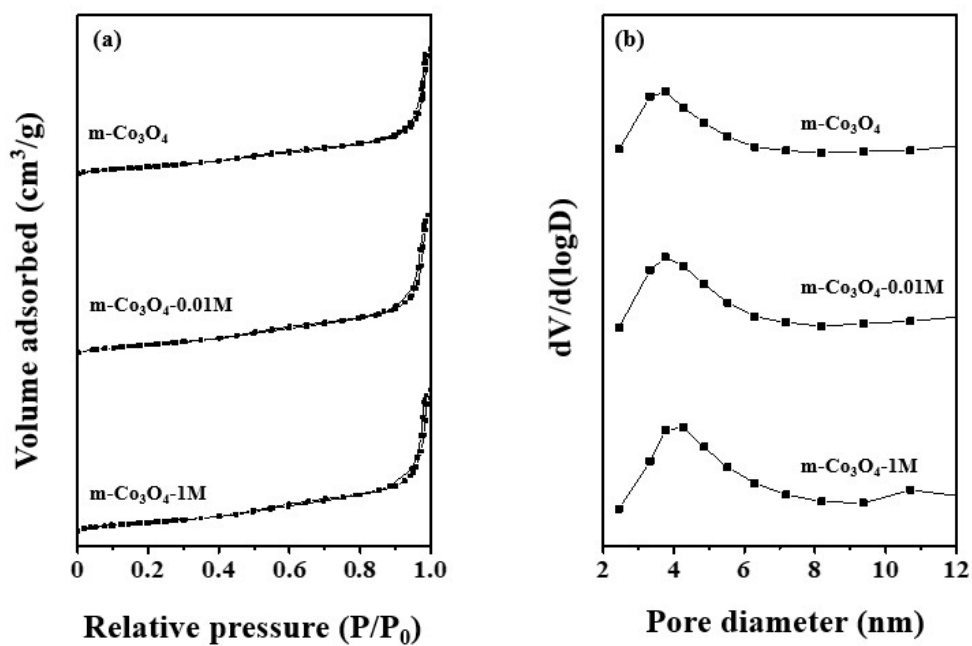


Fig. 2-6. (a) N_2 adsorption-desorption isotherms and (b) pore size distribution of the $m\text{-Co}_3\text{O}_4$ catalysts.

Table 2-3. Textural properties of the m-Co₃O₄ catalysts.

Catalyst	Surface area (m ² /g)	Pore volume (cm ³ /g)
m-Co ₃ O ₄	107	0.39
m-Co ₃ O ₄ -0.01M	105	0.44
m-Co ₃ O ₄ -1M	100	0.43

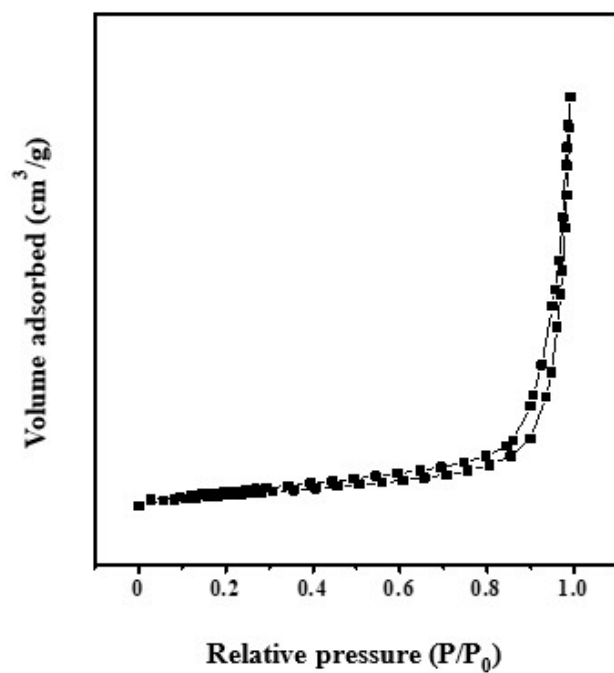


Fig. 2-7. N₂ adsorption-desorption isotherms of the b-Co₃O₄ catalyst.

Table 2-4. Textural property of the b-Co₃O₄ catalyst.

Catalyst	Surface area (m ² /g)	Pore volume (cm ³ /g)
b-Co ₃ O ₄	14	0.13

The crystal structure of the mesoporous cobalt oxide catalyst was investigated using XRD analysis. As shown in Fig. 2-8(a), diffraction peaks at 31.1° , 36.9° , 44.6° , 59.2° , and 65.1° were observed, which correspond to the spinel structure of Co_3O_4 . The XRD patterns of all catalysts are almost identical, and the XRD patterns of the acid-treated catalysts indicate that they are also composed of crystalline spinel-type Co_3O_4 . The most intense reflection, (311), was analyzed in detail at a slow scan rate ($0.1^\circ/\text{min}$) to enable a precise analysis of the crystal structure. As shown in Fig. 2-8(b), the (311) reflection shifted from 37.0° to 36.9° after acid treatment. This shift toward a lower angle indicates an increase in the lattice parameter of the Co_3O_4 phase.

Raman spectra were also obtained to examine the crystal structure of the catalyst further. As shown in Fig. 2-9, peaks corresponding to the E_g , F_{2g} , and A_{1g} symmetry bands of Co_3O_4 were observed. According to the literature, the main band at 668 cm^{-1} (A_{1g} symmetry) can be ascribed to the characteristic octahedral sites (i.e., CoO_6). Because Co^{3+} species occupy the octahedral sites of the Co_3O_4 structure, the A_{1g} peak arises from the Raman vibration of the $\text{Co}^{3+}\text{--O}^{2-}$ bonds. After the acid treatment, the A_{1g} peak shifted from 668 to 656 cm^{-1} and, then, further to 658 cm^{-1} . This redshift indicates that the acid treatment induced lattice distortion and caused residual stress in the original Co_3O_4 spinel structure, suggesting that defects had been formed. Lattice defects are known to be beneficial for the oxidation reaction because they provide vacancy sites for the adsorption and migration of molecular oxygen.

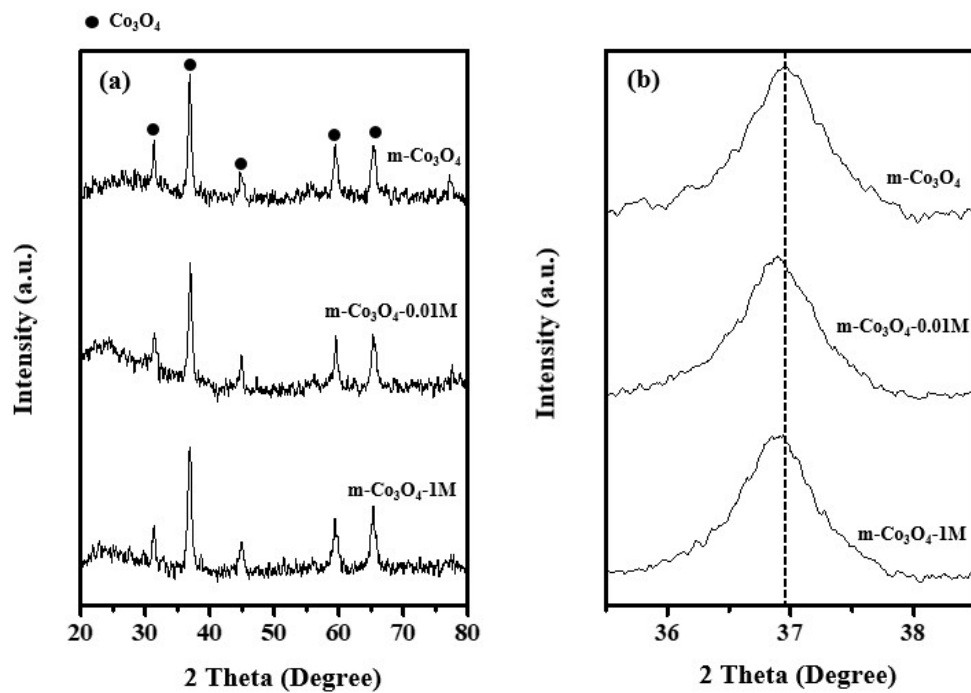


Fig. 2-8. (a) XRD patterns of the $\text{m-Co}_3\text{O}_4$ catalysts and (b) (311) peak of the $\text{m-Co}_3\text{O}_4$ catalysts.

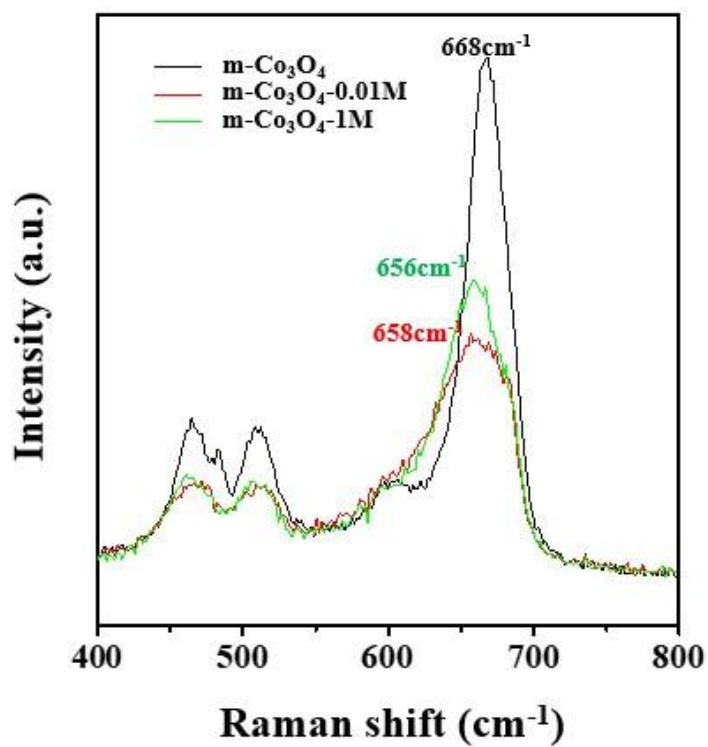


Fig. 2-9. Raman spectra of the $m\text{-Co}_3\text{O}_4$ catalysts.

Hydrogen TPR experiments were conducted to study the redox properties of the mesoporous cobalt oxide catalysts. Fig. 2-10 shows the TPR profiles of the catalysts. Two reduction peaks can be seen in the profiles of each catalyst. The first peak at around 310 °C can be attributed to the reduction of Co_3O_4 to CoO , and the second peak near 450 °C can be ascribed to the reduction of CoO to metallic Co . Fig. 2-10 clearly shows the shifts of the reduction peaks to lower temperatures in the acid-treated catalysts; the first peak shifted from 465 to 436 °C and the second peak shifted from 341 to 309 °C. These results indicate that the reducibility of the cobalt catalyst was significantly enhanced after acid treatment. The reducibility of metal oxide is related to the formation of oxygen vacancies, which indicates the tendency of the oxide to lose oxygen. Hence, the enhancement of reducibility will be beneficial for the catalytic combustion of methane. In addition, the hydrogen consumption corresponding to each peak was calibrated after the deconvolution process, and the results of the quantitative analysis are summarized in Table 2-5. Interestingly, the hydrogen consumption corresponding to the second peak was almost constant irrespective of acid treatment, although that corresponding to the first peak decreased after the acid treatment. This result indicates that a fraction of the Co^{3+} ions was reduced to Co^{2+} ions during the acid treatment.

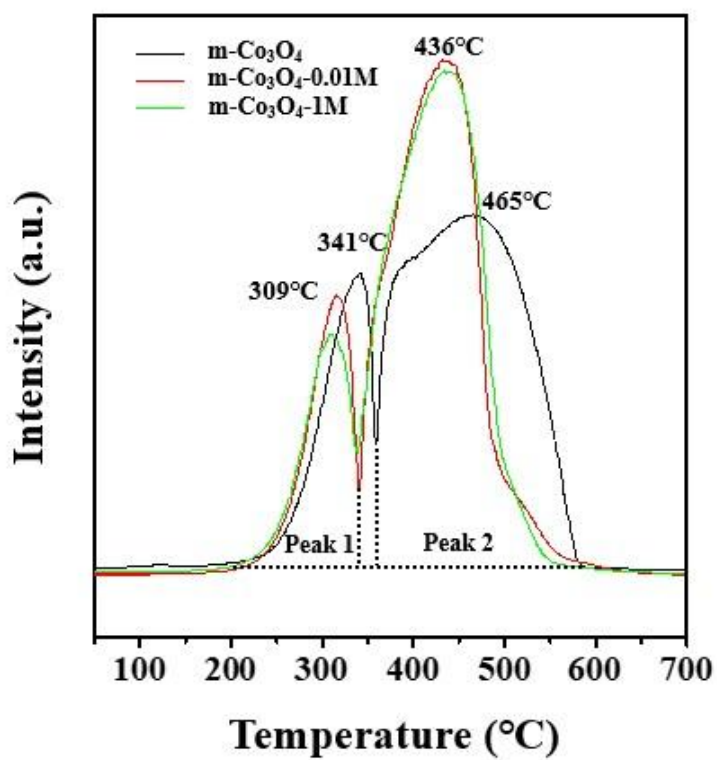


Fig. 2-10. H₂-TPR profiles of the m-Co₃O₄ catalysts.

Table 2-5. Hydrogen consumption during the H₂-TPR experiments.

Catalyst	Hydrogen consumption (mmol/g)	
	Peak 1	Peak 2
m-Co ₃ O ₄	3.6	11.5
m-Co ₃ O ₄ -0.01M	3.1	11.5
m-Co ₃ O ₄ -1M	2.9	11.4

O₂-TPD analysis was performed to identify the oxygen species in the cobalt oxide catalysts. As shown in Fig. 2-11, various oxygen species were desorbed with increase in temperature. For instance, chemisorbed oxygen desorbs below 300 °C and is known to participate in the catalytic oxidation reaction because of its high mobility. In contrast, lattice oxygen desorbs at temperatures higher than 450 °C because of the strong bonds in the crystal structure of cobalt oxide. Therefore, the low-temperature peak (< 300 °C) can be ascribed to the desorption of surface reactive oxygen species, whereas the medium-temperature peak between 400 and 600 °C can be assigned to the surface lattice oxygen. Finally, the high-temperature peak (> 700 °C) represents the release of bulk lattice oxygen arising from the decomposition of Co₃O₄. The quantification results for the oxygen desorption corresponding to each peak are summarized in Table 2-6. The amounts of desorbed chemisorbed oxygen for the acid-treated catalysts are 5.6 and 6.3 a.u., both of which are much larger than that of the fresh catalyst (1.4 a.u.). Therefore, we hypothesize that abundant oxygen vacancies were easily generated on the surfaces of the acid-treated catalysts. Under oxygen-rich conditions, oxygen can be adsorbed at the vacancy sites, thus generating active oxygen species. These active oxygen species were desorbed at temperatures below 300 °C during the TPD experiment, resulting in the larger peak areas observed for the acid-treated catalysts.

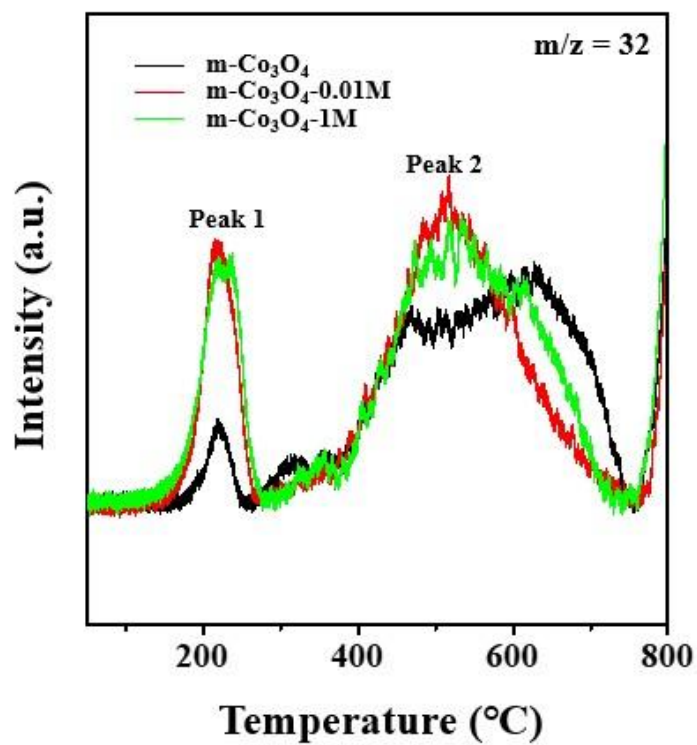


Fig. 2-11. O₂-TPD profiles of the m-Co₃O₄ catalysts.

Table 2-6. Oxygen desorption during the O₂-TPD experiments.

Catalyst	Oxygen desorption (a.u.)	
	Peak 1	Peak 2
m-Co ₃ O ₄	1.4	25.9
m-Co ₃ O ₄ -0.01M	5.6	23.2
m-Co ₃ O ₄ -1M	6.3	24.5

XPS analysis was conducted to obtain further information about the composition and chemical state of the catalyst surface. Fig. 2-12(a) displays the full XPS spectrum of the m-Co₃O₄ catalysts. Since the catalyst was treated with NaOH solution to remove silica template, it could be contaminated with sodium species. Choya et al. reported that the residual sodium could induce negative impact on the catalytic activity of Co₃O₄ catalyst. However, it was confirmed that the residual sodium species was removed during the filtration process because Na 1s spectrum (~1070 eV) was not detected. In addition, it was also confirmed that the acid treated catalysts did not possess any residual nitrogen species resulting from the nitric acid treatment because N 1s spectrum (~400 eV) was not observed. In addition, high-resolution Co 2p and O 1s spectrum of the catalysts are shown in Fig. 2-12(b) and (c), respectively. The Co 2p XPS spectrum of the catalysts exhibited typical characteristics of Co₃O₄. The Co 2p spectrum displays spin-orbit splitting into the 2p_{1/2} and 2p_{3/2} components. In addition, a satellite peak was observed, which is consistent with tetrahedrally coordinated Co²⁺ ions. For quantitative analysis, the Co 2p_{3/2} spectrum was deconvoluted into two components: the component at 780.7 eV can be assigned to Co²⁺ species, whereas that at 779.3 eV can be assigned to Co³⁺ species. In addition, to ensure accuracy in the deconvolution process, the spin-orbit doublet splitting was set to 15.2 eV with a fixed 2:1 ratio for the 2p_{3/2}-to-2p_{1/2} peak area. Following deconvolution, the ratios of surface Co²⁺ and Co³⁺ were calculated, and the results are summarized in Table 2-7. As shown in the table, the ratio of surface Co²⁺ was higher for the acid-treated catalysts than the fresh catalysts. Therefore, a small fraction of the Co³⁺ ions was reduced to Co²⁺ during the acid treatment, which is consistent with the H₂-TPR results.

The O 1s XPS spectra of the catalysts are shown in Fig. 2-12(c). Using a similar deconvolution method as used for the Co species, the O 1s peak was fitted

with two components: one corresponding to lattice oxygen (530.0 eV) and one corresponding to surface chemisorbed oxygen species (531.4 eV) . Table 2-7 summarizes the ratio of chemisorbed oxygen (O_{chem}) and lattice oxygen (O_{latt}) for each catalyst and clearly shows that the amount of chemisorbed oxygen increased after the acid treatment. In addition, the ratios of surface lattice oxygen to total cobalt species were calculated from the XPS results. The surface $O_{\text{latt}}/Co_{\text{total}}$ ratios of the acid treated catalysts were lower than that of the fresh catalyst, which further supported the hypothesis of oxygen vacancy formation. Thus, these results lead us to a similar conclusion to that obtained from the O_2 -TPD and XPS analyses. As discussed earlier, chemisorbed oxygen is more mobile than lattice oxygen and is, thus, expected to participate more actively in the oxidation reaction . Therefore, the abundance of active chemisorbed oxygen in the acid-treated catalysts could be the reason for their enhanced catalytic activity for the methane oxidation reaction.

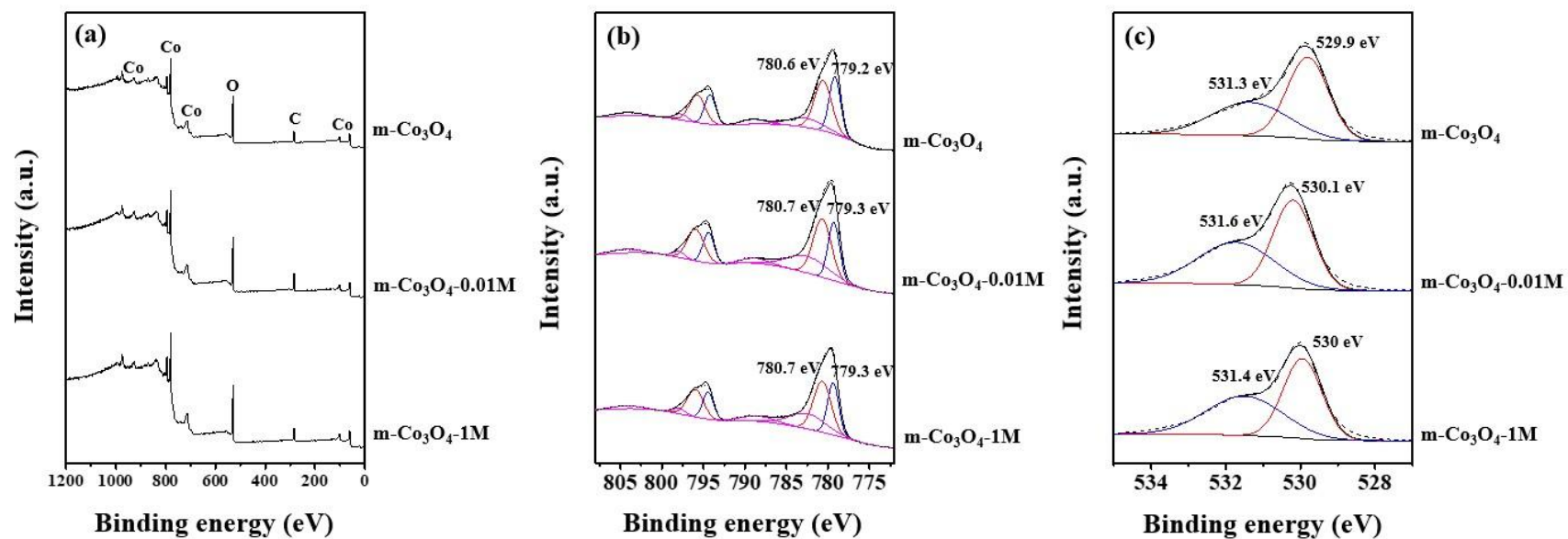


Fig. 2-12. XPS spectra of the m-Co₃O₄ catalysts; (a) Full spectrum, (b) Co 2p and (c) O 1s.

Table 2-7. Cobalt and oxygen species on the surface of the m-Co₃O₄ catalysts obtained from XPS analysis.

Catalyst	Co ²⁺ /Co ³⁺	O _{chem} /O _{latt}	O _{latt} /Co _{total}
m-Co ₃ O ₄	1.33	0.76	1.22
m-Co ₃ O ₄ -0.01M	1.56	0.92	1.07
m-Co ₃ O ₄ -1M	1.58	0.98	1.06

2.4. Discussion

In this work, the methane oxidation activity of a bulk cobalt oxide catalyst was enhanced by the introduction of mesopores and acid treatment. As discussed on our previous study, the improvement of catalytic activity after the addition of mesoporosity is understood as a result of the enhanced mass transfer efficiency of the bulk material in the presence of an ordered mesoporous structure . However, the effect of the acid treatment is not straightforward; therefore, the catalysts were further characterized to clarify the origin of the activity enhancement. The TEM images and N₂ adsorption-desorption isotherms confirmed that the ordered mesoporous structure was maintained even after acid treatment. As shown in Table 2-3, the surface areas and pore volumes of the catalysts were almost identical. Therefore, acid treatment had a negligible effect on the textural properties of the catalysts. However, a slight distortion from the original structure was observed in the TEM and SEM images, suggesting that defect sites, such as steps or kinks, could be generated during the acid treatment process.

XRD and Raman analyses provided detailed information about the crystal structures of the catalysts. XRD analysis showed that the lattice parameter increased slightly after the acid treatment. One possible explanation for the lattice expansion is the formation of oxygen vacancies. Once oxygen vacancies have been generated, Co³⁺ ions must be reduced to Co²⁺ ions to achieve charge balance . Because the size of Co²⁺ ions is larger than that of Co³⁺ ions, lattice expansion occurs to reduce the lattice strain . A similar result was observed in the Raman spectra. Specifically, the A_{1g} peaks of the m-Co₃O₄-0.01M and m-Co₃O₄-1M catalysts were observed at 656 and 658 cm⁻¹, respectively, which are lower than that of the fresh catalyst (668 cm⁻¹). Because the A_{1g} peak originates from the vibration of the Co³⁺-O²⁻ bond, such a redshift indicates an increase in the bond

length . Thus, acid treatment resulted in lattice distortion and residual stress in the original crystal structure, which further supports our hypothesis of defect site formation.

In addition, the formation of oxygen vacancies was further confirmed by H₂-TPR and Co 2p XPS analysis, which revealed that the acid-treated catalysts possessed larger amounts of Co²⁺ compared to the fresh catalyst. As discussed earlier, Co³⁺ must be reduced to Co²⁺ for charge balance after oxygen vacancy formation. Oxygen vacancies are known to be beneficial for the generation of chemisorbed oxygen because gas-phase oxygen can be adsorbed on these vacant sites. Such surface chemisorbed oxygen species (O₂²⁻, O⁻) are more mobile than lattice oxygen (O²⁻), which implies that it can be easily utilized and recycled during the oxidation reaction . Therefore, the reducibility enhancement observed in the H₂-TPR experiment can be explained by the abundance of mobile oxygen species in the acid-treated catalysts.

Quantitative analysis of the mobile chemisorbed oxygen species was carried out based on the O₂-TPD and O 1s XPS spectra. Both characterization methods revealed that the acid-treated catalysts contained larger amounts of surface chemisorbed oxygen species than the fresh catalyst. This can be explained on the basis of oxygen vacancy formation. Under oxygen-rich conditions, such as during oxidation reactions, oxygen is adsorbed on the vacancy sites and catalytically active oxygen species are generated. As discussed above, the surface chemisorbed oxygen is more mobile than lattice oxygen. In addition, the chemisorbed oxygen species are strongly electrophilic and attack organic molecules in regions of high electron density, thus resulting in the degradation of the organic framework . Zasada et al. reported that the activation energy of C-H bond becomes lower when the surface of cobalt oxide is abundant with reactive oxygen species . Therefore, the abundance of surface chemisorbed oxygen may explain the lower activation energy barrier of the methane combustion for the acid-treated catalysts. However,

the catalytic activities of the m-Co₃O₄-1M and m-Co₃O₄-0.01M catalysts were similar. Therefore, it can be concluded that the catalytic activity of the mesoporous cobalt oxide catalyst can be enhanced by simple acid treatment, but the acid concentration is not a critical factor.

Chapter 3. Effects of dealumination on the methane combustion activity of Pd/SSZ-13 catalysts

3.1. Introduction

The natural gas production has been increasing rapidly in the world for past few decades because of the shale gas revolution . In addition, natural gas is considered as clean energy source compared to other fossil fuels because of less pollutant emission . Therefore, the number of liquefied natural gas (LNG) vehicles is also continuously increasing . However, methane slip, in other words, unburned methane is emitted from the LNG engines. It has been serious problem for the environment because the global warming potential of methane is 25 times higher than that of CO₂ . The most efficient method for eliminating methane in the exhaust gas is the complete oxidation of methane to CO₂. However, methane is very inert chemical because of the high symmetry and low polarizability . Therefore, active catalyst is required in order to oxidize methane at low temperature and save energy consumption.

Supported Pd catalysts are accepted as the most active catalysts for the methane combustion reaction . However, the Pd catalysts are vulnerable to H₂O in the exhaust gas, which is known to severely inhibit the initial activity and cause deactivation during the long-term operation . One of the possible solutions for synthesizing the catalyst that is resistant to H₂O is to use hydrophobic support. Among the various support materials, zeolite can be effective support for the

methane oxidation catalyst because the hydrophobicity can be enhanced by increasing Si/Al₂ ratio . Zeolite can be easily dealuminated by steam treatment at high temperature, which is often referred to as hydrothermal treatment .

The effects of hydrothermal aging on catalytic activities of Pd/zeolite catalysts have been studied by various groups. Wang et al. reported that CO oxidation activity and NO_x storage capacity of Pd/SSZ-13 catalyst decreased after thermal aging at harsh condition (900 °C) . They claimed that the severe damage to the SSZ-13 structure and sintering to the bulk PdO_x particles on the zeolite surface were the reasons for the activity loss. On the contrary, our group reported that the NO_x storage ability and CO oxidation activity of Pd/SSZ-13 catalyst can be enhanced by the hydrothermal treatment at 750 °C . The hydrophobic zeolite exhibited higher NO_x storage capacity in the presence of H₂O because the concentration of dehydrated Pd ions increased after the dealumination. However, to the best of our knowledge, there are few papers that investigated the effects of hydrothermal treatment on the methane oxidation activity of the Pd/zeolite catalysts. In this contribution, we attempted to apply the Pd/SSZ-13 catalyst to the methane oxidation reaction and improve the activity by the dealumination process. In addition, the catalysts were investigated by various characterization techniques to elucidate the change in catalytic activity after the dealumination. It was revealed that zeolite hydrophobicity, state and location of Pd species were all affected by the hydrothermal treatment. Among them, the Pd state and location were the critical factors for determining the methane oxidation activity.

3.2. Experimental

3.2.1. Catalyst preparation

Since the active phase for the methane oxidation is accepted as PdO, all Pd/SSZ-13 catalysts were prepared by incipient impregnation method instead of ion exchange method. First, Pd was impregnated on the H-SSZ-13 (Si/Al₂ = 23, Heesung catalysis) using Pd(NO₃)₂·2H₂O (Sigma Aldrich) by incipient impregnation method with Pd loading of 1 wt%. After the impregnation, the catalyst was dried at 80 °C overnight and calcined at 500 °C for 2 h. The as-made catalyst was denoted as Pd(1)/SSZ-13.

In order to study the effects of dealumination, Pd(1)/SSZ-13 (HTA) catalyst was prepared by treating the Pd(1)/SSZ-13 catalyst at 750 °C for 20 h in the presence of 10% H₂O and 15% O₂ (N₂ balance).

However, our previous studies revealed that the hydrothermal treatment can disintegrate PdO nanoparticles to isolated Pd ions, which are less active in the methane combustion reaction. Therefore, another catalyst was prepared by slightly different method. First, H-SSZ-13 was hydrothermally aged in the same condition that was described earlier. Then, Pd was impregnated on the dealuminated H-SSZ-13 by incipient impregnation method with Pd loading of 1 wt%. The catalyst was dried at 80 °C overnight and calcined at 500 °C for 2 h. The as-made catalyst was denoted as Pd(1)/SSZ-13 (DeAl).

3.2.2. Catalyst characterization

The textural properties of the samples were examined by solid state magic angle spinning nuclear magnetic resonance (MAS NMR), N₂ adsorption-desorption and X-ray diffraction (XRD) analysis. Solid state ²⁷Al and ²⁹Si MAS NMR experiments were conducted using 500 MHz Bruker Avance III HD (Bruker, German) under room temperature. 4 mm MAS probe and spinning rate of 10 kHz were used to measure the data. N₂ adsorption-desorption experiments were

conducted using a BELSORP-mini II (BEL Japan). The samples were degassed at 200 °C for 3 h under vacuum to eliminate adsorbed impurities on the catalysts. The surface areas were calculated using the Brunauer-Emmett-Teller (BET) equation, while the micropore volumes were obtained from the t-plot. XRD analysis was carried out on a SmartLab (Rigaku) system (30 mA, 40 kV).

The hydrophobicity of the catalysts was examined by thermogravimetric analysis (TGA), H₂O adsorption isotherms and diffuse reflectance infrared Fourier transform spectroscopy (DRIFTS). TGA analysis was conducted using a Discovery TGA (TA Instruments) apparatus to quantify the amount of desorbed H₂O. The temperature was heated to 500 °C under air condition (5 °C/min). H₂O adsorption isotherms were obtained using 3 Flex (Micrometrics). The samples were pre-treated at 300 °C for 4 h to eliminate impurities and the experiments were conducted at 40 °C. DRIFTS experiments were performed in a diffuse reflectance cell (Praying Mantis, Harrick) installed in a Fourier transform infrared (FT-IR) spectrometer (iS-50, Thermo Fisher Scientific) with an MCT detector (32 scans, resolution of 4 cm⁻¹). Pre-treatment was conducted to eliminate any impurities under N₂ condition at 300 °C for 1 h and the total flow rate was fixed at 50 mL/min. H₂O adsorption was conducted at 120 °C and DRIFT spectra were collected after N₂ purging.

The characterization of Pd state was examined by Raman analysis, DRIFTS, H₂ temperature programmed reduction (H₂-TPR) and NH₃ temperature programmed desorption (NH₃-TPD). Raman spectra were obtained from a Raman spectrometer II (DXR2xi) with the samples excited at 532 nm. DRIFTS spectra were collected by pre-treating the samples under N₂ condition at 300 °C for 1 h. Saturation with CO molecules was conducted to every sample for 30 min, followed by N₂ purging for 30 min. DRIFTS spectra were obtained by subtracting background spectra collected before the saturation of CO molecules. H₂-TPR was operated on a BELCAT II system. Pre-treatment was conducted before the analysis

with 50 mL/min Ar at 300 °C. H₂-TPR profiles were obtained by elevating the temperature from -80 °C to 300 °C with 30 mL/min of 5% H₂, balanced with Ar (10 °C/min). NH₃-TPD was operated on a BELCAT B system. Pre-treatment was conducted at 300 °C for 1 h in He gas and then cooled to 50 °C. NH₃ adsorption was conducted with 10% NH₃, balanced with He. After removing the physically adsorbed NH₃ by flowing He gas at 100 °C for 1 h, NH₃-TPD profiles were obtained by elevating the temperature up to 700 °C under He gas.

The characterization of Pd location was examined using high-angle annular dark-field scanning transmission electron microscopy (HAADF-STEM) and X-ray photoelectron spectroscopy (XPS). HAADF-STEM was conducted on a JEM-ARM200F (JEOL) with a spherical aberration corrector (200 kV). XPS was operated on a K-alpha spectrometer (Thermo Fischer Scientific). The C 1s reference peak (284.6 eV) was utilized to correct the binding energies.

3.2.3. Catalytic reaction system

CH₄ combustion was operated in a quartz reactor. The catalysts were mixed with SiO₂ beads to disperse heat generated from the reaction. The feed consisted of 1,000 ppm CH₄, 15% O₂, 5% H₂O and N₂ balance flowed into the reactor (60,000 mL/g_{cat}·h). The outlet feed gas composition was analyzed via online gas chromatography (Younglin 6500) with a thermal conductivity detector (TCD) and flame ionization detector (FID). The CH₄ conversion was determined after stabilization for 30 min in the range of 300 to 450 °C at 25 °C intervals.

Activation energy for the methane combustion reaction was obtained when the methane conversion was less than 20%. The activation energy was calculated from the slope of the Arrhenius plot.

The catalytic stability was examined from long-term operation, which was conducted for 30 h at 400 °C. Deactivation rate was calculated after normalizing

the initial methane conversion as 1.

3.3. Results

3.3.1. Catalytic performance

Herein, the effects of dealumination on the Pd/SSZ-13 catalysts were investigated with 3 different catalysts; Pd(1)/SSZ-13 (pristine catalyst), Pd(1)/SSZ-13 (HTA), which was prepared by hydrothermal treating the pristine catalyst and Pd(1)/SSZ-13 (DeAl), which was prepared by hydrothermal treating the SSZ-13 support and subsequent Pd impregnation. The prepared Pd/SSZ-13 catalysts were applied to the methane combustion reaction. The Pd(1)/SSZ-13 (HTA) exhibited extremely low activity compared to the other catalysts; it could not oxidize methane at temperature lower than 450 °C (Fig. 3-1). On the other hand, the Pd(1)/SSZ-13 (DeAl) exhibited the highest activity among the Pd/SSZ-13 catalysts. The T_{50} of the Pd(1)/SSZ-13 (DeAl) was 386 °C, which was 23 °C lower than that of the pristine catalyst (Table 3-1). This results imply that the hydrothermal treatment is not always beneficial for the methane oxidation activity; Pd should be impregnated after hydrothermal treating the zeolite support in order to synthesize highly active catalyst for the methane combustion. In order to explain the change of the catalytic activity after the hydrothermal treatment, the catalysts were investigated extensively by using various characterization techniques.

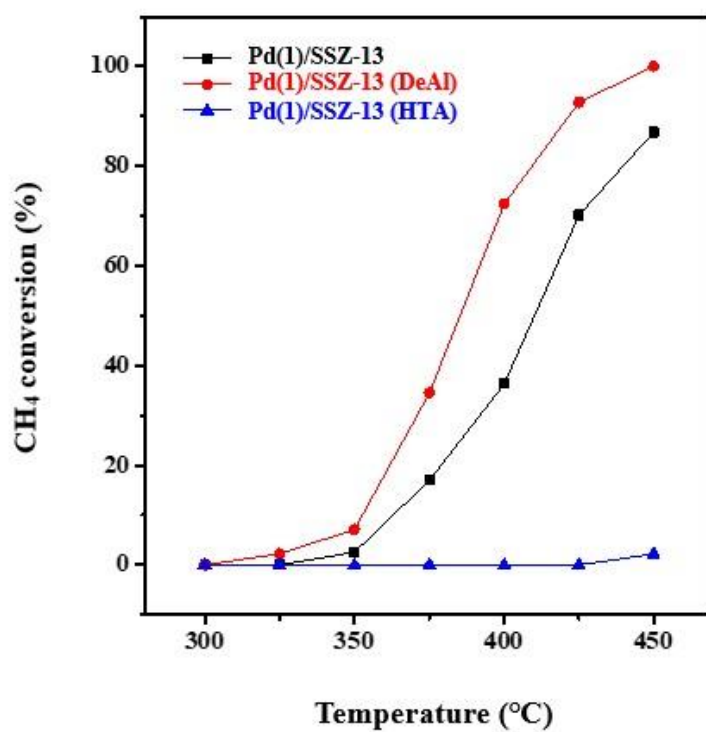


Fig. 3-1. Light-off curves of methane oxidation over the Pd/SSZ-13 catalysts.

Table 3-1. T_{50} values of the Pd/SSZ-13 catalysts.

Catalyst	T_{50} (°C)
Pd(1)/SSZ-13	409
Pd(1)/SSZ-13 (DeAl)	386
Pd(1)/SSZ-13 (HTA)	

3.3.2. Catalyst characterization

First, dealumination of the zeolite support after the hydrothermal treatment was verified by solid state NMR analysis. The Al species in zeolite can be analyzed from ^{27}Al NMR spectra (Fig. 3-2(a)). The main peak around 59 ppm can be assigned to tetrahedrally coordinated Al (framework Al) and another peak at 0 ppm is attributed to octahedrally coordinated Al (extra-framework Al). After the hydrothermal treatment, the tetrahedrally coordinated Al peak decreased sharply, indicating that the framework Al species were eliminated during the aging. In addition, slight increase in the extra-framework Al peak was observed after the hydrothermal treatment, which implies the generation of defective framework after the dealumination process. The Si species in the zeolite catalysts were examined by ^{29}Si NMR analysis (Fig. 3-2(b)). The main peak around 111 ppm is attributed to $\text{Q}^4 \text{Si}(\text{O}-\text{Si})_4$, and another peak at 105 ppm belongs to $\text{Q}^3 \text{Si}(\text{O}-\text{Si})_3(\text{O}-\text{Al})$ [13]. After the hydrothermal treatment, the increase of the Q^4 peak intensity and the decrease of the Q^3 peak intensity were observed, which implies the decrease of Al species in the zeolite framework. In addition, Si/Al_2 ratio was calculated from the peak area since it represents the number of aluminum atoms next to the silicon atom. The Si/Al_2 ratio increased from 23 to 64, which further supports that the zeolite was successfully dealuminated as expected.

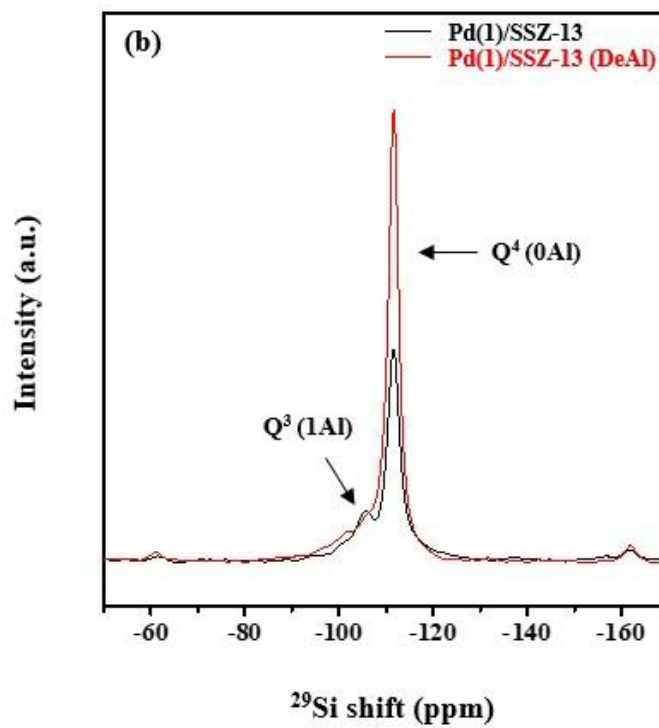
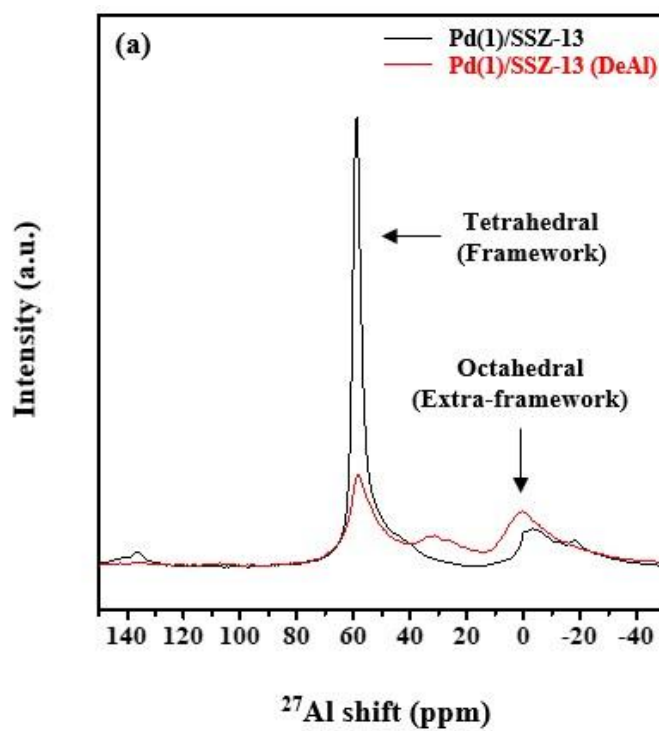


Fig. 3-2. (a) ^{27}Al NMR and (b) ^{29}Si NMR spectra of the Pd/SSZ-13 catalysts.

Second, the effect of the hydrothermal treatment on the zeolite textural property was examined by N_2 adsorption-desorption and XRD analyses. Sharp slope was observed from the N_2 adsorption-desorption isotherms at the low pressure range, which suggests the presence of micropores (Fig. 3-3). In addition, the hysteresis loop indicates the existence of mesopores, which arises from the stacking of the zeolite particles. Nevertheless, there was no noticeable difference in the N_2 adsorption-desorption isotherms between the catalysts. The BET surface area (532 vs 543 cm^2/g) and micropore volume (0.24 vs 0.25 cm^3/g) were also similar, which indicates that the zeolite microporous structure was not destroyed by the dealumination process (Table 3-2). Meanwhile, all catalysts exhibited the chabazite structure of the SSZ-13 support from the XRD patterns, demonstrating the stable zeolite structure (Fig. 3-4). Relative crystallinity was calculated from the peak intensity, which was 96% for the Pd(1)/SSZ-13 (DeAl). Based on the characterization results, it can be concluded that the zeolite structure was maintained, although the aluminum species were selectively eliminated during the hydrothermal treatment.

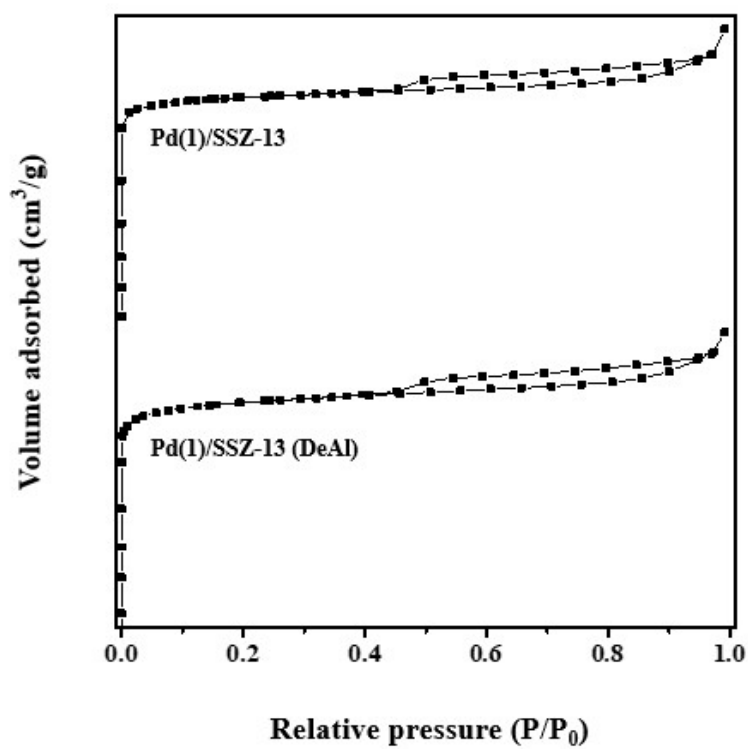


Fig. 3-3. N₂ adsorption-desorption isotherms of the Pd/SSZ-13 catalysts.

Table 3-2. Textural properties of the Pd/SSZ-13 catalysts.

Catalyst	BET surface area (cm ² /g)	Micropore volume (cm ³ /g)
Pd(1)/SSZ-13	543	0.25
Pd(1)/SSZ-13 (DeAl)	532	0.24

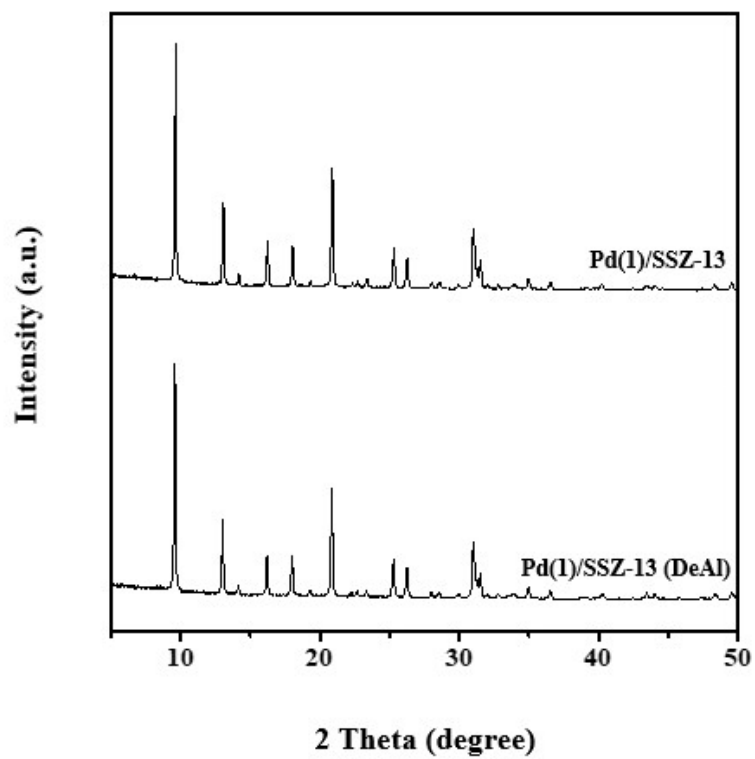


Fig. 3-4. XRD patterns of the Pd/SSZ-13 catalysts.

It is well-known that the hydrophobicity of the zeolite can be enhanced by the dealumination process. Thus, the hydrophobicity change after the hydrothermal treatment was explored by TGA, H₂O adsorption and H₂O-DRIFTS analyses. Since the catalysts were calcined at 500 °C before the TGA analysis, the weight loss observed during the experiment can be considered as the desorption of adsorbed H₂O on the zeolite support (Fig. 3-5). The relatively small weight loss observed from the Pd(1)/SSZ-13 (DeAl) catalyst indicates that it is more hydrophobic than the pristine catalyst. In addition, the larger amount of adsorbed H₂O observed from the H₂O adsorption isotherms further supports that the zeolite became more hydrophobic after the dealumination (Fig. 3-6). The hydrophobicity change was further confirmed from the DRIFTS spectra, which were collected after H₂O adsorption and subsequent N₂ purging process (Fig. 3-7). The broad band from 2800 to 3500 cm⁻¹ can be ascribed to the OH stretching vibration of adsorbed water. The OH band was hardly observed from the Pd(1)/SSZ-13 (DeAl), which implies that it became more hydrophobic after the dealumination, consistent with the previous characterization results. The increase of hydrophobicity can be explained by the characteristics of Al-O-Si and Si-O-Si bonds in the zeolite. The Al-O-Si bond is more polar than the Si-O-Si bond because the Al-O is combination of covalent and ionic bonds, while the Si-O is completely covalent bond. Thus, the decrease of Al-O-Si bond after the hydrothermal treatment explains the increase of hydrophobicity.

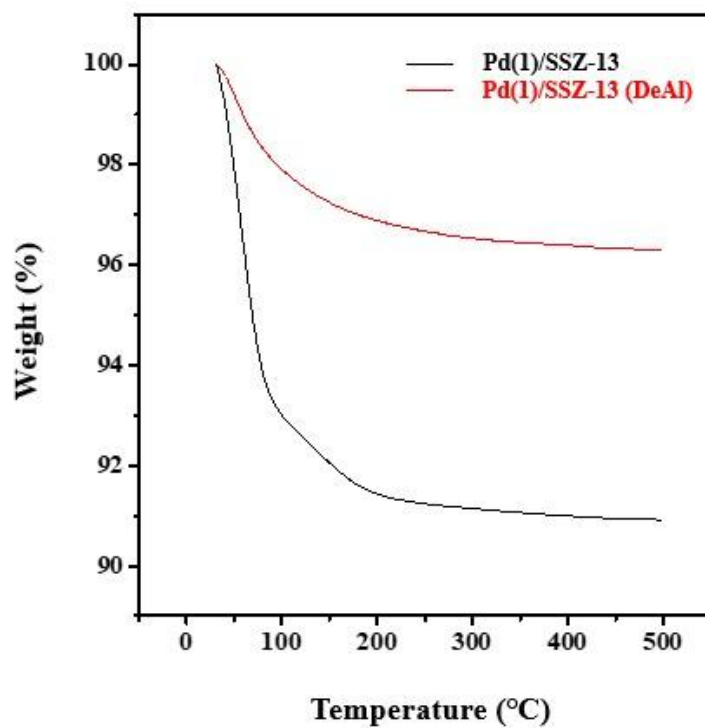


Fig. 3-5. TGA profiles of the Pd/SSZ-13 catalysts.

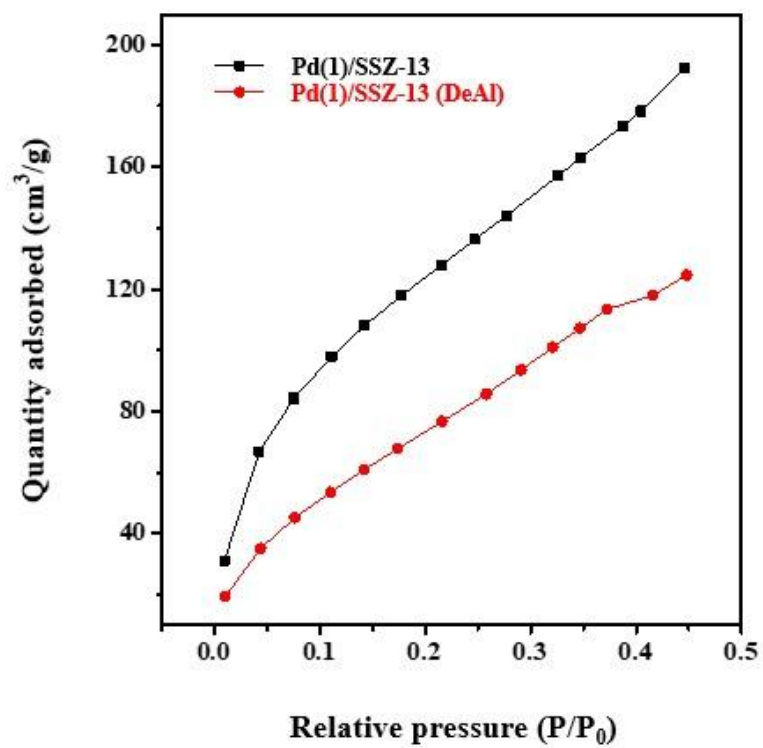


Fig. 3-6. H₂O adsorption isotherms of the Pd/SSZ-13 catalysts.

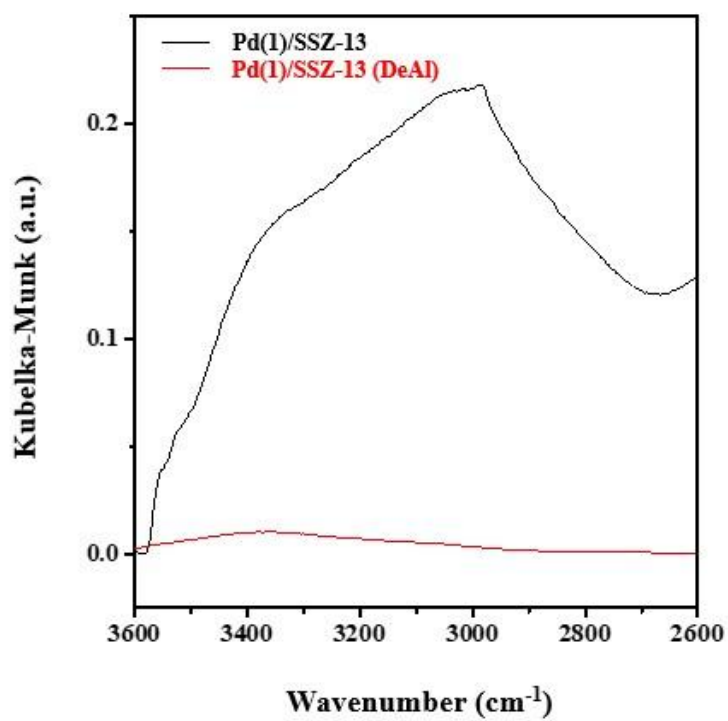


Fig. 3-7. DRIFT spectra of the Pd/SSZ-13 catalysts obtained after H₂O adsorption.

Next, the effect of the dealumination on the property of the active site, the state of Pd was investigated by Raman, DRIFTS and H₂-TPR analyses. It is well-known that Pd species in the zeolite catalyst can exist as PdO nanoparticles or monoatomic Pd ions. The formation of bulk PdO particles was explored by the Raman analysis (Fig. 3-8). The peak from 450 to 500 cm⁻¹ belongs to the T-O-T vibration in the chabazite zeolite structure and another peak at 650 cm⁻¹ can be assigned to the bulk PdO. From the intensity of the PdO peak, it can be inferred that the bulk PdO formation was accelerated in the Pd(1)/SSZ-13 (DeAl), while the Pd(1)/SSZ-13 (HTA) catalyst possessed the least amount of PdO. Pd ion species in the zeolite catalysts were confirmed by the CO-DRIFTS experiment (Fig. 3-9). Various peaks were observed from 2100 to 2200 cm⁻¹, which can be assigned to CO adsorbed on the Pd ions (Pd²⁺ or Pd(OH)⁺). CO adsorption peak was hardly observed from the Pd(1)/SSZ-13 (DeAl), which indicates the absence of Pd ions in the catalyst. On the other hand, the peak intensity of the Pd(1)/SSZ-13 (HTA) was higher than that of the pristine catalyst, which implies that the formation of Pd ions was promoted by the hydrothermal treatment. H₂-TPR analysis was conducted to further confirm the previous results because PdO nanoparticles and Pd ions can be distinguished from the reduction temperature (Fig. 3-10). The sharp peak in the range of 0-50 °C belongs to the reduction of PdO. The formation of PdH_x after the reduction of PdO to Pd metal was confirmed from the negative peak near 100 °C, which arises from the decomposition of PdH_x. The TPR profiles of the pristine and Pd(1)/SSZ-13 (DeAl) catalysts were similar, although the peak intensity of PdO reduction was slightly higher for the latter one. On the other hand, the TPR profile of the Pd(1)/SSZ-13 (HTA) was completely different from those of other catalysts. The PdO peak intensity was much lower than the other catalysts and new broad peak appeared in the range of 100-200 °C, which can be ascribed to the reduction

of Pd ions . Since the peak area represents the amount of H₂ consumption, the PdO/Pd_{total} ratio could be calculated from the H₂-TPR results (Table 3-3). The concentration of PdO was in the order of Pd(1)/SSZ-13 (DeAl) > Pd(1)/SSZ-13 > Pd(1)/SSZ-13 (HTA). Based on the previous characterization results, it can be concluded that most of the Pd species existed as PdO in the pristine and Pd(1)/SSZ-13 (DeAl) catalysts, while Pd ions were the major species for the Pd(1)/SSZ-13 (HTA). The larger amount of PdO in the Pd(1)/SSZ-13 (DeAl) than that in the pristine catalyst can be explained by the NH₃-TPD results (Fig. 3-11). The low temperature peak around 150 °C can be assigned to weakly bound NH₃ species and the high temperature peak above 300 °C belongs to the Brønsted acid sites (framework Al sites) . The number of acid sites decreased significantly after the hydrothermal treatment because large proportion of framework Al species were eliminated during the aging. Thus, it is reasonable to assume that the formation of Pd ions will be suppressed when Pd is impregnated on the dealuminated zeolite because Brønsted acid sites are required for the stabilization of Pd ions . In contrast to the other catalysts, most of the Pd species existed as Pd ions in the Pd(1)/SSZ-13 (HTA) catalyst. It is reported that the mobility of Pd species increases during the hydrothermal treatment (high temperature and humid condition) . Thus, the increase of Pd ions can be explained by the re-dispersion of PdO nanoparticles to the isolated Pd ions during the aging process.

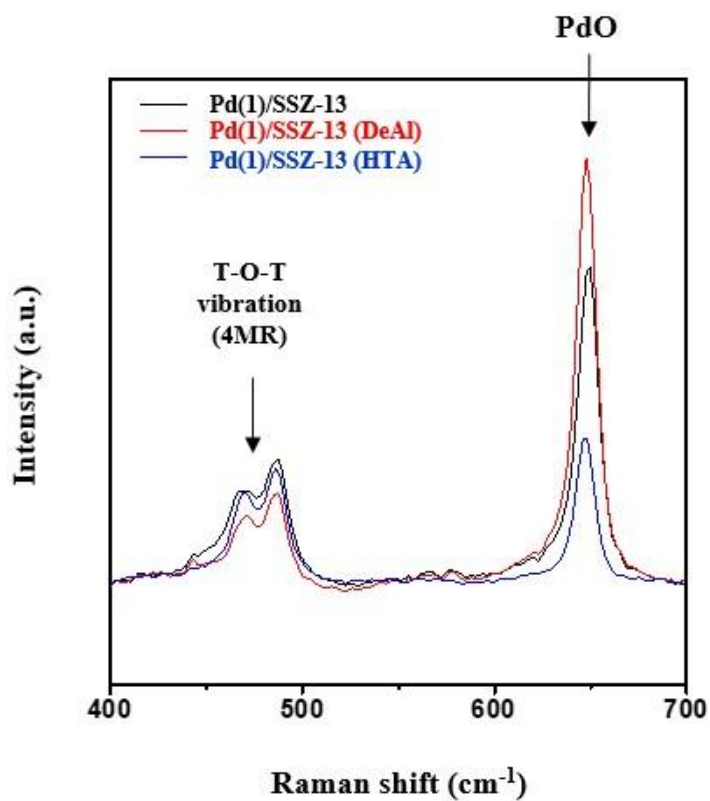


Fig. 3-8. Raman spectra of the Pd/SSZ-13 catalysts.

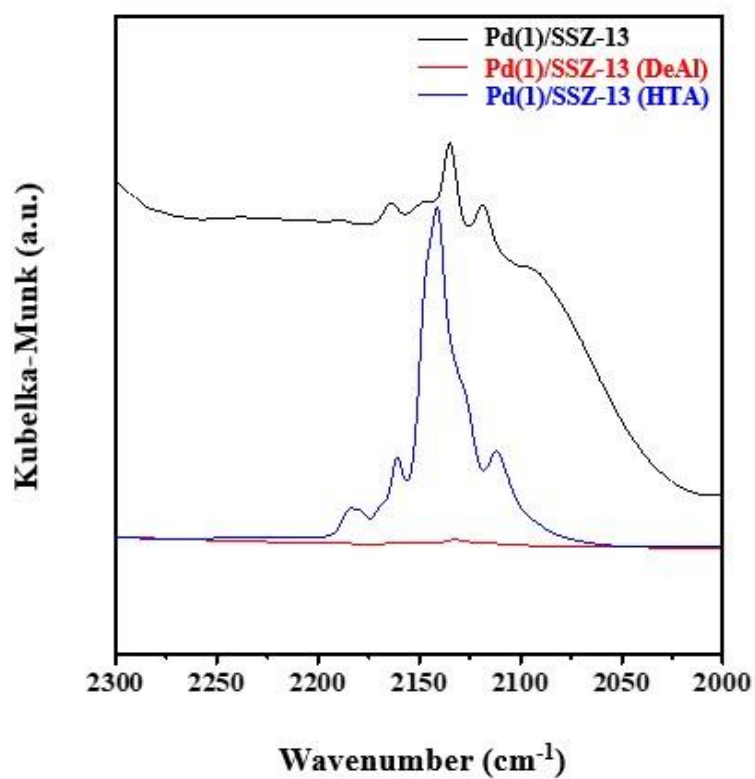


Fig. 3-9. DRIFT spectra of the Pd/SSZ-13 catalysts obtained after CO adsorption.

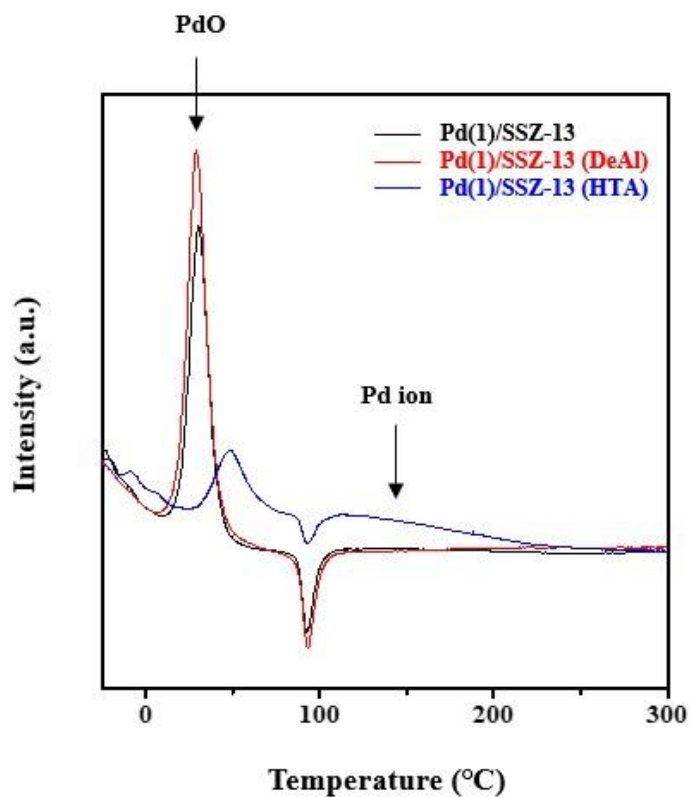


Fig. 3-10. H₂-TPR profiles of the Pd/SSZ-13 catalysts.

Table 3-3. PdO/Pd_{total} ratio of the Pd/SSZ-13 catalysts.

Catalyst	PdO/Pd _{total} (%)
Pd(1)/SSZ-13	78
Pd(1)/SSZ-13 (DeAl)	99
Pd(1)/SSZ-13 (HTA)	24

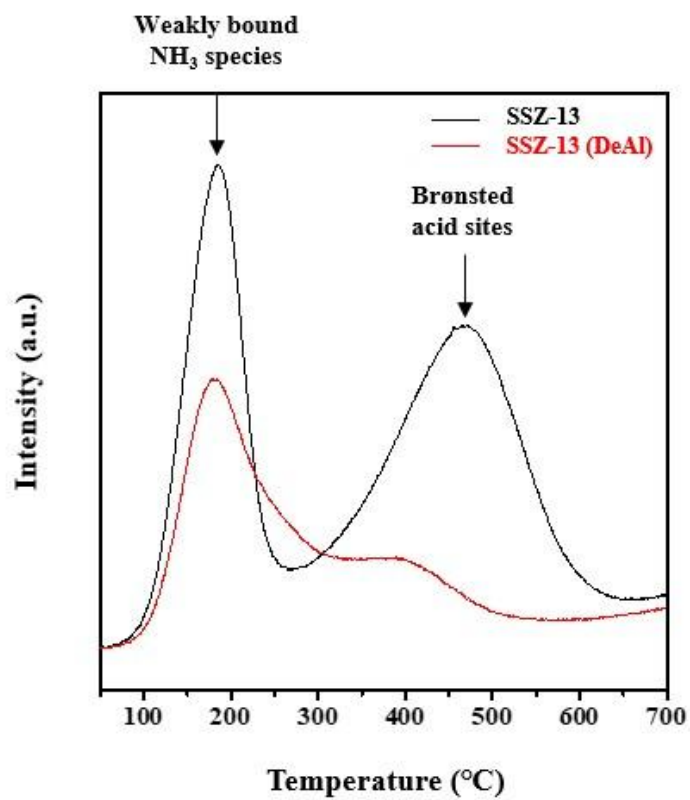


Fig. 3-11. NH₃-TPD profiles of the SSZ-13 supports.

Due to the unique microporous structure of the SSZ-13, the PdO nanoparticles can exist at different location; external zeolite surface and internal zeolite pores. Therefore, the location of PdO in the Pd(1)/SSZ-13 and Pd(1)/SSZ-13 (DeAl) catalysts was investigated by STEM and XPS analyses. HAADF-STEM and EDX mapping images displayed the location of PdO particles (Fig. 3-12). Compared to the Pd(1)/SSZ-13 catalyst, the images of the Pd(1)/SSZ-13 (DeAl) clearly displayed that the surface of the dealuminated SSZ-13 support was covered with the large amount of PdO nanoparticles. Thus, it is reasonable to assume that the concentration of external PdO nanoparticles would be larger in the Pd(1)/SSZ-13 (DeAl). The location of PdO particles was further supported by the XPS analysis (Fig. 3-13). The Pd 3d spectra displayed a peak around 336.7 eV, which can be assigned to the either PdO or Pd ions because both oxidation states are Pd²⁺. The peak position was similar, but the peak intensity was much higher for the Pd(1)/SSZ-13 (DeAl). In addition, the surface atomic concentration was calculated from the XPS results (Table 3-4). Although the bulk Pd concentration obtained from the ICP-AES analysis was similar, the XPS results demonstrated that the surface Pd concentration was different. The surface Pd concentration of the Pd(1)/SSZ-13 (DeAl) was 0.95%, which was much higher than that of the pristine catalyst (0.48%). Thus, it can be assumed that most of the Pd species in the Pd(1)/SSZ-13 (DeAl) were exposed at the external zeolite surface. The difference in the location of PdO species can be explained by the hydrophobicity of the zeolite support because it would be more difficult for the Pd precursor solution to penetrate into the internal pores of the hydrophobic zeolite. Based on the previous characterization results, it can be concluded that the Pd(1)/SSZ-13 possessed both external and internal PdO nanoparticles, while most of the Pd species in the Pd(1)/SSZ-13 (DeAl) were exposed at the external zeolite surface.

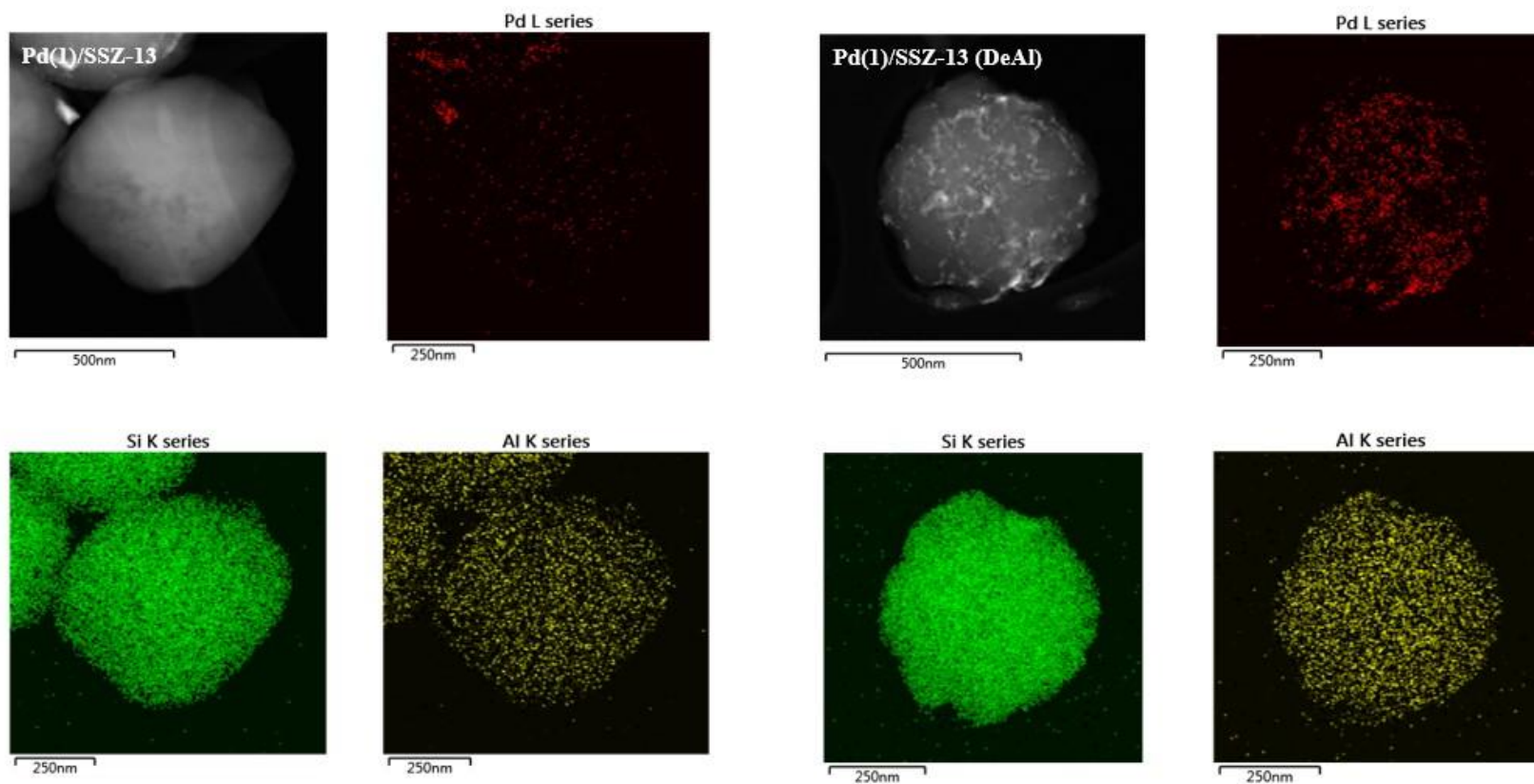


Fig. 3-12. HAADF-STEM and EDX mapping images of the Pd/SSZ-13 catalysts.

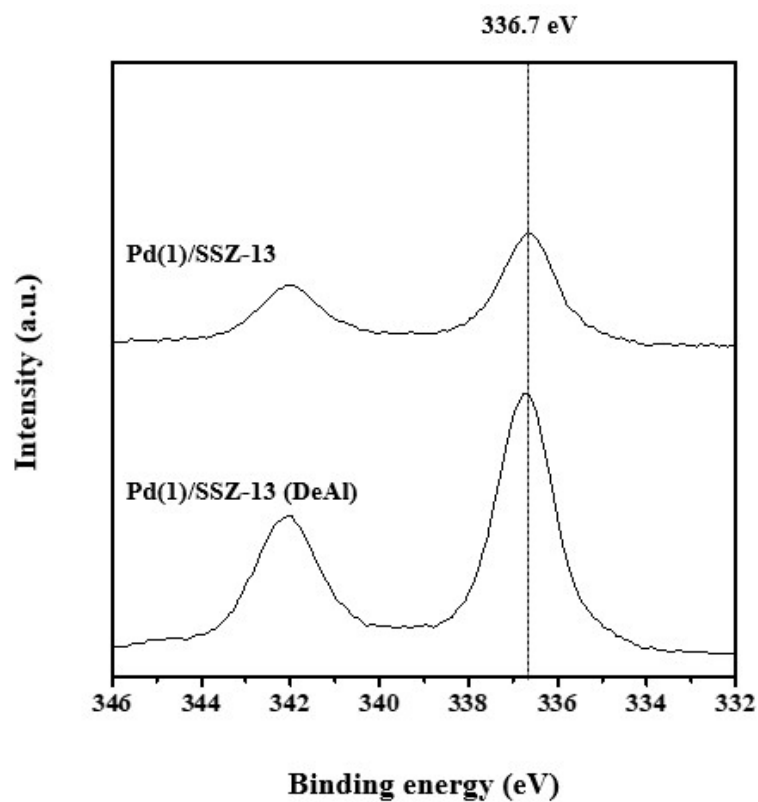


Fig. 3-13. Pd 3d XPS spectra of the Pd/SSZ-13 catalysts.

Table 3-4. Surface and bulk Pd concentration of the Pd/SSZ-13 catalysts.

Catalyst	Surface atomic concentration	Bulk concentration
	Pd (%)	Pd (wt.%)
Pd(1)/SSZ-13	0.48	0.87
Pd(1)/SSZ-13 (DeAl)	0.95	0.94

3.4. Discussion

The Pd(1)/SSZ-13 (DeAl) catalyst exhibited superior catalytic activity in methane oxidation compared to the other Pd/SSZ-13 catalysts, which was prepared by the dealumination of the SSZ-13 support. However, various catalytic properties were affected by the dealumination, including hydrophobicity of zeolite, state and location of Pd species. Thus, in order to elucidate whether the enhancement of activity was induced by the change of zeolite hydrophobicity, the catalytic activities of the zeolite catalysts were also evaluated in dry condition, where feed gas did not contain H₂O (Fig. 3-14). Interestingly, the catalytic activity of the Pd(1)/SSZ-13 (DeAl) was superior than that of the pristine catalyst even in the dry condition. The T₅₀ values of both catalysts increased after the introduction of water, which indicates the decrease of initial activity (Table 3-5). In addition, activation energies were calculated from the Arrhenius plot (Fig. 3-15). The activation energies for the dry condition were in the range of 107-116 kJ/mol, while significant increase was observed when water was added (178-194 kJ/mol). The increase of activation energy in the presence of water in the feed indicates that the catalytic activity of the Pd(1)/SSZ-13 (DeAl) was still inhibited by H₂O even though the zeolite surface became more hydrophobic after the dealumination. Therefore, it was reasonable to conclude that the hydrophobicity of zeolite was not a key factor for determining the methane oxidation activity.

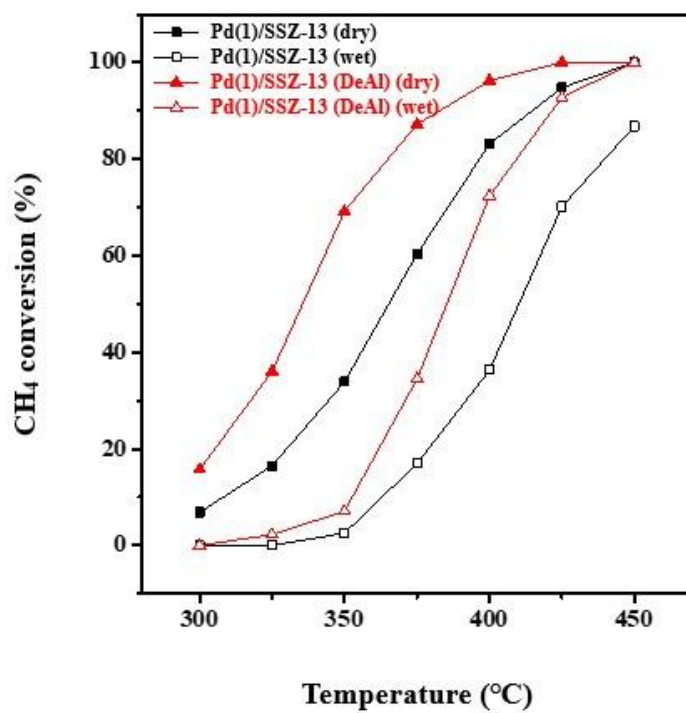


Fig. 3-14. Light-off curves of methane combustion over the Pd/SSZ-13 catalysts; dry and wet condition.

Table 3-5. T_{50} values of the Pd/SSZ-13 catalysts; dry and wet condition.

Catalyst	Dry condition T_{50} (°C)	Wet condition T_{50} (°C)
Pd(1)/SSZ-13	365	409
Pd(1)/SSZ-13 (DeAl)	337	385

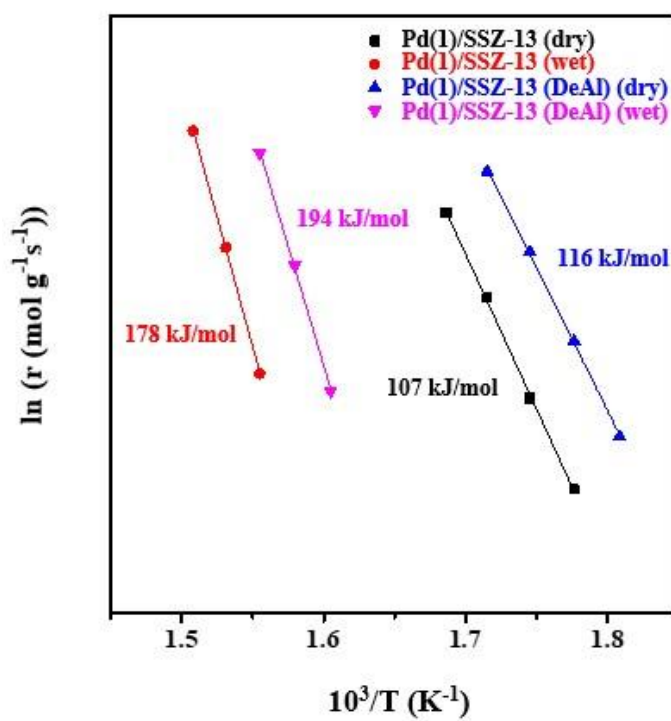


Fig. 3-15. Arrhenius plots of the methane combustion over the Pd/SSZ-13 catalysts.

Meanwhile, it was confirmed from the Raman, CO-DRIFT and H₂-TPR analyses that the state of Pd was altered after the hydrothermal treatment. For instance, Pd species mainly existed as Pd ions in the Pd(1)/SSZ-13 (HTA) catalyst, which exhibited extremely low methane oxidation activity compared to the other catalysts. Thus, it is reasonable to assume that the isolated Pd ions were not very active for the methane oxidation reaction compared to the PdO nanoparticles, which is consistent with previous reports. It is reported that Pd-O pairs are active sites for C-H bond activation, which is rate determining step for the methane oxidation reaction. Therefore, it can be concluded that the Pd paired with extra-lattice oxygen (PdO nanoparticle) is more active for the C-H bond cleavage compared to the Pd paired with the lattice oxygen of zeolite (Pd ion).

On the other hand, previous characterization results demonstrated that most Pd species existed as PdO in the Pd(1)/SSZ-13 and Pd(1)/SSZ-13 (DeAl) catalysts, although the location of PdO was different. The PdO species in the Pd(1)/SSZ-13 (DeAl) were exposed at the zeolite surface, while portion of PdO species in the Pd(1)/SSZ-13 were encapsulated inside the zeolite pores. The previous catalytic activity test demonstrated that the methane oxidation activity of the Pd(1)/SSZ-13 (DeAl) was superior to that of the Pd(1)/SSZ-13. Thus, it is reasonable to assume that the external PdO nanoparticles were more active than the encapsulated PdO. Considering that the SSZ-13 is small pore zeolite, it can be inferred that the size of the PdO inside the micropores would be very small compared to the PdO at the surface. Recently, various groups reported that highly dispersed Pd species are not active for the methane oxidation reaction. Goodman et al. claimed that single atom catalysts are not active for the reaction because critical ensemble size is required for the adsorption of oxygen and dehydrogenation of methane. In addition, Murata et al. reported that the size of Pd particle and

methane oxidation activity displayed volcano-shaped curve and 5-10 nm Pd particles exhibited highest activity . Moreover, the accessibility of reactant to the active site can be another reason for the low activity. It is reasonable to assume that methane will more easily adsorb on the PdO nanoparticles exposed at the zeolite surface, while diffusion to the PdO confined in the zeolite pores will be more difficult .

In order to further prove that the property of Pd was more critical factor for the catalytic activity compared to the zeolite hydrophobicity, we converted the Pd ions in the Pd(1)/SSZ-13 (HTA) to the PdO nanoparticles by reduction at 400 °C and re-oxidation at 500 °C. Generally, Pd ions are highly dispersed in the zeolite pores and stabilized at the Brønsted acid sites . Therefore, it can be assumed that the Pd ions inside the zeolite pores will be converted to the encapsulated PdO nanoparticles after the mild reduction and re-oxidation process because of the zeolite confinement effect . Thus, it is reasonable to assume that the hydrophobicity of the Pd(1)/SSZ-13 (HTA-400R500C) will be similar to the Pd(1)/SSZ-13 (DeAl), while the location of PdO will be completely different. Although the Pd(1)/SSZ-13 (HTA-400R500C) possessed hydrophobic surface, the catalytic activity was still inferior to the Pd(1)/SSZ-13 (DeAl), even lower than the pristine catalyst (Fig. 3-16). Such a low activity further proves that the hydrophobicity was not critical factor for the catalytic activity and the PdO nanoparticles confined inside the zeolite pores were not very active for the reaction.

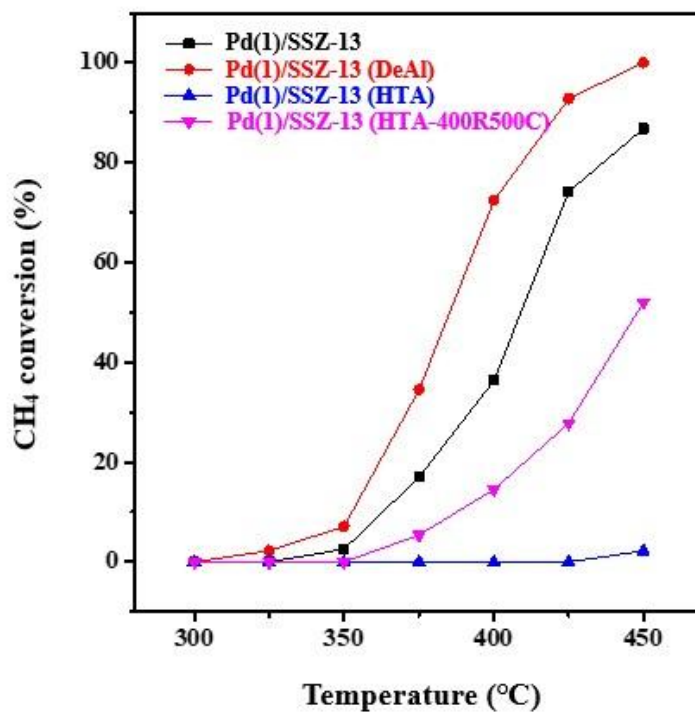


Fig. 3-16. Light-off curves of methane combustion over the Pd/SSZ-13 catalysts including Pd(1)/SSZ-13 (HTA-400R500C) catalyst.

The inhibition effect of H₂O on the initial methane oxidation activity was examined from the previous catalytic activity test and activation energy calculation, which demonstrated that the initial activity was still inhibited by H₂O even after the dealumination process. In addition, the deactivation effect of H₂O on the catalytic stability was investigated by the long-term activity test at 400 °C (Fig. 3-17). Deactivation was observed from both catalysts, but the deactivation rate of the Pd(1)/SSZ-13 (DeAl) was lower than that of the pristine catalyst. The deactivation in the presence of water is frequently observed from Pd/Al₂O₃ catalysts. However, recent studies demonstrated that the deactivation can be alleviated when Pd is impregnated on the zeolite with high Si/Al₂ ratio or pure silica zeolite (silicalite-1). Thus, it is reasonable to assume that the Al₂O₃ support or PdO-Al₂O₃ interface is responsible for the deactivation. Cui et al. reported that the PdO nanoparticles encapsulated in the zeolite pores are decorated with Al layer. However, the PdO nanoparticles in the Pd(1)/SSZ-13 (DeAl) will be less affected by the Al decoration because they are mostly exposed at the external surface and the Si/Al₂ ratio increased significantly after the dealumination process. Therefore, it can be concluded that the Pd(1)/SSZ-13 (DeAl) was less vulnerable to the deactivation because the PdO nanoparticles exposed at the surface were less decorated by Al.

In summary, various catalytic properties, including zeolite hydrophobicity, state and location of Pd species were affected by the dealumination process. Among them, it was revealed that the state and location of Pd species were critical factors for the methane oxidation activity. Pd(1)/SSZ-13 (DeAl) was the most active catalyst for the reaction because it possessed large amount of PdO nanoparticles exposed at the surface, which were more active than the encapsulated PdO and isolated Pd ions.

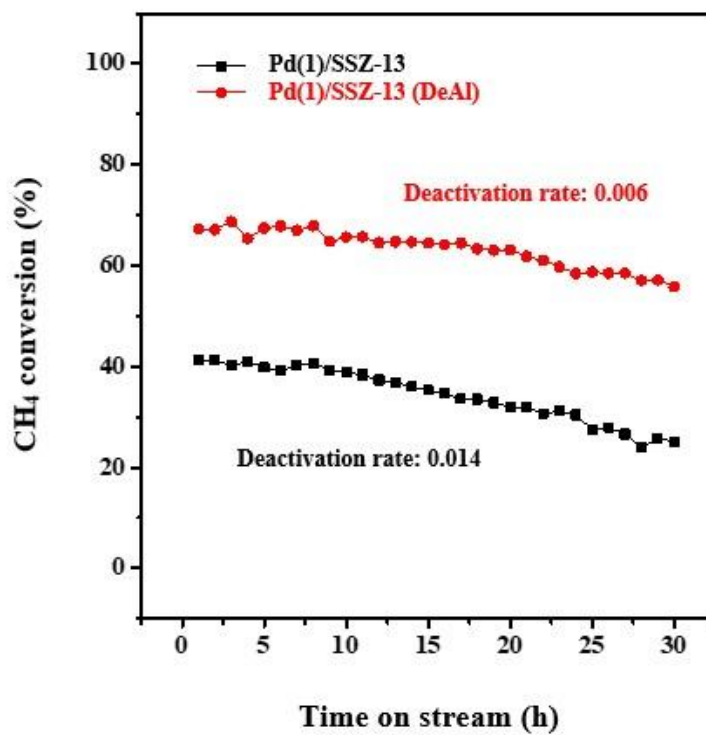


Fig. 3-17. Methane conversion with time-on-stream in the methane combustion reaction over the Pd/SSZ-13 catalysts at 400 °C.

Chapter 4. Effects of Pd precursors on the catalytic properties of Pd/CeO₂ catalysts for CH₄ and CO oxidation

4.1. Introduction

The number of transport vehicles has grown significantly over the past few decades owing to global economic growth. However, toxic gases, including nitrogen oxides, hydrocarbons, and carbon monoxide, are emitted from internal combustion engines, which can seriously impact the environment . Among the available technologies, catalytic oxidation is considered the most effective for reducing hydrocarbon and carbon monoxide emissions . Thus, developing highly active catalysts for CH₄ and CO oxidation reactions is essential to meet stringent regulations implemented to promote clean environments.

Noble metal catalysts, especially those containing Pd, have attracted significant attention due to the excellent catalytic activities for various oxidation reactions . Because of their high cost, noble metal catalysts are generally prepared by dispersing a small amount of the precious metal on a support material, such as alumina, ceria, or zeolite . Among them, ceria is generally utilized for oxidation reactions owing to the redox properties arising from the Ce⁴⁺/Ce³⁺ cycle, strong interaction with supported metals and large oxygen storage capacity .

Because of the limited availability of noble metals, the synthesis of highly

active catalysts with low metal loadings is essential for industrial applications. Pd species in Pd/CeO₂ catalysts can exist in various states, most commonly as metallic Pd, PdO nanoparticles, and highly dispersed Pd ions stabilized in ceria defect sites by forming a Pd_xCe_{1-x}O_{2-δ} solid solution. Each Pd phase exhibits different catalytic activities for different reactions. Therefore, understanding the active phase of Pd for a specific reaction is important to synthesize a highly active catalyst with an appropriate Pd state.

It is widely reported that the state of Pd in Pd/CeO₂ catalysts can be adjusted by various methods. First, the Pd state can be altered by the morphology of ceria support. Chen et al. and Hu et al. studied methane, propane and CO oxidation activities of Pd/CeO₂ catalysts prepared using ceria supports with octahedron, cube, and rod morphologies. The catalyst prepared using a ceria support with octahedral morphology was more active toward methane and propane oxidation compared to the rod morphology catalyst because PdO_x nanoparticles on the former cracked C-H bonds more efficiently than the highly dispersed Pd ions on the latter. On the other hand, the rod morphology catalyst was more active toward CO oxidation because the Pd ions in Pd_xCe_{1-x}O_{2-δ} solid solution easily created oxygen vacancy sites. In addition, the preparation method is another critical factor for altering the Pd phase in Pd/CeO₂. Ma et al. investigated CH₄ combustion over Pd/CeO₂ synthesized by different methods. The ratio of PdO particles to Pd_xCe_{1-x}O_{2-δ} was affected by the preparation method, and catalytic activity was correlated to the surface PdO concentration. Liu et al. also investigated the effects of Pd state on the propane oxidation activity of Pd/CeO₂ by modifying preparation method. They claimed that PdO was more favorable for propane activation and oxidative decomposition of reaction intermediates compared to the solid solution. Compared to the numerous studies on the ceria morphology and preparation method, the role of Pd precursors on the properties and activities of Pd/CeO₂ remains largely unexplored to the best of our knowledge. Danielis et al. explored

the effects of Pd salt in Pd/CeO₂ prepared by dry milling method, but their work was more focused on tuning the oxidation state of Pd by altering the calcination condition. Monteiro et al. investigated CO oxidation over Pd/Al₂O₃ and Pd/CeO₂/Al₂O₃ catalysts prepared by different precursors. They revealed that the Pd dispersion was affected by the precursor type, but the chemical state of Pd species was not discussed in detail. Herein, the Pd/CeO₂ catalysts prepared using different Pd precursors (palladium nitrate and acetate) were applied to the catalytic oxidation of CH₄ and CO. After combining results from various characterization techniques, it was revealed that the type of Pd precursor clearly affected the state and dispersion of Pd species, which were critical factors for the catalytic activity.

4.2. Experimental

4.2.1. Catalyst preparation

Commercial CeO₂ (Rhodia), palladium nitrate dihydrate (Sigma-Aldrich), and palladium acetate (Sigma-Aldrich) were utilized to prepare Pd/CeO₂ catalysts containing 2 wt% Pd (incipient impregnation method). After the impregnation, the catalysts were dried (80 °C for 16 h) and subsequently thermally treated under static air condition (500 °C for 2 h). The samples prepared using palladium nitrate and acetate are designated as Pd(2)/CeO₂ (N) and Pd(2)/CeO₂ (A), respectively.

4.2.1. Catalyst characterization

Microstructural characterization using high-angle annular dark-field scanning transmission electron microscopy (HAADF-STEM) and energy dispersive X-ray spectroscopy (EDX) was carried out on a JEM-ARM200F (JEOL)

with a spherical aberration corrector (200 kV). CO chemisorption was conducted on a BEL-CAT-II (BEL Japan) system. The samples were reduced under 5% H₂/Ar at 300 °C for 30 min before the analysis. After lowering the temperature to -78 °C, pulsed-CO chemisorption was performed. The dispersion of metallic Pd, D (%), was computed from the following equation.

$$D (\%) = \frac{V \times SF \times MW}{V_{mol} \times W} \times 100$$

V is the volume of adsorbed CO; SF is the stoichiometric factor (Pd/CO = 2); MW is the Pd molar mass; V_{mol} is the standard molar volume of CO, and W is the supported Pd weight. X-ray diffraction (XRD) analysis was carried out on a SmartLab (Rigaku) system (30 mA, 40 kV). Raman spectroscopy experiment was operated on a DXR2xi (Thermo Fischer Scientific) system with the samples excited at 532 nm. H₂-temperature programmed reduction (H₂-TPR) was operated on a BEL-CAT-II system. Before the analysis, the samples were pretreated with 50 mL/min Ar at 300 °C. After lowering the temperature to -80 °C, it was raised to 600 °C with 30 mL/min of 5% H₂ balanced with Ar (10 °C/min). X-ray photoelectron spectroscopy (XPS) was operated on a K-alpha spectrometer (Thermo Fischer Scientific). The C 1s reference peak (284.6 eV) was utilized to correct the binding energies. Bulk Pd loading was calculated via inductively coupled plasma atomic emission spectroscopy (ICP-AES) using an OPTIMA 8300 (Perkin-Elmer) apparatus. X-ray absorption spectroscopy (XAS) data were obtained from the 7D-XAFS beamline of the Pohang Light Source (PLS-II) at the Pohang Accelerator Laboratory. X-ray absorption near edge structure (XANES) and extended X-ray absorption fine structure (EXAFS) data were acquired from the raw data using the Athena program (Demeter) for data processing. Thermogravimetric analysis (TGA) of the uncalcined Pd(2)/CeO₂ (A) sample was conducted using a Discovery TGA (TA Instruments) apparatus. The temperature was heated to 500 °C under air or N₂ (5 °C/min).

4.2.1. Catalytic reaction system

CH₄ combustion was operated in a quartz reactor. The catalysts were mixed with SiO₂ beads to disperse heat generated from the reaction. The feed was consisted of 1,000 ppm CH₄ and 15% O₂ (N₂ balance) and flowed into the reactor (60,000 mL/g_{cat}·h). In addition, 5% H₂O was included to the feed for the investigation of H₂O effects. The outlet feed gas composition was analyzed via online gas chromatography (Younglin 6500) with a thermal conductivity detector (TCD) and flame ionization detector (FID). The CH₄ conversion was determined after 30 min stabilization in the range of 250 to 450 °C at 25 °C intervals.

Similar to the CH₄ combustion reaction, CO oxidation was also operated in a quartz reactor. The catalysts were reduced at 400 °C for 30 min before the reaction (10% H₂ balanced with N₂). The reactant feed was comprised of 1% CO and 10% O₂ (N₂ balance) and flowed into the reactor (400,000 mL/g_{cat}·h). After 1 h of stabilization at 40 °C, the temperature was increased by 2 °C/min from 40 to 160 °C. The outlet feed gas composition was examined using a Nicolet iS50 Fourier-transform infrared (FTIR) spectrometer (Thermo Fischer Scientific). The turnover frequency (TOF) was determined from the equation.

$$\text{TOF (s}^{-1}\text{)} = \frac{c \cdot X}{N \cdot D} \text{ (s}^{-1}\text{)}$$

c is the moles of methane or CO in the reactant; X is the methane or CO conversion; N is the total amount of Pd (mole), and D is the Pd dispersion.

4.3. Results

4.3.1. Catalytic performance

The Pd/CeO₂ catalysts prepared using different Pd precursors were

applied to the CH₄ and CO oxidation reactions. The light-off curves for methane combustion are displayed in Fig. 4-1. T₅₀ values, the temperatures required for achieving 50% of CH₄ conversion are in Table 3-1. Both Fig. 4-1(a) and Table 4-1 illustrate that the activity of the Pd(2)/CeO₂ (N) was superior to that of Pd(2)/CeO₂ (A). Specifically, the T₅₀ of the Pd(2)/CeO₂ (N) was 318 °C, 75 °C lower than that of its counterpart. In addition, it should be considered that the exhaust of natural gas engines usually contains high water vapor concentrations. It is well-known that the CH₄ oxidation activity is hindered by H₂O owing to the accumulation of hydroxyl species, thereby reducing the number of active sites and hindering oxygen exchange between the Pd and support. Therefore, the methane combustion reaction was also evaluated using a reactant containing 5% H₂O (Fig. 4-1(b)). Compared to the dry conditions, the catalytic activities of both catalysts decreased after H₂O addition, and the T₅₀ increased by 50–60 °C. Nevertheless, the activity of the Pd(2)/CeO₂ (N) remained superior to that of its counterpart under both conditions.

CO oxidation was also carried out with the Pd/CeO₂, as displayed in Fig. 4-2. Reduction process was conducted at 400 °C before the reaction because it has been reported that Pd metal is more active toward CO oxidation than PdO. Contrary to the CH₄ oxidation results, the activity of Pd(2)/CeO₂ (A) was superior to that of Pd(2)/CeO₂ (N). Specifically, the T₅₀ of the Pd(2)/CeO₂ (A) was 107 °C, 22 °C lower than that of its counterpart. The effect of H₂O on the catalyzed CO oxidation is displayed in Fig. 4-2(b). Significantly, the catalytic performance was enhanced after H₂O addition. Wang et al. described that the reaction of CO with hydroxyl can yield a carboxyl intermediate, decreasing the activation energy barrier by activating molecular O₂. However, the Pd(2)/CeO₂ (A) exhibited superior activity under both conditions. Therefore, it can be summarized that Pd/CeO₂ catalytic activity was altered by the type of Pd precursor used, with opposite trends in catalytic activity for the reactions studied herein. The Pd precursor effects on the catalytic activity and properties was studied using subsequent characterization

techniques.

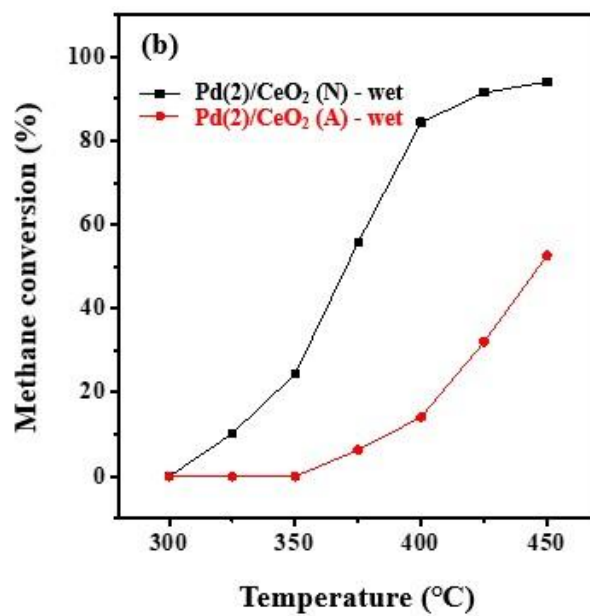
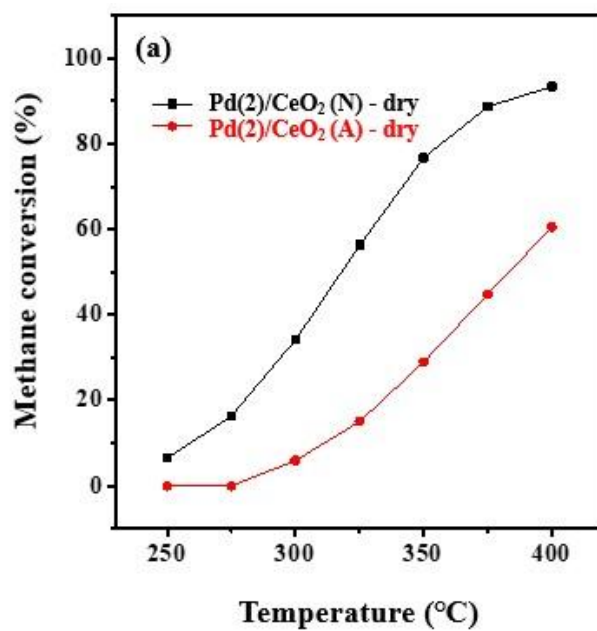
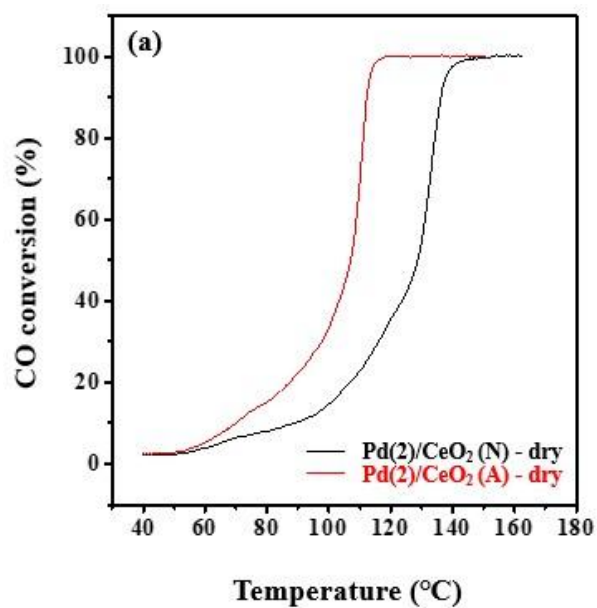


Fig. 4-1. Light-off curves of CH₄ oxidation over the Pd(2)/CeO₂ catalysts; (a) dry condition and (b) wet condition (5% H₂O).



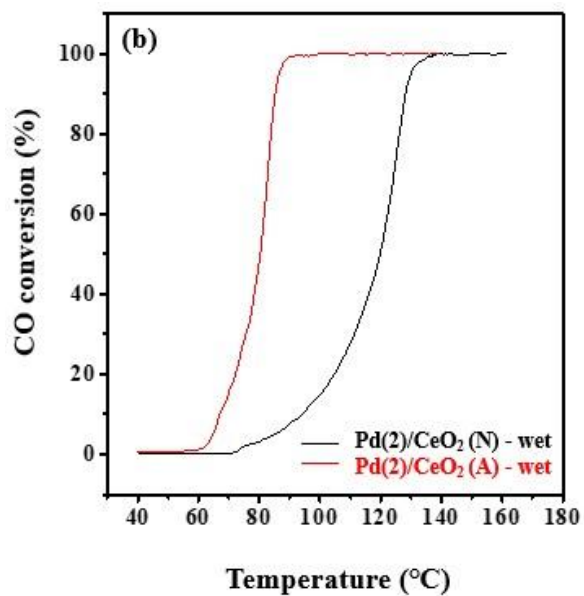


Fig. 4-2. Light-off curves of CO oxidation over the Pd(2)/CeO₂ catalysts; (a) dry condition and (b) wet condition (5% H₂O).

Table 4-1. T₅₀ values of the Pd(2)/CeO₂ catalysts for oxidation reactions.

Catalyst	CH ₄ oxidation T ₅₀ (°C)	CO oxidation T ₅₀ (°C)
Pd(2)/CeO ₂ (N) - dry	318	129
Pd(2)/CeO ₂ (A) - dry	383	107
Pd(2)/CeO ₂ (N) – wet	370	120
Pd(2)/CeO ₂ (A) – wet	446	80

4.3.2. Catalyst characterization

The metal size distribution in the catalysts is generally analyzed using TEM images. However, it was hard to differentiate the Pd and ceria supports from the TEM images because the atomic numbers (Z-contrast) are similar. Therefore, the elemental distribution in the Pd/CeO₂ catalysts was analyzed via STEM-EDX mapping (Fig. 4-3). The Pd species agglomerated in an oval shape in the Pd(2)/CeO₂ (N), indicating that the PdO nanoparticles were present on the ceria surface. In contrast, the Pd signal was very weak in the Pd(2)/CeO₂ (A) catalyst, which indicates the highly dispersed Pd species throughout the ceria. In summary, EDX mapping clearly demonstrated that the size distribution of Pd metal is affected by the Pd precursor type.

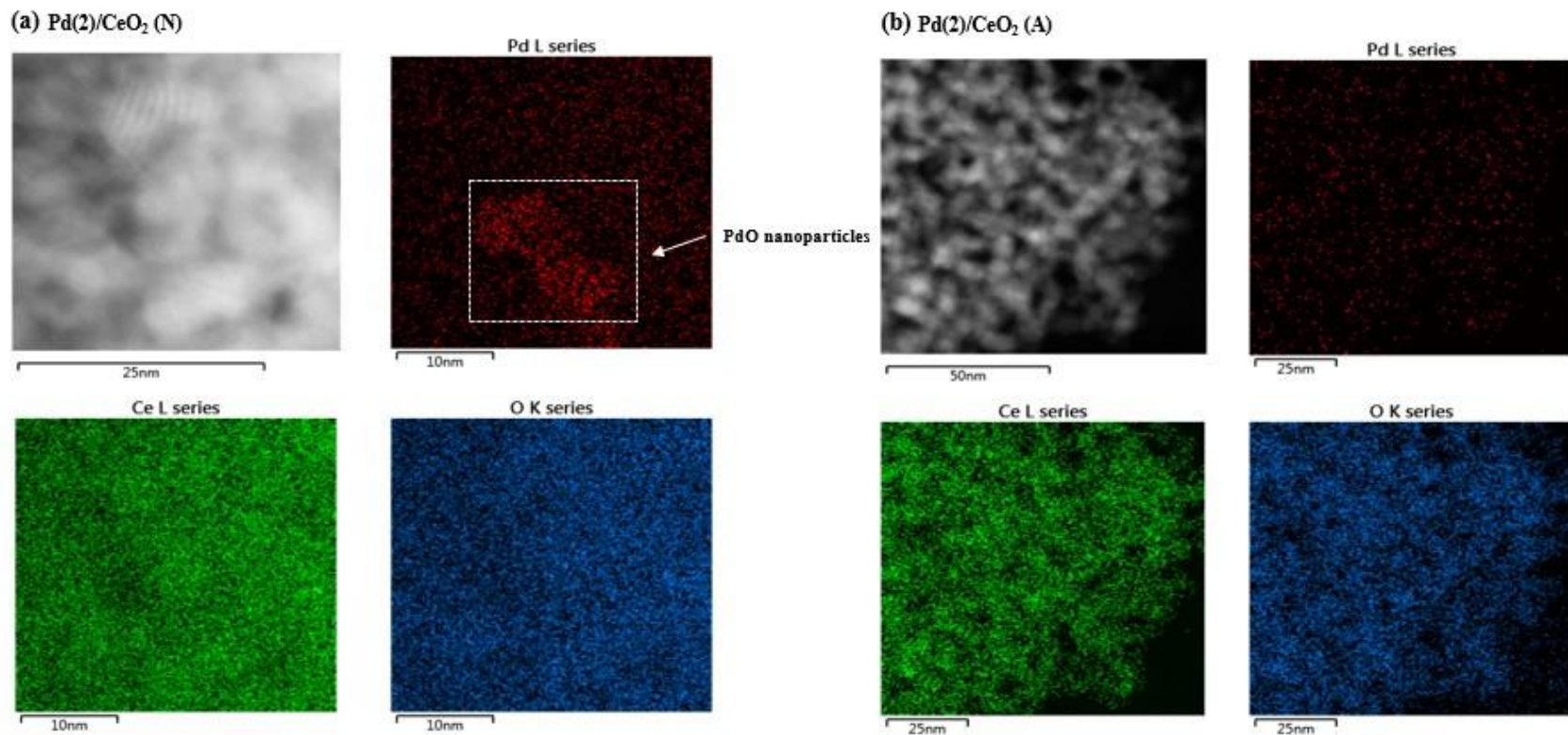


Fig. 4-3. HAADF-STEM images and EDX mapping of the (a) Pd(2)/CeO₂ (N) and (b) Pd(2)/CeO₂ (A) catalysts.

To further clarify the STEM-EDX mapping results, Pd metal dispersion was examined after the CO chemisorption experiment. For accurate measurements, CO should only be adsorbed on metallic Pd, but the literature suggests that CO can also adsorb on the CeO₂ support at room temperature. Therefore, CO chemisorption was performed at -78 °C because CO cannot chemisorb on CeO₂ at such low temperatures. The Pd metal dispersion of the Pd(2)/CeO₂ (N) and Pd(2)/CeO₂ (A) were 18.8 and 52.6%, respectively (Table 4-2). Assuming that the metals on the surface are spherical, the average metal size was determined using the following equation.

$$d_{Pd} \text{ (nm)} = \frac{112.1}{D \text{ (\%)}}$$

D (%) is the dispersion of metal [21]. The average sizes of the metallic Pd in the Pd(2)/CeO₂ (N) and Pd(2)/CeO₂ (A) were 2.1 and 5.9 nm, respectively. Therefore, both STEM and CO chemisorption results confirmed the higher Pd dispersion in the Pd(2)/CeO₂ (A), while large PdO particles were produced at the Pd(2)/CeO₂ (N) surface.

Table 4-2. Dispersion and average size of Pd in the Pd(2)/CeO₂ catalysts.

Catalyst	Pd dispersion (%)	Average Pd size (nm)
Pd(2)/CeO ₂ (N)	18.8	5.9
Pd(2)/CeO ₂ (A)	52.6	2.1

The XRD patterns of the samples exhibited a typical cubic fluorite phase of CeO_2 (Fig. 4-4) . As the catalysts were calcined under static air, it was expected that peaks corresponding to PdO would be observed for both catalysts. However, it is challenging to detect the characteristic diffraction peaks of PdO because the characteristic PdO peak (33.8°) overlaps with a large peak arising from the ceria support (33.2°) .

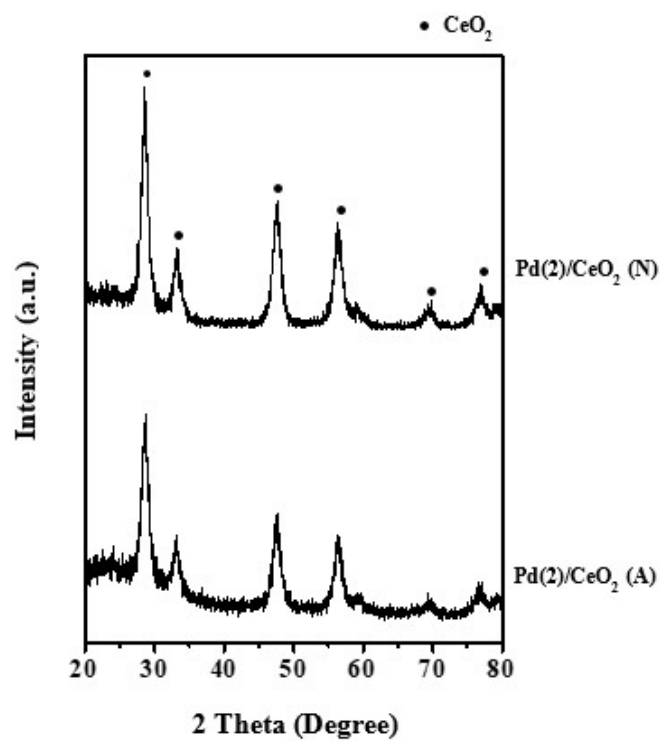


Fig. 4-4. XRD patterns of the Pd(2)/CeO₂ catalysts.

Because it was difficult to detect the PdO peak from the XRD analysis, the crystallinity of the PdO phase was analyzed using Raman spectroscopy. Fig. 4-5 displays that the peaks at 247 and 461 cm^{-1} arise from the CeO_2 support, which are the second-order transverse acoustic (2TA) and fluorite F_{2g} mode, respectively. A new peak is found at 642 cm^{-1} only for the Pd(2)/ CeO_2 (N), which arises from the Pd-O bond stretching in the PdO_4 structure often found at the core of crystalline nanoparticles. Therefore, it was confirmed that the Pd(2)/ CeO_2 (N) contained a large amount of crystalline PdO nanoparticles, which agrees well with the EDX mapping and CO chemisorption results.

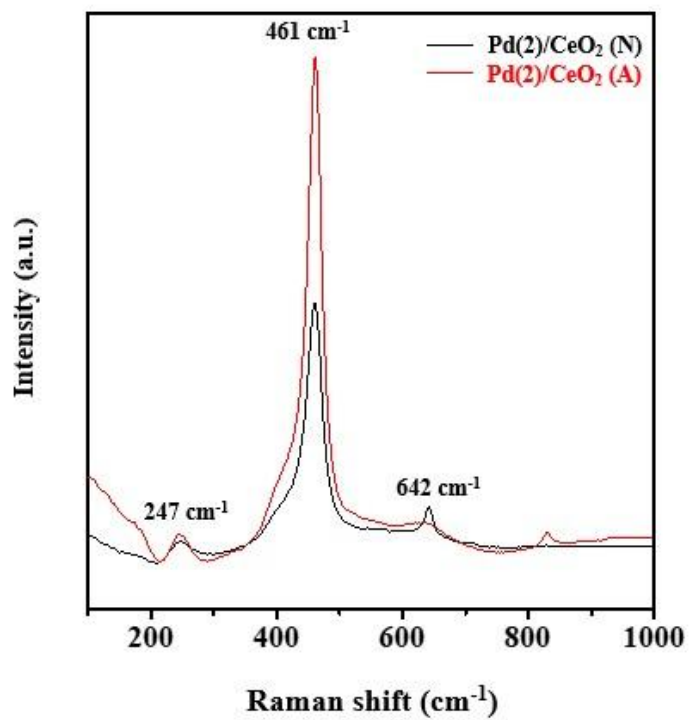


Fig. 4-5. Raman spectra of the Pd(2)/CeO₂ catalysts.

H₂-TPR experiments were conducted to investigate catalyst reducibility. Fig. 4-6 shows two reduction peaks for both catalysts, where the low-temperature peak at <100 °C is referred to PdO reduction and another peak at 400 °C to the surface CeO₂ reduction. The PdO reduction temperature was 54 °C for the Pd(2)/CeO₂ (N), which was 45 °C lower than that for its counterpart. Stronger metal-support interactions generally increase the reduction temperature of the metal oxide. Hence, it can be inferred that the metal-support interaction was stronger in the Pd(2)/CeO₂ (A). Furthermore, the sharp reduction peak of the Pd(2)/CeO₂ (N) indicates a rapid reduction process, further confirming that the metal-support interaction was weaker than in its counterpart. Meanwhile, the H₂ consumptions of the Pd(2)/CeO₂ (N) and Pd(2)/CeO₂ (A) samples were 0.41 and 0.49 mmol/g, respectively, both larger than the value required for the PdO reduction (0.19 mmol/g). This additional hydrogen consumption can be ascribed to the surface CeO₂ reduction near the Pd species, which was likely facilitated by hydrogen spillover from palladium to the ceria.

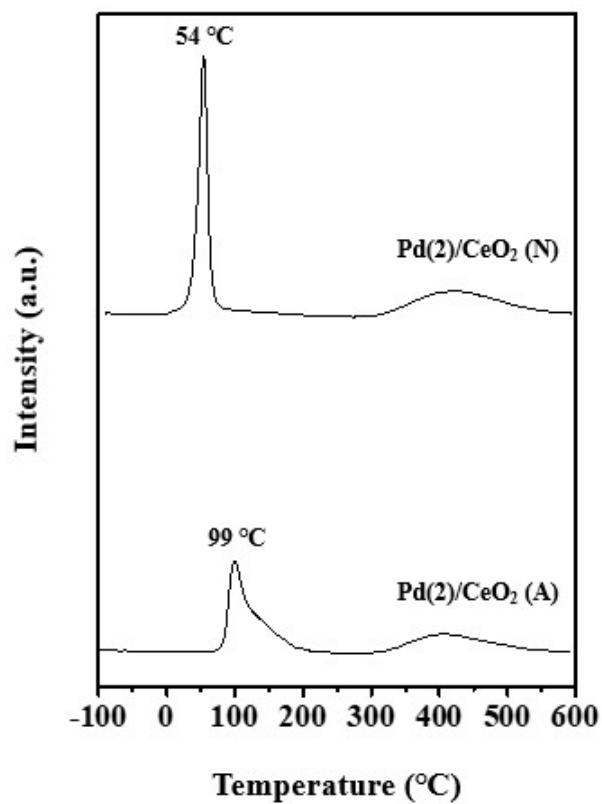


Fig. 4-6. H₂-TPR profiles of the Pd(2)/CeO₂ catalysts.

The Pd state on the catalyst surface was examined by XPS analysis. Pd 3d spectra presents two peaks at 336.5 eV, arising from Pd²⁺ in PdO nanoparticles, and 337.7 eV, from Pdⁿ⁺ ($2 \leq n \leq 4$) in the Pd_xCe_{1-x}O_{2-δ} solid solution (Fig. 4-7) . The peak corresponding to Pd metal (335 eV) was not observed because the catalysts were thermally treated under normal atmospheric conditions. The quantitative data calculated from the XPS spectra confirm that the Pd state is altered by the precursor type (Table 4-3). Clearly, the PdO nanoparticles were major species in the Pd(2)/CeO₂ (N), while the Pd species of the Pd(2)/CeO₂ (A) were inserted into the defect sites of the CeO₂ support and induced the formation of Pd_xCe_{1-x}O_{2-δ}. In addition, the peak intensity was higher for the Pd(2)/CeO₂ (N) catalyst. Since XPS analysis is surface-sensitive, it can be interpreted that the PdO particles were exposed on the Pd(2)/CeO₂ (N) surface, while the Pd species of the Pd(2)/CeO₂ (A) sample were stabilized within the bulk ceria lattice.

The surface atomic concentrations computed from the XPS data are displayed in Table 4-4. Notably, the surface concentration of Pd was higher for the Pd(2)/CeO₂ (N) catalyst, even though both catalysts were prepared with the same Pd loading (2 wt%), as confirmed via ICP-AES. Hence, the difference between the surface and bulk Pd concentrations can be explained by the chemical state. As previously discussed, Pd species exist at the ceria surface as PdO_x nanoparticles in the Pd(2)/CeO₂ (N). In contrast, the Pd species are located in the bulk CeO₂ lattice as a Pd_xCe_{1-x}O_{2-δ} in the Pd(2)/CeO₂ (A) sample.

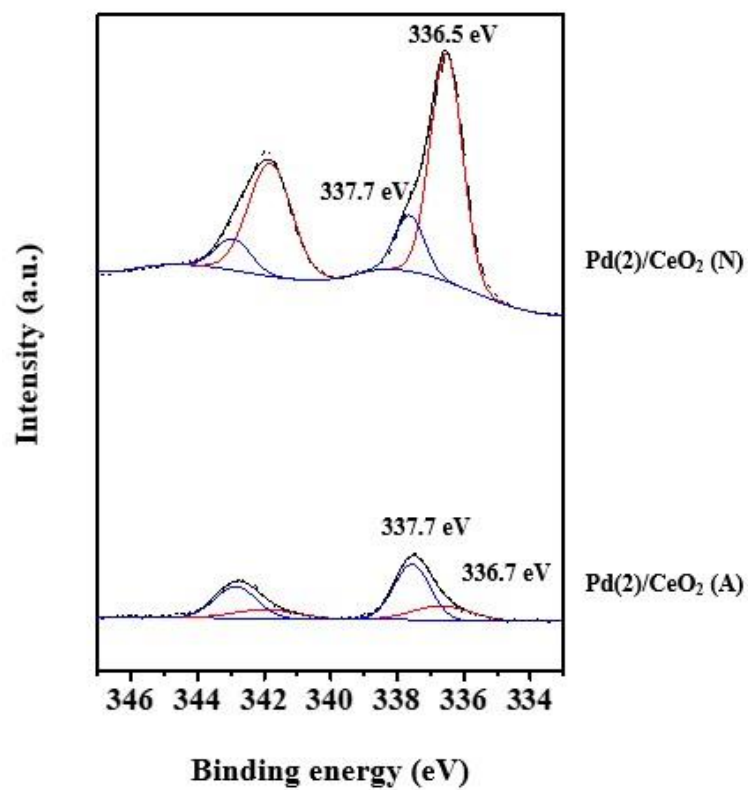


Fig. 4-7. Pd 3d XPS spectra of the Pd(2)/CeO₂ catalysts.

Table 4-3. Pd species on the surface of the Pd(2)/CeO₂ catalysts.

Catalyst	Pd	
	PdO (%)	Pd _x Ce _{1-x} O _{2-δ} (%)
Pd(2)/CeO ₂ (N)	81.7	18.3
Pd(2)/CeO ₂ (A)	29.8	70.2

Table 4-4. Surface and bulk Pd concentration of the Pd(2)/CeO₂ catalysts.

Catalyst	Surface atomic concentration			Bulk concentration
	Pd (%)	Ce (%)	O (%)	Pd (wt.%)
Pd(2)/CeO ₂ (N)	3.0	30.9	66.1	1.8
Pd(2)/CeO ₂ (A)	1.1	33.4	65.5	1.7

The Pd states were further examined by XAFS analysis. The XANES and EXAFS profiles are displayed in Fig. 4-8(a) and (b), respectively. The absorption edge profiles of both catalysts are close to that of the PdO reference (Fig. 4-8(a)). However, more detailed analyses of the XANES profiles highlight that the white line intensity of the Pd(2)/CeO₂ (A) was slightly higher than that of the PdO reference. The increment of the white line intensity is caused by the increased Pd oxidation state. This can be ascribed to the Pdⁿ⁺ species in the Pd(2)/CeO₂ (A), which is previously confirmed from the XPS analysis.

The EXAFS profiles displays a peak at 1.5 Å arising from the first Pd-O coordination shell was detected from both catalysts, confirming that Pd was oxidized (Fig. 4-8(b)). Another peak at 2.9 Å was assigned to second shell Pd-O-Pd coordination and the relative intensity of this peak was lower for the Pd(2)/CeO₂ (A) catalyst compared with its counterpart. These results indicate that the Pd size was smaller for the Pd(2)/CeO₂ (A) sample than for its counterpart, which is in agreement with the STEM-EDX mapping and CO chemisorption results.

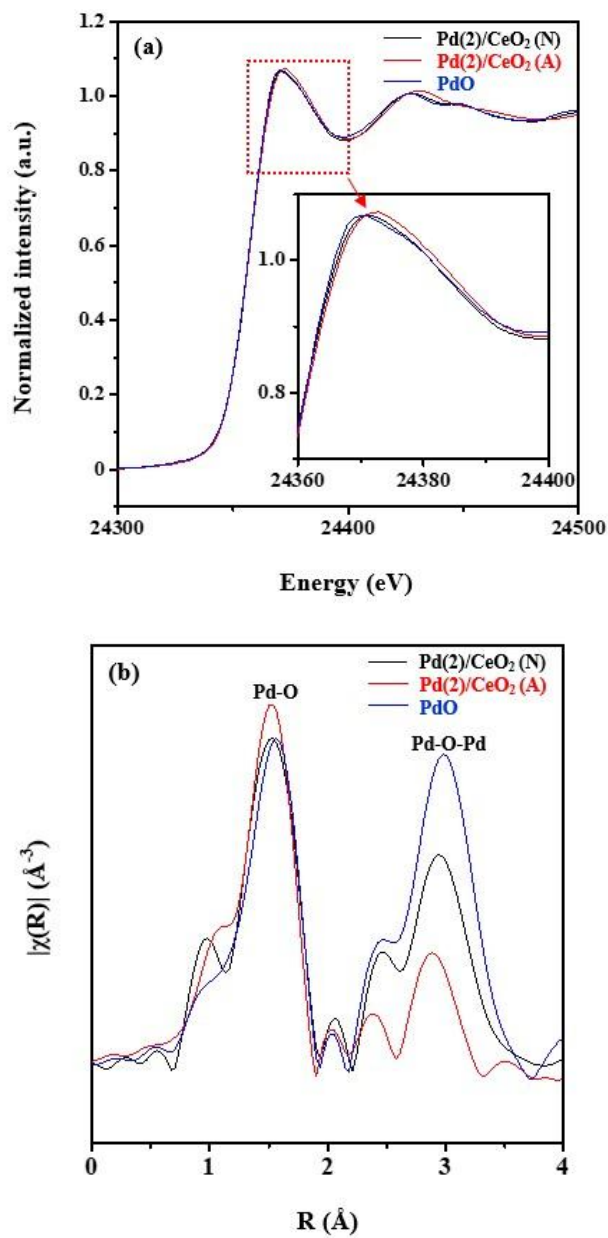


Fig. 4-8. (a) Normalized XANES and (b) EXAFS spectra of the Pd(2)/CeO₂ catalysts with PdO foil.

3.4. Discussion

Herein, Pd/CeO₂ catalysts were prepared using different Pd precursors and applied to CH₄ and CO oxidation reactions to examine their differing catalytic activities. The Pd(2)/CeO₂ (N) catalyst was highly active for CH₄ oxidation, whereas the Pd(2)/CeO₂ (A) catalyst exhibited high CO oxidation activity. Therefore, it can be interpreted that catalytic performance is largely affected by the type of Pd precursor. The effects of the Pd precursor on the catalytic properties and activities were studied using various characterization techniques.

Fig. 4-9 shows images of the Pd(2)/CeO₂ samples, wherein it is clear that the color of the Pd(2)/CeO₂ (N) catalyst is brown, whereas the Pd(2)/CeO₂ (A) catalyst is dark yellow, closer to the ceria support color. From these results, it is plausible to assume that the Pd state differed between the two catalysts.

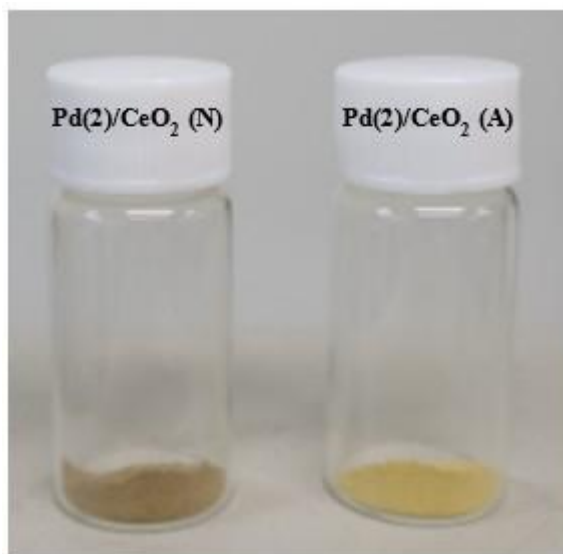


Fig. 4-9. The color of the Pd/CeO₂ catalysts.

Despite some discrepancies in literature regarding the identification of the active Pd states for methane oxidation, many authors have reported that PdO is the active state. Chen et al. claimed that PdO can dissociate methane and fully oxidize to CO₂, whereas the highly dispersed Pd ions are inactive in producing CO and tend to generate carbonate and formate species. In addition, they claimed that the incomplete coordination of Pd²⁺ and adjacent oxygen atoms were responsible for the high activity of PdO. Thus, the difference in the methane oxidation activity can be explained by the difference in the Pd state, which was discussed in the previous catalyst characterization section. The STEM-EDX mapping images revealed the presence of PdO nanoparticles on the Pd(2)/CeO₂ (N) surface, although it was difficult to observe them in the Pd(2)/CeO₂ (A). From the Raman and XPS spectra, it can be inferred that a Pd_xCe_{1-x}O_{2-δ} was produced, and Pd species were highly dispersed in the ceria support defect sites. Therefore, it can be hypothesized that the Pd state is critical for determining the methane oxidation catalytic activity. For Pd(2)/CeO₂ (A), Pdⁿ⁺ stabilized in the bulk ceria lattice could not easily facilitate methane oxidation. In contrast, the PdO nanoparticles exposed on the Pd(2)/CeO₂ (N) surface acted as active sites for methane oxidation.

The CH₄ oxidation over Pd/CeO₂ proceeds via Mars-van Krevelen mechanism. Accordingly, oxygen vacancies are produced when CH₄ reacts with PdO. The oxygen vacancies are replenished by lattice oxygen diffusion from the ceria and adsorption of gas-phase O₂. Therefore, methane oxidation activity can be affected by the oxygen vacancy replenishment rate. The Pd_xCe_{1-x}O_{2-δ} can act as a transition layer for oxygen species from the ceria to Pd. Therefore, the inferior activity of the Pd(2)/CeO₂ (A) sample than that of its counterpart can be explained

by excess $\text{Pd}_x\text{Ce}_{1-x}\text{O}_{2-\delta}$ because the transition channel thickness may limit the oxygen diffusion rate.

However, the trend of activity was opposite for the CO oxidation. The Pd(2)/CeO_2 (A) exhibited superior activity than the Pd/CeO_2 in previous studies prepared by similar method (Table 4-5) . In contrast to CH_4 oxidation, the Pd/CeO_2 samples were reduced prior to the reaction because metallic Pd has been reported to be the active site. Therefore, the difference in the CO oxidation activity between the catalysts cannot be explained using the Pd oxidation state. STEM-EDX, CO chemisorption, and EXAFS analyses revealed that the average Pd size was smaller in the Pd(2)/CeO_2 (A) sample compared to that of its counterpart. The Pd species were introduced into the bulk ceria lattice, forming strong Pd-O-Ce bonds in the acetate catalyst. Therefore, the metal-support interaction was stronger than that in the Pd(2)/CeO_2 (N) catalyst, as confirmed via the H_2 -TPR experiment. The strong metal-support interaction may explain the presence of highly dispersed Pd species because the Pd is stabilized by the support, and Pd agglomeration is prevented during reduction . Therefore, the high activity of the Pd(2)/CeO_2 (A) can be ascribed to high Pd dispersion that provided additional sites for CO adsorption.

Table 4-5. CO oxidation activities of the Pd/CeO₂ catalysts reported in the literatures.

Catalyst	Pd precursor	T₉₀ (°C)	Reactant	Space velocity (mL/g_{cat}·h)	Reference
Pd(2)/CeO₂ (A)	Acetate	112	CO 1%, O₂ 10%, N₂ balance	400,000	This work
Pd/CeO₂	Nitrate	130	CO 1%, O₂ 10%, He balance	120,000	[99]
Pd/CeO₂	Nitrate	148	CO 1%, O₂ 2.5%, N₂ balance	200,000	[100]
Pd/CeO₂	Chloride	205	CO 1%, O₂ 20%, N₂ balance	100,000	[101]

All catalysts (2 wt% Pd) in Table 3-5 were prepared using the conventional impregnation method.

Although the light-off curves showed that the Pd(2)/CeO₂ (A) catalyst exhibited superior activity than its counterpart, comparing catalytic activities in terms of TOF may be more appropriate because the number of active sites differs for catalysts with varying particle sizes. Fig. 4-10(a) shows the CO oxidation activity in terms of TOF values. The catalytic activity data in the kinetically controlled regime (under 20% CO conversion) was used to improve accuracy. The TOFs were similar in the kinetically controlled region (from 40 to 70 °C), although the Pd dispersion was different. In addition, the activation energy was obtained from the Arrhenius plot (Fig. 4-10(b)). The activation energies were within the range of the experimental error (44–48 kJ/mol). These results indicate that the catalytic active sites and reaction pathway are identical for both catalysts, irrespective of Pd dispersion. Therefore, the reaction is structure-insensitive reaction, as reported from previous research. From the kinetic study, it can be concluded that the catalytic activity normalized by the catalyst weight was higher for Pd(2)/CeO₂ (A) than that of its counterpart because of the larger number of active sites, whereas the activities normalized by the number of active sites were similar. Fig. 4-10(c) displays the Arrhenius plots of the catalysts for CH₄ oxidation. In contrast to CO oxidation, the activation energy of Pd(2)/CeO₂ (N) (73 kJ/mol) was significantly smaller than that of its counterpart. Because the active site for the methane oxidation reaction is known as PdO, the PdO nanoparticles on the Pd(2)/CeO₂ (N) surface were more active in cleaving the methane C-H bond than the Pd ions stabilized in the ceria lattice.

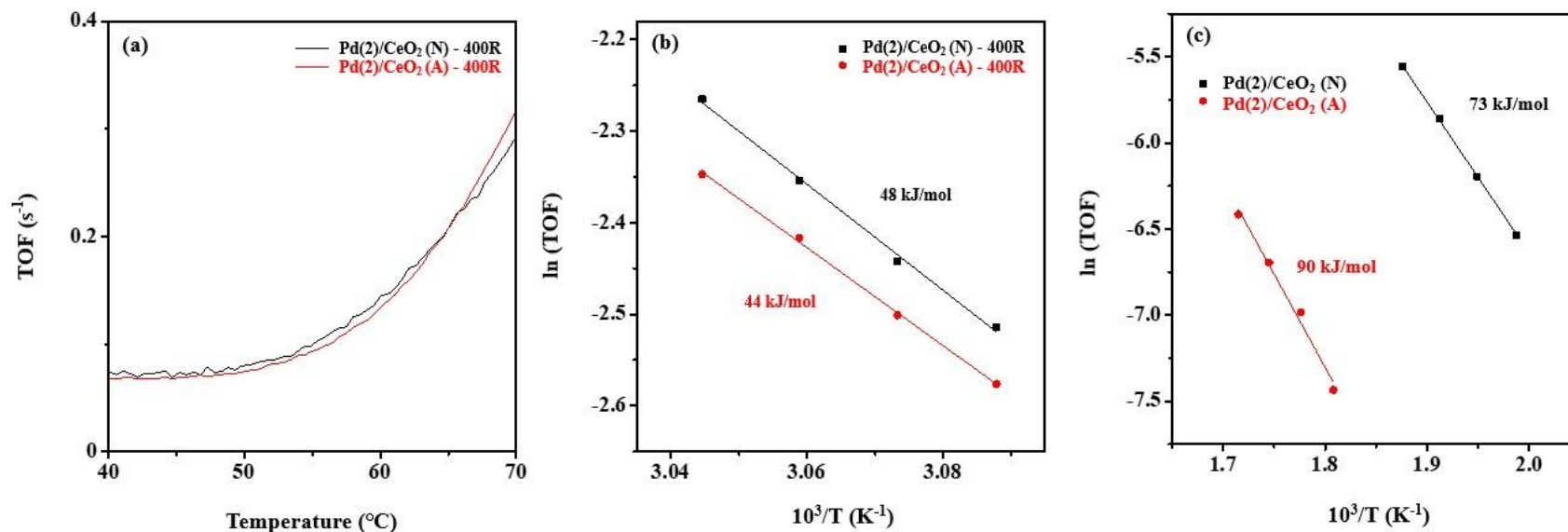


Fig. 4-10. (a) CO oxidation activities of the Pd(2)/CeO₂ catalysts in terms of TOF, Arrhenius plots (b) for CO and (c) CH₄ oxidation.

The major difference between Pd nitrate and acetate lies in their decomposition behavior. Pd nitrate directly decomposes to PdO, whereas Pd acetate initially decomposes to Pd metal and slowly oxidizes to PdO under oxidative conditions. To investigate the decomposition behavior of Pd acetate impregnated on the ceria support, H₂-TPR and TGA analyses were conducted on the Pd(2)/CeO₂ (A) catalysts. Fig. 4-11(a) displays the H₂-TPR results of Pd(2)/CeO₂ (A) calcined under different conditions. As discussed previously, a reduction peak at 99 °C was detected from the Pd(2)/CeO₂ (A) catalysts calcined in air, corresponding to Pd reduction. However, a reduction peak was not detected from -100 to 300 °C for the Pd(2)/CeO₂ (A) sample calcined under N₂, which implies the presence of metallic Pd on the catalyst. Therefore, the decomposition behavior of Pd acetate remained unchanged even after impregnation. Fig. 4-11(b) shows the TGA profiles of the Pd(2)/CeO₂ (A) catalyst under air and N₂ conditions. Notably, similar TGA profiles were obtained under both conditions, implying that the Pd species were inserted into the ceria lattice to form a Pd_xCe_{1-x}O_{2-δ}. This is because if Pd metal was oxidized to PdO, weight increases would be observed during the TGA process. Therefore, it can be concluded that Pd nitrate is more effective for synthesizing catalysts with PdO nanoparticles exposed on the ceria support surface. In contrast, Pd acetate impregnated on ceria decomposed into Pd metal, and subsequent calcination induced the incorporation of Pd species into the defect sites of ceria to form a Pd-O-Ce structure. It was induced by the interaction between the highly dispersed metallic Pd and ceria, which was higher than the interaction between the agglomerated PdO nanoparticles and ceria. In conclusion, the Pd(2)/CeO₂ (N) catalyst was highly active for CH₄ combustion because the PdO nanoparticles exposed at the surface acted as active sites. In contrast, the Pd(2)/CeO₂ (A) catalyst was more active for the CO oxidation reaction because the highly dispersed Pd provided additional sites for CO adsorption.

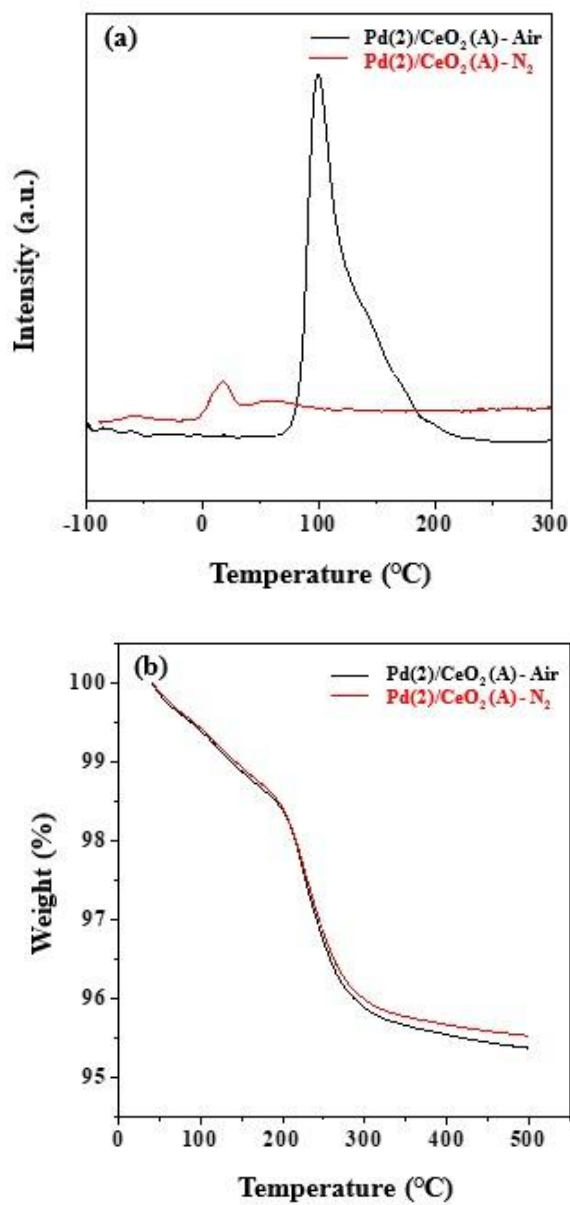


Fig. 4-11. (a) H₂ -TPR profiles and (b) TGA profiles of the Pd(2)/CeO₂ (A) catalysts calcined in air or N₂ condition.

Chapter 5. Conclusions

In chapter 2, mesoporous cobalt oxide catalysts were prepared using an SBA-15 template, and the catalysts were treated with nitric acid to modify the surface chemistry and structure. The prepared catalysts were applied to the methane combustion reaction, and significant enhancements in the catalytic activities of the acid-treated catalysts were observed compared to that of the fresh catalyst. The effects of acid treatment were investigated using various characterization methods. First, TEM and SEM observation revealed the morphological changes, such as surface roughening, as a result of the acid treatment. In addition, XRD and Raman analyses demonstrated that acid treatment resulted in lattice distortion and residual stress in the crystal structure. Thus, on the basis of these results, it was reasonable to hypothesize that defect sites, such as oxygen vacancy sites, are generated by the acid treatment. Furthermore, H₂-TPR, O₂-TPD, and XPS analyses showed that the acid-treated catalysts possessed larger amounts of Co²⁺ and surface chemisorbed oxygen species, which adds weight to the hypothesis concerning oxygen vacancy formation. In conclusion, in-depth characterization of the surface chemistry and defect structure of mesoporous cobalt oxide catalysts reveals that modification by acid treatment is beneficial for enhancing the catalyst activity for the catalytic oxidation of methane.

In chapter 3, the dealumination of the Pd/SSZ-13 catalysts were conducted by the hydrothermal treatment in order to study the effects of dealumination on the catalytic properties and activities. The Pd(1)/SSZ-13 (HTA), which was prepared by hydrothermal treatment of the pristine catalyst, displayed extremely low methane oxidation activity compared to the other catalysts. On the other hand, the Pd(1)/SSZ-13 (DeAl), which was prepared by hydrothermal treatment of the SSZ-13 support and subsequent Pd impregnation, exhibited

enhanced catalytic activity compared to the pristine catalyst. From the TGA, H₂O adsorption, DRIFTS analyses, it was confirmed that the hydrophobicity of zeolite was enhanced after the dealumination process. However, the increase of T₅₀ and activation energy in the presence of H₂O indicated that the Pd(1)/SSZ-13 (DeAl) catalyst was still inhibited by H₂O and the hydrophobicity change was not key factor for the activity enhancement. Next, the state of Pd was investigated by the Raman, DRIFTS and H₂-TPR analyses. Pd species mainly existed as PdO in the pristine and Pd(1)/SSZ-13 (DeAl) catalysts, while Pd(1)/SSZ-13 (HTA) possessed large amount of Pd ions. Thus, the inferior activity of the Pd(1)/SSZ-13 (HTA) can be explained by the Pd state because Pd ions are not active in the C-H bond activation compared to PdO. Although the pristine and Pd(1)/SSZ-13 (DeAl) catalysts both possessed large amount of PdO, the location of PdO was different. Most of the PdO in the Pd(1)/SSZ-13 (DeAl) was exposed at the external zeolite surface, while the Pd(1)/SSZ-13 possessed both external and internal PdO encapsulated in the zeolite pores. Therefore, the activity enhancement observed from the Pd(1)/SSZ-13 (DeAl) can be explained by the larger amount of external PdO nanoparticles, which were more active than encapsulated PdO. In addition, the Pd(1)/SSZ-13 (DeAl) was more resistant to the deactivation in the long-term activity test because the external PdO nanoparticles were less decorated by Al. In summary, the hydrothermal treatment is not always beneficial for the methane oxidation activity; Pd should be impregnated after hydrothermal treating the zeolite support in order to synthesize highly active and stable catalyst (Pd(1)/SSZ-13 (DeAl)) for the methane combustion.

In chapter 4, the effects of the Pd precursor on the activities and properties of Pd/CeO₂ catalysts were examined. Raman and XPS spectra disclosed that the Pd state was altered by the precursor type. The PdO nanoparticles exposed at the surface were active for CH₄ combustion, which were more abundant on the Pd(2)/CeO₂ (N) catalyst compared to that on its counterpart. However, most Pd

species in the Pd(2)/CeO₂ (A) existed as Pd ions stabilized in the ceria defect sites, which were not very active for the reaction. In addition, Pd dispersion was confirmed to be affected by the precursor type. The STEM-EDX mapping images, CO chemisorption, and EXAFS spectra revealed that the size of Pd was smaller in the Pd(2)/CeO₂ (A) catalyst than that in its counterpart. The stronger metal-support interaction arising from the Pd-O-Ce bond of the Pd_xCe_{1-x}O_{2-δ} structure was the underlying cause of the high dispersion. Because of its high Pd dispersion, a large amount of CO was adsorbed on the Pd(2)/CeO₂ (A) sample, which promoted the CO oxidation. In conclusion, the chemical state and dispersion status of Pd were largely affected by the Pd precursor and these proved to be critical for CH₄ and CO oxidation activities.

Bibliography

- [1] Y. Li, P. Wang, S. Wang, J. Liu, Y. Xie, W. Li, Quantitative investigation of the effects of CR, EGR and spark timing strategies on performance, combustion and NO_x emissions characteristics of a heavy-duty natural gas engine fueled with 99% methane content, *Fuel* 255 (2019) 115803.
- [2] A.W. Petrov, D. Ferri, F. Krumeich, M. Nachtegaal, J.A. van Bokhoven, O. Krocher, Stable complete methane oxidation over palladium based zeolite catalysts, *Nat. Commun.* 9 (2018) 2545.
- [3] D. Jiang, K. Khivantsev, Y. Wang, Low-temperature methane oxidation for efficient emission control in natural gas vehicles: Pd and beyond, *ACS Catal.* 10 (2020) 14304-14314.
- [4] C.K. Lambert, Current state of the art and future needs for automotive exhaust catalysis, *Nat. Catal.* 2 (2019) 554-557.
- [5] P. Lott, M. Eck, D.E. Doronkin, A. Zimina, S. Tischer, R. Popescu, S. Belin, V. Briois, M. Casapu, J.-D. Grunwaldt, O. Deutschmann, Understanding sulfur poisoning of bimetallic Pd-Pt methane oxidation catalysts and their regeneration, *Appl. Catal. B: Environ.* 278 (2020) 119244.
- [6] K. Murata, J. Ohyama, Y. Yamamoto, S. Arai, A. Satsuma, Methane combustion over Pd/Al₂O₃ catalysts in the presence of water: Effects of Pd particle size and alumina crystalline phase, *ACS Catal.* 10 (2020) 8149-8156.
- [7] Y. Lei, W. Li, Q. Liu, Q. Lin, X. Zheng, Q. Huang, S. Guan, X. Wang, C. Wang, F. Li, Typical crystal face effects of different morphology ceria on the activity of Pd/CeO₂ catalysts for lean methane combustion, *Fuel* 233 (2018) 10-20.
- [8] P. Losch, W. Huang, O. Vozniuk, E.D. Goodman, W. Schmidt, M. Cargnello, Modular Pd/Zeolite composites demonstrating the key role of support hydrophobic/hydrophilic character in methane catalytic combustion, *ACS Catal.* 9

(2019) 4742-4753.

[9] A. Toso, S. Colussi, J. Llorca, A. Trovarelli, The dynamics of PdO-Pd phase transformation in the presence of water over Si-doped Pd/CeO₂ methane oxidation catalysts, *Appl. Catal. A: Gen.* 574 (2019) 79-86.

[10] M. Monai, T. Montini, C. Chen, E. Fonda, R.J. Gorte, P. Fornasiero, Methane catalytic combustion over hierarchical Pd@CeO₂/Si-Al₂O₃: Effect of the presence of water, *ChemCatChem* 7 (2014) 2038-2046.

[11] N. Sadokhina, G. Smedler, U. Nylén, M. Olofsson, L. Olsson, Deceleration of SO₂ poisoning on PtPd/Al₂O₃ catalyst during complete methane oxidation, *Appl. Catal. B: Environ.* 236 (2018) 384-395.

[12] L. He, Y. Fan, J. Bellettre, J. Yue, L. Luo, A review on catalytic methane combustion at low temperatures: Catalysts, mechanisms, reaction conditions and reactor designs, *Renew. Sustain. Energy Rev.* 119 (2020) 109589.

[13] J. Lee, J. Kim, Y. Kim, S. Hwang, H. Lee, C.H. Kim, D.H. Kim, Improving NO_x storage and CO oxidation abilities of Pd/SSZ-13 by increasing its hydrophobicity, *Appl. Catal. B: Environ.* 277 (2020) 119190.

[14] A. Bolshakov, N. Kosinov, D.E. Romero Hidalgo, B. Mezari, A.J.F. van Hoof, E.J.M. Hensen, Mild dealumination of template-stabilized zeolites by NH₄F, *Catal. Sci. Technol.* 9 (2019) 4239-4247.

[15] Y. Sun, C. Li, I. Djerdj, O. Khalid, P. Cop, J. Sann, T. Weber, S. Werner, K. Turke, Y. Guo, B.M. Smarsly, H. Over, Oxygen storage capacity versus catalytic activity of ceria-zirconia solid solutions in CO and HCl oxidation, *Catal. Sci. Technol.* 9 (2019) 2163-2172.

[16] P. Govardhan, A.P. Anantharaman, S.S. Patil, H.P. Dasari, H. Dasari, A. Shourya, Effect of Ag loading on praseodymium doped ceria catalyst for soot oxidation activity, *Korean J. Chem. Eng.* 39 (2022) 328-342.

[17] K. Razmgar, M. Altarawneh, I. Oluwoye, G. Senanayake, Ceria-based catalysts for selective hydrogenation reactions: A critical review, *Catal. Surv. Asia*

25 (2021) 27-47.

[18] S. Zhang, J. Lee, D.H. Kim, T. Kim, NO reduction by CO over $\text{CoO}_x/\text{CeO}_2$ catalysts: Effect of support calcination temperature on activity, *Mol. Catal.* 482 (2020) 110703.

[19] H. Peng, C. Rao, N. Zhang, X. Wang, W. Liu, W. Mao, L. Han, P. Zhang, S. Dai, Confined ultrathin Pd-Ce nanowires with outstanding moisture and SO_2 tolerance in methane combustion, *Angew. Chem. Int. Ed.* 57 (2018) 8953-8957.

[20] S. Chen, S. Li, R. You, Z. Guo, F. Wang, G. Li, W. Yuan, B. Zhu, Y. Gao, Z. Zhang, H. Yang, Y. Wang, Elucidation of active sites for CH_4 catalytic oxidation over Pd/ CeO_2 via tailoring metal-support interactions, *ACS Catal.* 11 (2021) 5666-5677.

[21] S. Thomas, Review of ways to transport natural gas energy from countries which do not need the gas for domestic use, *Energy*, 28 (2003) 1461-1477.

[22] X. Mao, X. Guo, Y. Chang, Y. Peng, Improving air quality in large cities by substituting natural gas for coal in China: Changing idea and incentive policy implications, *Energy Policy* 33 (2005) 307-318.

[23] T.Y. Kim, S.B. Jo, C.H. Lee, S.-H. Kang, J.W. Kim, S.C. Lee, J.C. Kim, Effect of reducibility on the performance of Co-based catalysts for the production of high-calorie synthetic natural gas, *Korean J. Chem. Eng.* 37 (2020) 1690-1698.

[24] K. Murata, D. Kosuge, J. Ohyama, Y. Mahara, Y. Yamamoto, S. Arai, A. Satsuma, Exploiting metal-support interactions to tune the redox properties of supported Pd Catalysts for methane combustion, *ACS Catal.* 10 (2019) 1381-1387.

[25] Q. Yu, C. Wang, X. Li, Z. Li, L. Wang, Q. Zhang, G. Wu, Z. Li, Engineering an effective MnO_2 catalyst from LaMnO_3 for catalytic methane combustion, *Fuel* 239 (2019) 1240-1245.

[26] Y. Lou, J. Ma, W. Hu, Q. Dai, L. Wang, W. Zhan, Y. Guo, X.-M. Cao, Y. Guo, P. Hu, G. Lu, Low-temperature methane combustion over Pd/H-ZSM-5: Active Pd sites with specific electronic properties modulated by acidic sites of H-ZSM-5,

ACS Catal. 6 (2016) 8127-8139.

[27] Y. Ding, Q. Wu, B. Lin, Y. Guo, Y. Guo, Y. Wang, L. Wang, W. Zhan, Superior catalytic activity of a Pd catalyst in methane combustion by fine-tuning the phase of ceria-zirconia support, Appl. Catal B: Environ. 266 (2020) 118631.

[28] B.-J. Kim, K.-W. Jeon, H.-S. Na, Y.-L. Lee, S.-Y. Ahn, K.-J. Kim, W.-J. Jang, J.-O. Shim, H.-S. Roh, Reducible oxide (CeO_2 , ZrO_2 , and $\text{CeO}_2\text{-ZrO}_2$) promoted Ni-MgO catalysts for carbon dioxide reforming of methane reaction, Korean J. Chem. Eng. 37 (2020) 1130-1136.

[29] J. Li, M. Li, P. Gui, L. Zheng, J. Liang, G. Xue, Hydrothermal synthesis of sandwich interspersed $\text{LaCO}_3\text{OH}/\text{Co}_3\text{O}_4$ /graphene oxide composite and the enhanced catalytic performance for methane combustion, Catal. Today 327 (2019) 134-142.

[30] A. Choya, B. de Rivas, J.R. González-Velasco, J.I. Gutiérrez-Ortiz, R. López-Fonseca, On the beneficial effect of MgO promoter on the performance of $\text{Co}_3\text{O}_4/\text{Al}_2\text{O}_3$ catalysts for combustion of dilute methane, Appl. Catal. A: Gen. 582 (2019) 117099.

[31] R.B. Rakhi, W. Chen, D. Cha, H.N. Alshareef, Substrate dependent self-organization of mesoporous cobalt oxide nanowires with remarkable pseudocapacitance, Nano Lett. 12 (2012) 2559-2567.

[32] T.H. Lim, S.B. Park, J.M. Kim, D.H. Kim, Ordered mesoporous MCo_2O_4 ($\text{M}=\text{Cu}$, Zn and Ni) spinel catalysts with high catalytic performance for methane combustion, J. Mol. Catal. A: Chem. 426 (2017) 68-74.

[33] S. Gupta, C. Ciotonea, S. Royer, J.-P. Dacquin, C.P. Vinod, Engineering pore morphology using silica template route over mesoporous cobalt oxide and its implications in atmospheric pressure carbon dioxide hydrogenation to olefins, Appl. Mater. Today 19 (2020) 100586.

[34] Y. Peng, W. Si, J. Luo, W. Su, H. Chang, J. Li, J. Hao, J. Crittenden, Surface tuning of $\text{La}_{0.5}\text{Sr}_{0.5}\text{CoO}_3$ perovskite catalysts by acetic acid for NO_x storage and

reduction, *Environ. Sci. Technol.* 50 (2016) 6442-6448.

[35] W. Si, Y. Wang, Y. Peng, J. Li, Selective dissolution of A-Site cations in ABO_3 perovskites: A new path to high-performance catalysts, *Angew. Chem. Int. Ed.* 54 (2015) 7954-7957.

[36] P.J. Saines, J.R. Spencer, B.J. Kennedy, M. Avdeev, Structures and crystal chemistry of the double perovskites $\text{Ba}_2\text{LnB}'\text{O}_6$ (Ln =lanthanide $\text{B}'=\text{Nb}^{5+}$ and Ta^{5+}): Part I. Investigation of $\text{Ba}_2\text{LnTaO}_6$ using synchrotron X-ray and neutron powder diffraction, *J. Solid State Chem.* 180 (2007) 2991-3000.

[37] Z.N. Garba, W. Xiao, W. Zhou, I. Lawan, Y. Jiang, M. Zhang, Z. Yuan, Process optimization and synthesis of lanthanum-cobalt perovskite type nanoparticles (LaCoO_3) prepared by modified proteic method: Application of response surface methodology, *Korean J. Chem. Eng.* 36 (2019) 1826-1838.

[38] W. Tang, W. Xiao, S. Wang, Z. Ren, J. Ding, P.-X. Gao, Boosting catalytic propane oxidation over PGM-free Co_3O_4 nanocrystal aggregates through chemical leaching: A comparative study with Pt and Pd based catalysts, *Appl. Catal. B: Environ.* 226 (2018) 585-595.

[39] X. Fan, L. Li, F. Jing, J. Li, W. Chu, Effects of preparation methods on $\text{CoAlO}_x/\text{CeO}_2$ catalysts for methane catalytic combustion, *Fuel* 225 (2018) 588-595.

[40] S. Xie, Y. Liu, J. Deng, J. Yang, X. Zhao, Z. Han, K. Zhang, H. Dai, Insights into the active sites of ordered mesoporous cobalt oxide catalysts for the total oxidation of o-xylene, *J. Catal.* 352 (2017) 282-292.

[41] Y. Zheng, Y. Yu, H. Zhou, W. Huang, Z. Pu, Combustion of lean methane over Co_3O_4 catalysts prepared with different cobalt precursors, *RSC Adv.* 10 (2020) 4490-4498.

[42] Y. Wang, J. Ren, Y. Wang, F. Zhang, X. Liu, Y. Guo, G. Lu, Nanocasted synthesis of mesoporous LaCoO_3 perovskite with extremely high surface area and excellent activity in methane combustion, *J. Phys. Chem. C* 112 (2008) 15293-15298.

- [43] G. Ercolino, P. Stelmachowski, A. Kotarba, S. Specchia, Reactivity of mixed iron–cobalt spinels in the lean methane combustion, *Top. Catal.* 60 (2017) 1370-1379.
- [44] Z. Jiang, J. Yu, J. Cheng, T. Xiao, M.O. Jones, Z. Hao, P.P. Edwards, Catalytic combustion of methane over mixed oxides derived from Co–Mg/Al ternary hydrotalcites, *Fuel Process. Technol.* 91 (2010) 97-102.
- [45] R. Sanz, G. Calleja, A. Arencibia, E.S. Sanz-Pérez, Amino functionalized mesostructured SBA-15 silica for CO₂ capture: Exploring the relation between the adsorption capacity and the distribution of amino groups by TEM, *Microporous Mesoporous Mater.* 158 (2012) 309-317.
- [46] Y.-M. Liu, Y. Cao, N. Yi, W.-L. Feng, W.-L. Dai, S.-R. Yan, H.-Y. He, K.-N. Fan, Vanadium oxide supported on mesoporous SBA-15 as highly selective catalysts in the oxidative dehydrogenation of propane, *J. Catal.* 224 (2004) 417-428.
- [47] G. Wang, H. Liu, J. Horvat, B. Wang, S. Qiao, J. Park, H. Ahn, Highly ordered mesoporous cobalt oxide nanostructures: synthesis, characterisation, magnetic properties, and applications for electrochemical energy devices, *Chemistry* 16 (2010) 11020-11027.
- [48] B. Bai, H. Arandiyán, J. Li, Comparison of the performance for oxidation of formaldehyde on nano-Co₃O₄, 2D-Co₃O₄, and 3D-Co₃O₄ catalysts, *Appl. Catal. B: Environ.* 142-143 (2013) 677-683.
- [49] J. Taghavimoghaddam, G.P. Knowles, A.L. Chaffee, Preparation and characterization of mesoporous silica supported cobalt oxide as a catalyst for the oxidation of cyclohexanol, *J. Mol. Catal. A: Chem.* 358 (2012) 79-88.
- [50] R. Kumar, R.K. Singh, M.K. Zope, M. Kar, Tuning of magnetic property by lattice strain in lead substituted cobalt ferrite, *Mater. Sci. Eng. B*, 220 (2017) 73-81.
- [51] L.-H. Ai, J. Jiang, Rapid synthesis of nanocrystalline Co₃O₄ by a microwave-assisted combustion method, *Powder Technol.* 195 (2009) 11-14.
- [52] S.K. Tripathy, M. Christy, N.-H. Park, E.-K. Suh, S. Anand, Y.-T. Yu,

Hydrothermal synthesis of single-crystalline nanocubes of Co_3O_4 , *Mater. Lett.* 62 (2008) 1006-1009.

[53] Q. Liu, L.-C. Wang, M. Chen, Y. Cao, H.-Y. He, K.-N. Fan, Dry citrate-precursor synthesized nanocrystalline cobalt oxide as highly active catalyst for total oxidation of propane, *J. Catal.* 263 (2009) 104-113.

[54] Z. Cheng, L. Qin, M. Guo, M. Xu, J.A. Fan, L.S. Fan, Oxygen vacancy promoted methane partial oxidation over iron oxide oxygen carriers in the chemical looping process, *Phys. Chem. Chem. Phys.* 18 (2016) 32418-32428.

[55] L. Xue, C. Zhang, H. He, Y. Teraoka, Catalytic decomposition of N_2O over CeO_2 promoted Co_3O_4 spinel catalyst, *Appl. Catal. B: Environ.* 75 (2007) 167-174.

[56] A. Ruiz Puigdollers, P. Schlexer, S. Tosoni, G. Pacchioni, Increasing oxide reducibility: The role of metal/oxide interfaces in the formation of oxygen vacancies, *ACS Catal.* 7 (2017) 6493-6513.

[57] A.M. Ali, E.A.C. Emanuelsson, D.A. Patterson, Conventional versus lattice photocatalysed reactions: Implications of the lattice oxygen participation in the liquid phase photocatalytic oxidation with nanostructured ZnO thin films on reaction products and mechanism at both 254nm and 340nm, *Appl. Catal. B: Environ.* 106 (2011) 323-336.

[58] L.F. Liotta, M. Ousmane, G. Di Carlo, G. Pantaleo, G. Deganello, G. Marci, L. Retailleau, A. Giroir-Fendler, Total oxidation of propene at low temperature over $\text{Co}_3\text{O}_4\text{-CeO}_2$ mixed oxides: Role of surface oxygen vacancies and bulk oxygen mobility in the catalytic activity, *Appl. Catal. A: Gen.* 347 (2008) 81-88.

[59] L. Cheng, Z. Liu, S. Yuan, M. Wei, X. Hu, B. Zhang, Y. Jiang, Sol-gel citrate procedure to synthesize $\text{Ag/Co}_3\text{O}_4$ catalysts with enhanced activity for propane catalytic combustion, *Chem. Pap.* 74 (2019) 1449-1457.

[60] A. Choya, B. de Rivas, J. Gutiérrez-Ortiz, R. López-Fonseca, Effect of residual Na^+ on the combustion of methane over Co_3O_4 bulk catalysts prepared by precipitation, *Catalysts* 8 (2018) 427.

- [61] C. Huck-Iriart, L. Soler, A. Casanovas, C. Marini, J. Prat, J. Llorca, C. Escudero, Unraveling the chemical state of cobalt in Co-based catalysts during ethanol steam reforming: an in situ study by near ambient pressure XPS and XANES, *ACS Catal.* 8 (2018) 9625-9636.
- [62] L.F. Liotta, G. Di Carlo, G. Pantaleo, A.M. Venezia, G. Deganello, $\text{Co}_3\text{O}_4/\text{CeO}_2$ composite oxides for methane emissions abatement: Relationship between Co_3O_4 – CeO_2 interaction and catalytic activity, *Appl. Catal. B: Environ.* 66 (2006) 217-227.
- [63] Z. Zhu, G. Lu, Z. Zhang, Y. Guo, Y. Guo, Y. Wang, Highly active and stable $\text{Co}_3\text{O}_4/\text{ZSM-5}$ catalyst for propane oxidation: Effect of the preparation method, *ACS Catal.* 3 (2013) 1154-1164.
- [64] N.A. Merino, B.P. Barbero, P. Eloy, L.E. Cadús, $\text{La}_{1-x}\text{Ca}_x\text{CoO}_3$ perovskite-type oxides: Identification of the surface oxygen species by XPS, *Appl. Surf. Sci.* 253 (2006) 1489-1493.
- [65] Y. Liu, D. Sun, Effect of CeO_2 doping on catalytic activity of $\text{Fe}_2\text{O}_3/\text{gamma-Al}_2\text{O}_3$ catalyst for catalytic wet peroxide oxidation of azo dyes, *J. Hazard. Mater.* 143 (2007) 448-454.
- [66] S. Chen, L. Li, W. Hu, X. Huang, Q. Li, Y. Xu, Y. Zuo, G. Li, Anchoring high-concentration oxygen vacancies at interfaces of $\text{CeO}_{2-x}/\text{Cu}$ toward enhanced activity for preferential CO oxidation, *ACS Appl. Mater. Interfaces* 7 (2015) 22999-23007.
- [67] Z. Wang, W. Wang, L. Zhang, D. Jiang, Surface oxygen vacancies on Co_3O_4 mediated catalytic formaldehyde oxidation at room temperature, *Catal. Sci. Technol.* 6 (2016) 3845-3853.
- [68] F. Zasada, J. Gryboś, C. Hudy, J. Janas, Z. Sojka, Total oxidation of lean methane over cobalt spinel nanocubes—Mechanistic vistas gained from DFT modeling and catalytic isotopic investigations, *Catal. Today*, 354 (2020) 183-195.
- [69] H. Wakamatsu, K. Aruga, The impact of the shale gas revolution on the U.S. and Japanese natural gas markets, *Energy Policy* 62 (2013) 1002-1009.

- [70] A.-H. Kakaee, A. Paykani, M. Ghajar, The influence of fuel composition on the combustion and emission characteristics of natural gas fueled engines, *Renew. Sustain. Energy Rev.* 38 (2014) 64-78.
- [71] P. Deng, J. Liang, Y. Wu, T. Li, Dynamic boil-off characterization for discharge process of LNG vehicle tank, *Energy* 186 (2019) 115813.
- [72] W. Shi, G. Pan, Q. Chen, L. Song, L. Zhu, X. Ji, Hypoxia Remediation and Methane Emission Manipulation Using Surface Oxygen Nanobubbles, *Environ. Sci. Technol.* 52 (2018) 8712-8717.
- [73] G. Corro, J. Cruz-Mérida, D. Montalvo, U. Pal, Performance of Pt/Cr₂O₃, Pt/ZrO₂, and, Pt/ γ -Al₂O₃ catalysts in total oxidation of methane: Effect of metal-support interaction, *Ind. Eng. Chem. Res.* 60 (2021) 18841-18852.
- [74] P. Velin, M. Ek, M. Skoglundh, A. Schaefer, A. Raj, D. Thompsett, G. Smedler, P.-A. Carlsson, Water inhibition in methane oxidation over alumina supported palladium catalysts, *J. Phys. Chem. C* 123 (2019) 25724-25737.
- [75] J.J. Willis, A. Gallo, D. Sokaras, H. Aljama, S.H. Nowak, E.D. Goodman, L. Wu, C.J. Tassone, T.F. Jaramillo, F. Abild-Pedersen, M. Cargnello, Systematic structure-property relationship studies in palladium-catalyzed methane complete combustion, *ACS Catal.* 7 (2017) 7810-7821.
- [76] Y. Ryou, J. Lee, S.J. Cho, H. Lee, C.H. Kim, D.H. Kim, Activation of Pd/SSZ-13 catalyst by hydrothermal aging treatment in passive NO adsorption performance at low temperature for cold start application, *Appl. Catal. B: Environ.* 212 (2017) 140-149.
- [77] B. Fan, D. Zhu, L. Wang, S. Xu, Y. Wei, Z. Liu, Dynamic evolution of Al species in the hydrothermal dealumination process of CHA zeolites, *Inorg. Chem. Front.* 9 (2022) 3609-3618.
- [78] R. Zhang, R. Zou, W. Li, Y. Chang, X. Fan, On understanding the sequential post-synthetic microwave-assisted dealumination and alkaline treatment of Y zeolite, *Microporous Mesoporous Mater.* 333 (2022) 111736.

- [79] J.V. Milato, R.J. França, A.S. Rocha, M.R.C.M. Calderari, Catalytic co-pyrolysis of oil sludge with HDPE to obtain paraffinic products over HUSY zeolites prepared by dealumination and desilication, *J. Anal. Appl. Pyrolysis* 151 (2020) 104928.
- [80] M. Sun, Q. Gu, A. Hanif, T. Wang, J. Shang, Transition metal cation-exchanged SSZ-13 zeolites for CO₂ capture and separation from N₂, *Chem. Eng. J.* 370 (2019) 1450-1458.
- [81] Y. Ryou, J. Lee, Y. Kim, S. Hwang, H. Lee, C.H. Kim, D.H. Kim, Effect of reduction treatments (H₂ vs. CO) on the NO adsorption ability and the physicochemical properties of Pd/SSZ-13 passive NO_x adsorber for cold start application, *Appl. Catal. A: Gen.* 569 (2019) 28-34.
- [82] Z. Xu, J. Li, Y. Huang, H. Ma, W. Qian, H. Zhang, W. Ying, Size control of SSZ-13 crystals with APAM and its influence on the coking behaviour during MTO reaction, *Catal. Sci. Technol.* 9 (2019) 2888-2897.
- [83] L. Luo, J.D. LaCoste, N.G. Khamidullina, E. Fox, D.D. Gang, R. Hernandez, H. Yan, Investigate interactions of water with mesoporous ceria using in situ VT-DRIFTS, *Surf. Sci.* 691 (2020) 121486.
- [84] C. Wang, H. Guo, S. Leng, J. Yu, K. Feng, L. Cao, J. Huang, Regulation of hydrophilicity/hydrophobicity of aluminosilicate zeolites: a review, *Crit. Rev. Solid State Mater. Sci.* 46 (2020) 330-348.
- [85] Y. Cui, J. Zhu Chen, B. Peng, L. Kovarik, A. Devaraj, Z. Li, T. Ma, Y. Wang, J. Szanyi, J.T. Miller, Y. Wang, F. Gao, Onset of high methane combustion rates over supported palladium catalysts: From isolated Pd cations to PdO nanoparticles, *JACS Au* 1 (2021) 396-408.
- [86] H. Zhang, Q. Dong, P. Shan, D. Pan, B. Fan, R. Li, Synthesis of highly crystallized SSZ-13 with a small amount of organic structure-directing agent in the presence of seeds, *Microporous Mesoporous Mater.* 324 (2021) 111287.
- [87] J. Lee, Y. Ryou, S. Hwang, Y. Kim, S.J. Cho, H. Lee, C.H. Kim, D.H. Kim,

Comparative study of the mobility of Pd species in SSZ-13 and ZSM-5, and its implication for their activity as passive NO_x adsorbers (PNAs) after hydro-thermal aging, *Catal. Sci. Technol.* 9 (2019) 163-173.

[88] D. Chen, H. Lei, W. Xiong, Y. Li, X. Ji, J.-Y. Yang, B. Peng, M. Fu, P. Chen, D. Ye, Unravelling phosphorus-induced deactivation of Pd-SSZ-13 for passive NO_x adsorption and CO oxidation, *ACS Catal.* 11 (2021) 13891-13901.

[89] T. Ryu, J. Jeong, S.W. Byun, S. Kweon, J. Park, W.B. Bae, D.Y. Kim, Y.J. Kim, M.B. Park, S.B. Kang, Ethylene trapping of palladium-impregnated zeolites for cold-start emission control, *Chem. Eng. J.* 442 (2022) 136197.

[90] A. Tuel, D. Farrusseng, Hollow zeolite single crystals: Synthesis routes and functionalization methods, *Small Methods* 2 (2018) 1800197.

[91] I. Friberg, A.H. Clark, P.H. Ho, N. Sadokhina, G.J. Smales, J. Woo, X. Auvray, D. Ferri, M. Nachtegaal, O. Kröcher, L. Olsson, Structure and performance of zeolite supported Pd for complete methane oxidation, *Catal. Today*, 382 (2021) 3-12.

[92] Y.-H. Chin, M. García-Diéguez, E. Iglesia, Dynamics and thermodynamics of Pd-PdO phase transitions: Effects of Pd cluster size and kinetic implications for catalytic methane combustion, *J. Phys. Chem. C* 120 (2016) 1446-1460.

[93] E.D. Goodman, A.C. Johnston-Peck, E.M. Dietze, C.J. Wrasman, A.S. Hoffman, F. Abild-Pedersen, S.R. Bare, P.N. Plessow, M. Cargnello, Supported catalyst deactivation by decomposition into single atoms is suppressed by increasing metal loading, *Nat. Catal.* 2 (2019) 748-755.

[94] Q. Zhang, W. Ming, J. Ma, J. Zhang, P. Wang, R. Li, De novo assembly of a mesoporous beta zeolite with intracrystalline channels and its catalytic performance for biodiesel production, *J. Mater. Chem. A* 2 (2014) 8712-8718.

[95] Y. Kim, J. Sung, S. Kang, J. Lee, M.-H. Kang, S. Hwang, H. Park, J. Kim, Y. Kim, E. Lee, G.-S. Park, D.H. Kim, J. Park, Uniform synthesis of palladium species confined in a small-pore zeolite via full ion-exchange investigated by cryogenic

- electron microscopy, *J. Mater. Chem. A* 9 (2021) 19796-19806.
- [96] T. Franken, M. Roger, A.W. Petrov, A.H. Clark, M. Agote-Arán, F. Krumeich, O. Kröcher, D. Ferri, Effect of short reducing pulses on the dynamic structure, activity, and stability of Pd/Al₂O₃ for wet lean methane oxidation, *ACS Catal.* 11 (2021) 4870-4879.
- [97] R.L. Mortensen, H.D. Noack, K. Pedersen, S. Mossin, J. Mielby, Recent advances in complete methane oxidation using zeolite-supported metal nanoparticle catalysts, *ChemCatChem* 14 (2022) e202101924.
- [98] H. Hosseiniamoli, A. Setiawan, A.A. Adesina, E.M. Kennedy, M. Stockenhuber, The stability of Pd/TS-1 and Pd/silicalite-1 for catalytic oxidation of methane – understanding the role of titanium, *Catal. Sci. Technol.* 10 (2020) 1193-1204.
- [99] G. Corro, A. Flores, F. Pacheco-Aguirre, U. Pal, F. Bañuelos, A. Ramirez, A. Zehe, Biodiesel and fossil-fuel diesel soot oxidation activities of Ag/CeO₂ catalyst, *Fuel* 250 (2019) 17-26.
- [100] S. Hoang, X. Lu, W. Tang, S. Wang, S. Du, C.-Y. Nam, Y. Ding, R.D. Vinluan, J. Zheng, P.-X. Gao, High performance diesel oxidation catalysts using ultra-low Pt loading on titania nanowire array integrated cordierite honeycombs, *Catal. Today* 320 (2019) 2-10.
- [101] J. Chen, Y. Wu, W. Hu, P. Qu, X. Liu, R. Yuan, L. Zhong, Y. Chen, Insights into the role of Pt on Pd catalyst stabilized by magnesia-alumina spinel on gamma-alumina for lean methane combustion: Enhancement of hydrothermal stability, *Mol. Catal.* 496 (2020) 111185.
- [102] X. Zhao, Y. Liu, J. Deng, P. Xu, J. Yang, K. Zhang, Z. Han, H. Dai, Mesoporous Pd Pt alloys: High-performance catalysts for methane combustion, *Mol. Catal.* 442 (2017) 191-201.
- [103] P. Xu, X. Zhao, X. Zhang, L. Bai, H. Chang, Y. Liu, J. Deng, G. Guo, H. Dai, Three-dimensionally ordered macroporous LaMnAl₁₁O₁₉-supported Pd

nanocatalysts highly active for methane combustion, *Mol. Catal.* 439 (2017) 200-210.

[104] N. Yang, S. Ni, Y. Sun, Y. Zhu, A facial strategy to synthesize Pd/Co₃O₄ nanosheets with enhanced performance for methane catalytic oxidation, *Mol. Catal.* 452 (2018) 28-35.

[105] F. Jiang, S. Wang, B. Liu, J. Liu, L. Wang, Y. Xiao, Y. Xu, X. Liu, Insights into the influence of CeO₂ crystal facet on CO₂ hydrogenation to methanol over Pd/CeO₂ catalysts, *ACS Catal.* 10 (2020) 11493-11509.

[106] Z. Hu, X. Liu, D. Meng, Y. Guo, Y. Guo, G. Lu, Effect of ceria crystal plane on the physicochemical and catalytic properties of Pd/Ceria for CO and propane oxidation, *ACS Catal.* 6 (2016) 2265-2279.

[107] J. Ma, Y. Lou, Y. Cai, Z. Zhao, L. Wang, W. Zhan, Y. Guo, Y. Guo, The relationship between the chemical state of Pd species and the catalytic activity for methane combustion on Pd/CeO₂, *Catal. Sci. Technol.* 8 (2018) 2567-2577.

[108] M. Khader, M. Al-Marri, S. Ali, A. Abdelmoneim, Active and stable methane oxidation nano-catalyst with highly-ionized palladium species prepared by solution combustion synthesis, *Catalysts*, 8 (2018) 66.

[109] M. Danielis, L.E. Betancourt, I. Orozco, N.J. Divins, J. Llorca, J.A. Rodríguez, S.D. Senanayake, S. Colussi, A. Trovarelli, Methane oxidation activity and nanoscale characterization of Pd/CeO₂ catalysts prepared by dry milling Pd acetate and ceria, *Appl. Catal. B: Environ.* 282 (2021) 119567.

[110] Y. Liu, Y. Cai, X. Tang, C. Shao, Y. You, L. Wang, W. Zhan, Y. Guo, Y. Zhao, Y. Guo, Insight into the roles of Pd state and CeO₂ property in C₃H₈ catalytic oxidation on Pd/CeO₂, *Appl. Surf. Sci.* 605 (2022) 154675.

[111] M. Danielis, S. Colussi, C. de Leitenburg, A. Trovarelli, The role of palladium salt precursors in Pd-PdO/CeO₂ catalysts prepared by dry milling for methane oxidation, *Catal. Commun.* 135 (2020) 105899.

[112] R.S. Monteiro, L.C. Dieguez, M. Schmal, The role of Pd precursors in the

oxidation of carbon monoxide over Pd/Al₂O₃ and Pd/CeO₂/Al₂O₃ catalysts, *Catal. Today* 65 (2001) 77-89.

[113] A. Aznárez, A. Gil, S.A. Korili, Performance of palladium and platinum supported on alumina pillared clays in the catalytic combustion of propene, *RSC Adv.* 5 (2015) 82296-82309.

[114] Y. Yang, J. Lee, R. Dorakhan, H. Nie, G. Fu, A. Quarantotto, J.Y. Howe, Y.-H. Chin, Active site structure and methane oxidation reactivity of bimetallic Pd and Pt nanoparticles, *Appl. Catal. A: Gen.* 629 (2022) 118290.

[115] J.F. Weaver, J. Choi, V. Mehar, C. Wu, Kinetic coupling among metal and oxide phases during CO oxidation on partially reduced PdO (101): Influence of gas-phase composition, *ACS Catal.* 7 (2017) 7319-7331.

[116] C. Wang, X.-K. Gu, H. Yan, Y. Lin, J. Li, D. Liu, W.-X. Li, J. Lu, Water-mediated Mars–Van Krevelen mechanism for CO Oxidation on ceria-supported single-atom Pt₁ catalyst, *ACS Catal.* 7 (2016) 887-891.

[117] J. Yang, M. Peng, G. Ren, H. Qi, X. Zhou, J. Xu, F. Deng, Z. Chen, J. Zhang, K. Liu, X. Pan, W. Liu, Y. Su, W. Li, B. Qiao, D. Ma, T. Zhang, A hydrothermally stable irreducible oxide-modified Pd/MgAl₂O₄ catalyst for methane combustion, *Angew. Chem. Int. Ed.* 59 (2020) 18522-18526.

[118] J. Lee, Y. Ryou, J. Kim, X. Chan, T.J. Kim, D.H. Kim, Influence of the defect concentration of ceria on the Pt dispersion and the CO oxidation activity of Pt/CeO₂, *J. Phys. Chem. C*, 122 (2018) 4972-4983.

[119] L.A. Gonzaga, V.T. Santana, M.I.B. Bernardi, J. Hrubý, P. Neugebauer, A. Mesquita, CeO₂ and CeO₂:Pr nanocrystalline powders prepared by the polymeric precursor method: Yellow and red pigments with tunable color, *J. Am. Ceram. Soc.* 103 (2020) 6280-6288.

[120] M. Machida, A. Fujiwara, H. Yoshida, J. Ohyama, H. Asakura, S. Hosokawa, T. Tanaka, M. Haneda, A. Tomita, T. Miki, K. Iwashina, Y. Endo, Y. Nakahara, S. Minami, N. Kato, Y. Hayashi, H. Goto, M. Hori, T. Tsuda, K. Miura, F. Kimata, K.

Iwachido, Deactivation mechanism of Pd/CeO₂–ZrO₂ three-Way catalysts analyzed by chassis-dynamometer tests and in situ diffuse reflectance spectroscopy, *ACS Catal.* 9 (2019) 6415-6424.

[121] E. Ismail, M. Khenfouch, M. Dhlamini, S. Dube, M. Maaza, Green palladium and palladium oxide nanoparticles synthesized via *Aspalathus linearis* natural extract, *J. Alloys Compd.* 695 (2017) 3632-3638.

[122] H. Tan, J. Wang, S. Yu, K. Zhou, Support morphology-dependent catalytic activity of Pd/CeO₂ for formaldehyde oxidation, *Environ. Sci. Technol.* 49 (2015) 8675-8682.

[123] R. Khobragade, M. Roškarič, G. Žerjav, M. Košiček, J. Zavašnik, N. Van de Velde, I. Jerman, N.N. Tušar, A. Pintar, Exploring the effect of morphology and surface properties of nanoshaped Pd/CeO₂ catalysts on CO₂ hydrogenation to methanol, *Appl. Catal. A: Gen.* 627 (2021) 118394.

[124] Y. Kim, G. Collinge, M.S. Lee, K. Khivantsev, S.J. Cho, V.A. Glezakou, R. Rousseau, J. Szanyi, J.H. Kwak, Surface density dependent catalytic activity of single palladium atoms supported on ceria, *Angew. Chem. Int. Ed.* 60 (2021) 22769-22775.

[125] L. Zhang, F. Wang, J. Zhu, B. Han, W. Fan, L. Zhao, W. Cai, Z. Li, L. Xu, H. Yu, W. Shi, CO₂ reforming with methane reaction over Ni@SiO₂ catalysts coupled by size effect and metal-support interaction, *Fuel* 256 (2019) 115954.

[126] G. Jacobs, J.A. Chaney, P.M. Patterson, T.K. Das, B.H. Davis, Fischer–Tropsch synthesis: study of the promotion of Re on the reduction property of Co/Al₂O₃ catalysts by in situ EXAFS/XANES of Co K and Re L_{III} edges and XPS, *Appl. Catal. A: Gen.* 264 (2004) 203-212.

[127] A. Toso, S. Colussi, S. Padigapaty, C. de Leitenburg, A. Trovarelli, High stability and activity of solution combustion synthesized Pd-based catalysts for methane combustion in presence of water, *Appl. Catal. B: Environ.* 230 (2018) 237-245.

- [128] S. Hinokuma, H. Fujii, Y. Katsuhara, K. Ikeue, M. Machida, Effect of thermal ageing on the structure and catalytic activity of Pd/CeO₂ prepared using arc-plasma process, *Catal. Sci. Technol.* 4 (2014) 2990-2996.
- [129] E.K. Dann, E.K. Gibson, C.R.A. Catlow, V. Celorrio, P. Collier, T. Eralp, M. Amboage, C. Hardacre, C. Stere, A. Kroner, A. Raj, S. Rogers, A. Goguet, P.P. Wells, Combined spatially resolved operando spectroscopy: New insights into kinetic oscillations of CO oxidation on Pd/ γ -Al₂O₃, *J. Catal.* 373 (2019) 201-208.
- [130] M.A. Newton, D. Ferri, C.J. Mulligan, I. Alxneit, H. Emerich, P.B.J. Thompson, K.K. Hii, In situ study of metal leaching from Pd/Al₂O₃ induced by K₂CO₃, *Catal. Sci. Technol.* 10 (2020) 466-474.
- [131] Y. Ryou, J. Lee, H. Lee, C.H. Kim, D.H. Kim, Effect of various activation conditions on the low temperature NO adsorption performance of Pd/SSZ-13 passive NO_x adsorber, *Catal. Today* 320 (2019) 175-180.
- [132] X. Feng, D. Liu, B. Yan, M. Shao, Z. Hao, G. Yuan, H. Yu, Y. Zhang, Highly active PdO/Mn₃O₄/CeO₂ nanocomposites supported on one dimensional halloysite nanotubes for photoassisted thermal catalytic methane combustion, *Angew. Chem. Int. Ed.* 60 (2021) 18552-18556.
- [133] Y. Seo, M.W. Lee, H.J. Kim, J.W. Choung, C. Jung, C.H. Kim, K.Y. Lee, Effect of Ag doping on Pd/Ag-CeO₂ catalysts for CO and C₃H₆ oxidation, *J. Hazard. Mater.* 415 (2021) 125373.
- [134] A.J. Hill, C.Y. Seo, X. Chen, A. Bhat, G.B. Fisher, A. Lenert, J.W. Schwank, Thermally induced restructuring of Pd@CeO₂ and Pd@SiO₂ nanoparticles as a strategy for enhancing low-temperature catalytic activity, *ACS Catal.* 10 (2019) 1731-1741.
- [135] C. Du, Y. Guo, Y. Guo, X.-q. Gong, G. Lu, Polymer-templated synthesis of hollow Pd-CeO₂ nanocomposite spheres and their catalytic activity and thermal stability, *J. Mater. Chem. A* 3 (2015) 23230-23239.
- [136] I. Ro, I.B. Aragao, J.P. Chada, Y. Liu, K.R. Rivera-Dones, M.R. Ball, D.

Zanchet, J.A. Dumesic, G.W. Huber, The role of Pt-Fe_xO_y interfacial sites for CO oxidation, *J. Catal.* 358 (2018) 19-26.

[137] H. Li, M. Shen, J. Wang, H. Wang, J. Wang, Effect of support on CO oxidation performance over the Pd/CeO₂ and Pd/CeO₂-ZrO₂ Catalyst, *Ind. Eng. Chem. Res.* 59 (2020) 1477-1486.

[138] B. Wang, D. Weng, X. Wu, J. Fan, Influence of H₂/O₂ redox treatments at different temperatures on Pd-CeO₂ catalyst: Structure and oxygen storage capacity, *Catal. Today* 153 (2010) 111-117.

[139] E.M. Slavinskaya, R.V. Gulyaev, A.V. Zadesenets, O.A. Stonkus, V.I. Zaikovskii, Y.V. Shubin, S.V. Korenev, A.I. Boronin, Low-temperature CO oxidation by Pd/CeO₂ catalysts synthesized using the coprecipitation method, *Appl. Catal. B: Environ.* 166-167 (2015) 91-103.

초 록

천연가스는 지구상에서 가장 풍부한 에너지원 중 하나이며 발전, 난방, 운송에 사용될 수 있다. 천연가스의 주요 성분은 메탄이며, 기존의 석유 기반 연료보다 연소 중에 오염을 덜 발생시킨다. 따라서, 질소산화물, 황산화물 및 탄화수소의 배출을 줄이기 위해 가솔린 및 디젤 엔진이 천연가스 엔진으로 대거 대체되고 있다. 하지만, 일부 미연소된 메탄이 천연 가스 차량에서 배출된다. 메탄의 지구 온난화 지수가 이산화탄소보다 25배 이상 높기 때문에 환경 보호를 위해 메탄 배출 규제가 적용될 것으로 전망된다. 촉매를 사용한 메탄 연소 반응은 ($\text{CH}_4 + 2\text{O}_2 \rightarrow \text{CO}_2 + 2\text{H}_2\text{O}$) 천연 가스 엔진의 메탄 배출을 감소시키는 가장 효과적인 방법이다. 그러나 메탄은 강한 C-H 결합을 가지고 있어 매우 안정한 물질이기 때문에 메탄 산화 반응은 높은 온도를 요구하고 에너지 소모가 매우 크다. 따라서, 이 과정의 에너지 소비를 줄이기 위해서는 저온 메탄 산화 반응을 위한 촉매가 필요하다.

Pd 기반 귀금속 촉매가 메탄 연소 반응에 가장 널리 사용되며 가장 활성이 우수한 촉매이다. 그러나 귀금속의 불안정한 가격때문에 실제 산업으로의 적용이 어렵다. Pd 촉매의 대체재로, 페로브스카이트 또는 스피넬 산화물과 같은 전이 금속 산화물 촉매가 있다. 이러한 전이금속 산화물 중 스피넬 형태의 코발트 산화물이 산화 반응에 널리 사용되고 있다. 그러나, Pd 촉매에 비해 코발트 산화물의 반응 활성이 매우 낮기 때문에 저온 메탄 산화 반응에 곧바로 적용하기 어렵다.

제 2장에서는 벌크 코발트 산화물 촉매의 낮은 반응 활성을 두 가지 다른 방법으로 향상시켰다. 첫째, 중형기공의 도입으로 벌크 촉매

의 낮은 표면적을 개선하였다. 둘째, 합성된 중형기공성 코발트 산화물 촉매를 질산으로 처리하여 표면 구조를 개선하였다. 제조된 촉매를 사용하여 메탄 연소 반응을 진행했으며, 산처리된 촉매는 기존 촉매에 비해 반응 활성이 크게 향상된 것을 확인하였다. 다양한 분석 기법을 사용하여 산처리된 촉매의 특성 분석을 진행하였다. 투과 및 주사전자현미경 이미지는 산처리된 촉매의 표면이 거칠어지는 것을 보여주었다. 한편, 수소 승온 환원 결과를 통해, 산처리 후 코발트 산화물의 환원성이 향상되는 것을 확인할 수 있었다. 또한, 산소 승온 탈착 및 X선 광전자 분광 분석 결과, 산처리된 촉매가 기존 촉매보다 표면에 화학 흡착된 산소를 더 많이 보유한 것으로 밝혀졌으며, 이를 통해 산처리된 촉매의 향상된 환원성 및 산화 반응 활성을 설명할 수 있다. 즉, 산처리는 메탄 연소 반응을 위한 높은 활성을 가지는 벌크 산화물 촉매의 합성에 유용한 방법이라고 결론을 내릴 수 있다.

산 처리에 의해 코발트 산화물 촉매의 메탄 산화 활성을 크게 증가시킬 수 있었지만, 촉매 활성은 여전히 귀금속 촉매에 비해 낮았다. 귀금속 촉매, 특히 Pd를 포함하는 촉매는 다양한 산화 반응에 대한 우수한 활성으로 인해 상당한 주목을 받고 있다. 귀금속 촉매는 높은 가격 때문에 일반적으로 알루미나, 세리아, 제올라이트 등의 지지체에 소량의 귀금속을 분산시켜 제조된다. 하지만 Pd 촉매는 배기가스 내의 물에 취약한데, 물은 촉매의 초기 활성을 심각하게 저해하고 장기 운전시 비활성화를 일으키는 것으로 알려져 있다. 물에 내성이 있는 촉매를 합성하기 위한 가능한 해결책 중 하나는 소수성 지지체를 사용하는 것이다. 다양한 지지체 중 제올라이트는 Si/Al₂ 비율을 증가시켜 소수성을 향상시킬 수 있기 때문에 메탄 산화 촉매를 위한 효과적인 지지체가 될 수 있다. 제올라이트는 고온에서 증기 처리에 의해 쉽게 탈알루미늄화될 수

있으며, 이는 종종 수열 처리라고 불린다.

제 3장에서는 탈알루미늄화가 Pd/SSZ-13 촉매의 메탄 연소 반응 활성화에 미치는 영향을 조사하였다. Pd/SSZ-13 촉매를 수열 처리하여 제조한 Pd(1)/SSZ-13(HTA)는 매우 낮은 촉매 활성을 나타내었다. 반면에, SSZ-13 지지체를 수열 처리한 후에 Pd를 담지하여 제조한 Pd(1)/SSZ-13(DeAl) 촉매가 가장 높은 촉매 활성을 보였다. 제올라이트 소수성, Pd 위치 및 상태 등의 촉매 특성을 다양한 분석 기법을 이용하여 조사하였다. Pd/SSZ-13(HTA) 촉매에 포함된 대부분의 Pd 종은 Pd 이온으로 존재하였으며, Pd 이온은 메탄 산화 반응 활성이 거의 없었다. 반면에, Pd(1)/SSZ-13(DeAl) 촉매에 포함된 대부분의 Pd 종들은 외부 표면에 PdO 나노입자로 존재하여 메탄 산화 반응 활성이 높았다. 결론적으로, 메탄 연소 반응에 높은 활성을 보이는 Pd/SSZ-13 촉매를 합성하기 위해서는 외부 표면에 존재하는 PdO 나노입자의 양을 극대화해야 하는데, 이는 Pd 담지전에 SSZ-13 지지체의 탈알루미늄화를 진행하면 가능하다.

앞선 연구에서 제올라이트 지지체의 소수성이 촉매 활성화에 큰 영향을 끼치지 않는 것을 확인했기 때문에 다른 지지체를 사용해보았다. 세리아는 일반적으로 Ce^{4+}/Ce^{3+} 사이클에서 발생하는 산화 환원 특성, 담지된 금속과의 강한 상호 작용 및 높은 산소 저장 용량으로 인해 산화 반응에 자주 활용된다. 귀금속의 매장량이 제한적이기 때문에, 낮은 금속 함량으로 높은 활성을 보이는 촉매의 제조가 필요하다. Pd/CeO₂ 촉매의 Pd 종은 다양한 상태로 존재할 수 있으며, 일반적으로 금속 Pd나 PdO 나노입자 상태이지만, Pd_xCe_{1-x}O_{2-δ} 고용체를 형성하여 세리아 결합 부위에 안정화된 고분산된 Pd 이온으로도 존재할 수 있다. 각 Pd 종은 서로 다른 반응에 대해 서로 다른 촉매 활성을 나타낸다. 따라서, 우

수한 활성을 보이는 촉매를 제조하려면 목표 반응에 적합한 Pd 상태에 대한 이해가 필요하다.

제 4장에서는 Pd/CeO₂ 촉매에서 Pd 전구체가 Pd 상태에 어떠한 영향을 끼치는지 연구하였다. 서로 다른 Pd 전구체를 사용하여 Pd/CeO₂ 촉매를 제조했으며 CH₄ 및 CO 산화 반응에 적용하였다. 팔라듐 나이트레이트 (Pd(2)/CeO₂(N))를 사용하여 제조된 촉매는 CH₄ 산화 반응에 대하여 높은 활성을 보였으며, 반면에 팔라듐 아세테이트 (Pd(2)/CeO₂(A))를 사용하여 제조된 촉매는 높은 CO 산화 활성을 나타내었다. 촉매 활성 및 특성에 대한 전구체의 영향은 다양한 분석 기법을 사용하여 연구되었다. Pd(2)/CeO₂(N) 촉매는 CH₄ 산화를 위한 활성 상인 PdO 나노입자를 표면에 보유하고 있었다. 반면, Pd(2)/CeO₂(A) 촉매는 CeO₂ 결합 부위에 안정화된 Pd 이온을 가지고 있었으며, 이는 반응성이 매우 낮았다. 그러나, 높은 Pd 분산도는 CO 산화 반응에 유리하였다. 결론적으로, Pd 전구체는 촉매 활성에 중요한 Pd/CeO₂ 내의 Pd의 분산도 및 화학 상태를 명확하게 변화시켰다.

주요어: 저온 메탄 연소 반응, 코발트 촉매, 산 처리, 팔라듐 담지 촉매, 탈알루미늄화, 팔라듐 전구체

학 번: 2017-26064